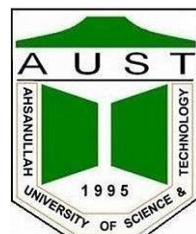


بسم الله الرحمن الرحيم

# **DESIGN & DEVELOPMENT OF A FIXED WING VTOL UAV WITH TILT-ROTORS**

By

**Student 1- Dewan Mohammed Eshak (20200208010)**  
**Student 2- Ahsanul Kabir Shuvo (20200208170)**  
**Student 3- Laisur Rahman Turjo (20200208107)**



**DEPARTMENT OF MECHANICAL AND PRODUCTION  
ENGINEERING (MPE)**

**AHSANULLAH UNIVERSITY OF SCIENCE AND TECHNOLOGY  
(AUST)  
DHAKA-1208, BANGLADESH**

# **DESIGN & DEVELOPMENT OF A FIXED WING VTOL UAV WITH TILT- ROTORS**

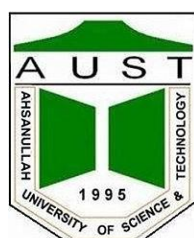
By

**Dewan Mohammed Eshak**                   **2020.02.08.010**

**Ahsanul Kabir Shuvo**                   **2020.02.08.170**

**Laisur Rahman Turjo**                   **2020.02.08.107**

A Thesis Submitted to the  
Department of Mechanical and Production Engineering,  
In partial fulfillment of the requirements for the Degree of  
**BACHELOR OF SCIENCE IN MECHANICAL ENGINEERING**



**DEPARTMENT OF MECHANICAL AND PRODUCTION  
ENGINEERING (MPE)**  
**AHSANULLAH UNIVERSITY OF SCIENCE AND TECHNOLOGY**  
**(AUST)**  
**DHAKA-1208, BANGLADESH**

**June 2025**

# CERTIFICATE OF SUBMISSION

---

The thesis entitled "**DESIGN & DEVELOPMENT OF A FIXED WING VTOL UAV WITH TILT-ROTOR**S" submitted by the following students has been accepted for partial fulfillment of the requirement for the degree of B.Sc. in Mechanical Engineering in June 2025.

**Dewan Mohammed Eshak**      **2020.02.08.010**      Signature: \_\_\_\_\_

**Ahsanul Kabir Shuvo**      **2020.02.08.170**      Signature: \_\_\_\_\_

**Laisur Rahman Turjo**      **2020.02.08.107**      Signature: \_\_\_\_\_

Thesis Supervisor:

---

**Dr. Mohammad Harun-Or-Rashid**  
Associate Professor  
Dept. of MPE  
Ahsanullah University of Science and Technology

External Examiner:

---

**Dr. Fazlur Rahman**  
Associate Professor  
Dept. of MPE  
Ahsanullah University of Science and Technology

# DECLARATION OF CANDIDATE

---

It is hereby declared that this thesis or any part of it has not been submitted elsewhere for the award of any degree or diploma.

**Dewan Mohammed Eshak**      **2020.02.08.010**      Signature: \_\_\_\_\_

**Ahsanul Kabir Shuvo**      **2020.02.08.170**      Signature: \_\_\_\_\_

**Laisur Rahman Turjo**      **2020.02.08.107**      Signature: \_\_\_\_\_

**This work is dedicated to  
Our loving parents**

## ACKNOWLEDGEMENT

---

In the Name of Allah, the Most Gracious, the Most Merciful (Al-Rahman, Al-Rahim) (Tawfiq)

This thesis is a humble tribute to the ultimate planner, Allah (SWT). Our deepest gratitude goes to our esteemed supervisor, Associate Professor Dr. Mohammad Harun-Or-Rashid, from the Department of Mechanical & Production Engineering at Ahsanullah University of Science and Technology. His guidance throughout this journey has been a true blessing. Professor Rashid's wisdom and expertise became a beacon, illuminating the path whenever we faced challenges. We are incredibly fortunate to have had the opportunity to learn from him.

We would also like to express our sincere thanks to Omon Sharker Thinan for his invaluable advice on system design using Computer-Aided Design (CAD) software. His insights were instrumental in shaping the technical aspects of this project.

## ABSTRACT

---

This report details the design, simulation, and control system development of a novel tiltrotor fixed-wing UAV for diverse applications. This fixed-wing UAV consists of an innovative glider design with a tiltrotor for easier vertical take-off and landing (VTOL) using thrust vectoring capability. The fixed-wing design of the UAV optimizes its flight efficiency by generating higher aerodynamic lift, making it highly versatile for a wide range of applications, including agricultural, medical, cargo transport, and surveillance. The novel innovation is in the tiltrotor mechanism and glider configuration, both of which enable VTOL and efficient fixed-wing flight. Both 2D sketching and 3D CAD model designs were derived from the computed optimum shape using SOLIDWORKS following the Informed Design Process. Iterative optimization was further conducted based on simulated computational fluid dynamics (CFD) outcomes using ANSYS and XFLR5 software. The aerodynamic performance of the wing and propeller was analyzed through simulations for flight characteristics by utilizing the principles of physics of the UAV. The UAVs' wing geometry and profile were optimized for greater lift with less drag. The design with a wingspan of 1.2 meters and a chord length of 0.2 meters, with a gross weight of 2000 grams and a load capacity of 500 grams, meets the requirements for the design. The cruising speed and max operating speed are set to 10m/s and 30m/s, which produce a lift force of around 12 N and 103 N, respectively. The prototype UAV is a hybrid created from a combination of Polylactic acid 3D-printed components and a structural tube from carbon fiber to provide strength, light weight, and affordability. A single Teensy-based flight controller with a stable flight program was used to gain steady and stable flight dynamics. Although the current prototype is configured for manual control, the system can accommodate autonomous flight in the future. This work contributes to the development of low-noise, efficient UAV technology suitable for various applications across industry.

# TABLE OF CONTENTS

|                                                          |       |
|----------------------------------------------------------|-------|
| CERTIFICATE OF SUBMISSION.....                           | 3     |
| DECLARATION OF CANDIDATE.....                            | 4     |
| DEDICATION .....                                         | 5     |
| ACKNOWLEDGEMENT .....                                    | 6     |
| ABSTRACT.....                                            | 7     |
| TABLE OF CONTENTS.....                                   | 8-10  |
| LIST OF TABLES .....                                     | 11    |
| LIST OF FIGURES .....                                    | 12-15 |
| LIST OF ABBREVIATIONS.....                               | 16    |
| NOMENCLATURE .....                                       | 17    |
| Chapter 1.....                                           | 18    |
| INTRODUCTION .....                                       | 18    |
| 1.1 Background.....                                      | 18    |
| 1.1.1 Types of UAVs .....                                | 19    |
| 1.2 Problem Statements .....                             | 19    |
| 1.3 Objectives .....                                     | 20    |
| 1.4 Scopes of the Thesis.....                            | 20    |
| Chapter 2.....                                           | 21    |
| LITERATURE REVIEW .....                                  | 21    |
| 2.1 Research Gaps and Future Works.....                  | 31    |
| Chapter 3.....                                           | 32    |
| METHODOLOGY .....                                        | 32    |
| 3.1 Designing of setup .....                             | 32    |
| 3.2 Electrical Components Selection with Comparison..... | 32    |
| Chapter 4.....                                           | 36    |
| THEORY AND CALCULATION .....                             | 36    |
| 4.1 Theory .....                                         | 36    |
| 4.2 Dimensions for calculation .....                     | 37    |
| 4.3 Minimum Success Criteria.....                        | 37    |
| 4.4 System Design Approach.....                          | 38    |
| 4.5 Graphical Comparison of Estimated Data .....         | 41    |
| 4.6 Tail Calculation.....                                | 41    |
| 4.7 UAV Performance Estimation Code.....                 | 43    |
| Chapter 5.....                                           | 46    |
| DESIGN .....                                             | 46    |
| 5.1 Structure Design.....                                | 46    |
| 5.1.1 Airfoil Selection.....                             | 46    |
| 5.1.2 CFD Analysis (2D) .....                            | 49    |

|                                                                       |    |
|-----------------------------------------------------------------------|----|
| 5.1.2.a Grid Independence Test .....                                  | 49 |
| 5.1.3 UAV CAD Design .....                                            | 50 |
| 5.1.4 VTOL Rotor Mechanism .....                                      | 51 |
| 5.1.4.a Working Principle of VTOL .....                               | 52 |
| 5.1.5 CAD Tail Design .....                                           | 54 |
| 5.1.6 Final Design Dimension.....                                     | 55 |
| 5.1.7 Final Design Render .....                                       | 56 |
| 5.2 Control System Architecture and Process.....                      | 57 |
| 5.3 Circuit Design .....                                              | 62 |
| 5.4 Control System Integration and Calibration .....                  | 65 |
| Chapter 6.....                                                        | 66 |
| DEVELOPMENT .....                                                     | 69 |
| 6.1 Weight of the Aircraft.....                                       | 70 |
| 6.2 Fabrication .....                                                 | 70 |
| Chapter 7.....                                                        | 73 |
| SUSTAINABILITY.....                                                   | 73 |
| 7.1 Social Impact Assessment.....                                     | 73 |
| 7.1.1 Social Benefits of the Project.....                             | 73 |
| 7.1.2 Critical Analysis of Sustainable Development Goals (SDGs) ..... | 73 |
| 7.2 Environmental Impact Assessment.....                              | 74 |
| Chapter 8.....                                                        | 77 |
| RESULTS & DISCUSSION.....                                             | 77 |
| 8.1 Experimental Data for Validation .....                            | 77 |
| 8.2 Validation Analysis with Miley Airfoil Data.....                  | 78 |
| 8.3 Results.....                                                      | 79 |
| 8.4 Validation Against Open-Source Airfoil Data.....                  | 80 |
| 8.5 CFD Analysis (3D) .....                                           | 82 |
| 8.5.1 Lift.....                                                       | 82 |
| 8.5.2 Drag.....                                                       | 83 |
| 8.5.3 Downwash.....                                                   | 85 |
| 8.5.4 Streamline .....                                                | 85 |
| 8.5.5 Propeller Thrust Force .....                                    | 89 |
| 8.6 Optimization .....                                                | 90 |
| 8.6.1 Redesign of Wing.....                                           | 90 |
| 8.6.2 Verification of the Optimized Wing .....                        | 91 |
| Chapter 9.....                                                        | 93 |
| CONCLUSIONS.....                                                      | 93 |
| 9.1 Conclusion .....                                                  | 93 |
| 9.2 Future Recommendation.....                                        | 94 |

|                  |         |
|------------------|---------|
| REFERENCES ..... | 96-98   |
| APPENDIX.....    | 969=106 |

## **LIST OF TABLES**

---

| <b>Table No.</b> | <b>Table Title</b>                                                                             | <b>Page No.</b> |
|------------------|------------------------------------------------------------------------------------------------|-----------------|
| Table 3.1        | Comparison of motors according to their thrust, power & <i>efficiency</i>                      | 34              |
| Table 3.2        | Comparison of different types of propellers                                                    | 34              |
| Table 3.3        | Comparison of different types of electric speed controllers (ESC)                              | 35              |
| Table 3.4        | Comparison of Servo motors according to Torque, Speed                                          | 35              |
| Table 3.5        | Specifications & Weight estimation of equipment used in project                                | 36              |
| Table 4.1        | Design Parameters of the UAV                                                                   | 40-41           |
| Table 4.2        | Numerical Value of Different Parameters According to Different<br>Wing Loading ratio W/S Ratio | 41-42           |
| Table 4.3        | Horizontal & Vertical tail parameters                                                          | 44-44           |
| Table 5.1        | Comparative Illustration of Different Types of Airfoils                                        | 47-48           |
| Table 5.1(a)     | Selection of Airfoil                                                                           | 48              |
| Table 6.1        | Weight of the aircraft                                                                         | 71              |
| Table 8.1        | Values of Lift and Drag Coefficient for different angles of attack                             | 79              |
| Table 8.2        | Numerical Calculated Value of Lift(L) & Drag(D) at Different Velocities                        | 81              |
| Table 8.3        | Comparison of Computational & Experimental Data at Different AoA for<br>10m/s velocity         | 83-84           |
| Table 8.4        | Extracted Values from Simulation                                                               | 89              |
| Table 8.5        | Parameter Setting for the CFD Analysis                                                         | 89              |

## LIST OF FIGURES

---

| <b>Figure No—figure Title</b>                                                                                  | <b>Page No</b> |
|----------------------------------------------------------------------------------------------------------------|----------------|
| Fig. 2.1 Drone delivery setup of Amazon.                                                                       | 21             |
| Fig. 2.2 The glider patent for payload disposal with folding wing                                              | 22             |
| Fig. 2.3 The hybrid design of glider and quadcopter                                                            | 22             |
| Fig. 2.4 Pressure Contour for various angles of attack for lift and drag                                       | 28             |
| Fig. 2.5 Velocity Streamline for stall phenomenon                                                              | 29             |
| Fig. 2.6 3D model of the VTOL plane with a) twin-tail boom, b) transverse arm,<br>c) tandem wing configuration | 30             |
| Fig. 3.1 Flow chart of overall methodology                                                                     | 32             |
| Fig. 3.2 Flow chart of design methodology                                                                      | 33             |
| Fig. 5.1 Block Diagram of Structural Design Process                                                            | 47             |
| Fig. 5.1(b) Comparison of 3airfoils with respect to $C_l$ vs $\alpha$ , $C_l$ vs $C_d$                         | 49             |
| Fig. 5.1(c) Wing and extremity profile                                                                         | 49             |
| Fig. 5.2 Grid Dependency Test                                                                                  | 50             |
| Fig. 5.3 NACA-4412 airfoil Pressure Contour                                                                    | 51             |
| Fig. 5.4 NACA-4412 airfoil Velocity Contour                                                                    | 51             |
| Fig. 5.5 CAD Model of NACA 4412 Airfoil Based Wing                                                             | 52             |
| Fig. 5.6 CAD Design of the UAV                                                                                 | 52             |
| Fig. 5.7 VTOL Rotor Mechanism with Components                                                                  | 53             |
| Fig. 5.8 CAD Design of the VTOL Rotor Mechanism                                                                | 54             |
| Fig. 5.9 The tail design procedure                                                                             | 55             |
| Fig. 5.10 Dimensions of UAV top view and side view                                                             | 56             |
| Fig. 5.11 Final render of full model UAV a) Top view, b) Front Isometric view                                  | 57             |
| Fig. 5.12 T-motor AS2820 880KV                                                                                 | 58             |

---

|           |                                                                                                                                                                                                                                                   |       |
|-----------|---------------------------------------------------------------------------------------------------------------------------------------------------------------------------------------------------------------------------------------------------|-------|
| Fig. 5.13 | TD-8320MG 20kg Waterproof Digital Metal Gear                                                                                                                                                                                                      | 58    |
| Fig. 5.14 | Red Volcano 11.1V 3S lipo 5200mah Battery                                                                                                                                                                                                         | 59    |
| Fig. 5.15 | Emax BLHeli 50A ESC with 5V3A BEC                                                                                                                                                                                                                 | 59    |
| Fig. 5.16 | 12×6.0 Carbon Fiber Propellers CW/CCW                                                                                                                                                                                                             | 60    |
| Fig. 5.17 | Fly sky FS-i6X 2.4GHz 6CH Transmitter                                                                                                                                                                                                             | 60    |
| Fig. 5.18 | Teensy 4.0 microcontroller unit                                                                                                                                                                                                                   | 61    |
| Fig. 5.19 | MPU-6050 IMU sensor                                                                                                                                                                                                                               | 61    |
| Fig. 5.20 | Micro SD card module                                                                                                                                                                                                                              | 62    |
| Fig. 5.21 | Mini 360 buck converter module                                                                                                                                                                                                                    | 62    |
| Fig. 5.22 | Micro SD card module setup on a breadboard                                                                                                                                                                                                        | 63    |
| Fig. 5.23 | The Circuit Diagram designed for VTOL                                                                                                                                                                                                             | 64    |
| Fig. 5.24 | The PCB design for VTOL UAV, a) 2D View, b) 3D View                                                                                                                                                                                               | 64-65 |
| Fig. 5.25 | Detailed block diagram of a UAV rotation rate control system, illustrating the error between desired and measured rotation, the PID controller's role, motor and UAV dynamics, and the sensor feedback mechanism                                  | 65    |
| Fig. 5.26 | Time-series plot visualizing the IMU data, highlighting the fluctuation in rotational rates without calibration                                                                                                                                   | 67    |
| Fig. 5.27 | Time-series plot visualizing the IMU data, highlighting the fluctuation in rotational rates with calibration                                                                                                                                      | 68    |
| Fig. 5.28 | Visualization of Transmitter Calibration. The left image shows the initial Serial Monitor output, highlighting the need for trimming. The right image shows the corrected output after trimming, ensuring precise control inputs for the VTOL UAV | 69    |
| Fig. 7.1  | A Holistic Approach to Sustainable Design                                                                                                                                                                                                         | 76    |
| Fig. 7.2  | Key Environmental Impact parameters of the wing assembly's LCA                                                                                                                                                                                    | 77    |

|            |                                                                                                     |    |
|------------|-----------------------------------------------------------------------------------------------------|----|
| Fig. 7.3   | Components contributing most to four areas of environmental impact                                  | 77 |
| Fig. 7.4   | Environmental Impact (calculated using CML impact assessment methodology)                           | 78 |
| Fig. 8.1   | Comparison between (a) Left one: Cl vs AoA; & (b) Right one: Cl vs Cd from XFLR5 and Miley's report | 80 |
| Fig. 8.2   | Lift Coefficient vs Angle of Attack at Different Velocities                                         | 81 |
| Fig. 8.3   | Lift Coefficient vs Drag Coefficient at Different Velocities                                        | 82 |
| Fig. 8.4   | Comparison Between Computational Data & Experimental Data of Lift-Co-Efficient vs Angle of Attack   | 82 |
| Fig. 8.5   | Comparison Between Computational Data & Experimental Data of Lift Coefficient vs Drag Coefficient   | 83 |
| Fig. 8.6a  | Lift Profile at $10^0$ Angle of Attack                                                              | 84 |
| Fig. 8.6b  | Lift Profile at $-9^0$ Angle of Attack                                                              | 84 |
| Fig. 8.7a  | Induced Drag (top view)                                                                             | 85 |
| Fig. 8.7b  | Induced Drag Profile (isometric view)                                                               | 85 |
| Fig. 8.8a  | Downwash Profile at $10^0$ Angle of Attack                                                          | 85 |
| Fig. 8.8b  | Downwash Profile at $-9^0$ Angle of Attack                                                          | 86 |
| Fig. 8.9a  | Streamline Profile (top view)                                                                       | 86 |
| Fig. 8.9b  | Streamline Profile at $10^0$ Angle of Attack                                                        | 87 |
| Fig. 8.9c  | Streamline Profile at $-9^0$ Angle of Attack                                                        | 87 |
| Fig. 8.10a | Combine Isometric View of Lift, Drag, Downwash, Streamline At $10^0$ AOA                            | 88 |
| Fig. 8.10b | Combine Isometric View of Lift, Drag, Downwash, Streamline At $-9^0$ AOA                            | 88 |
| Fig. 8.11a | Propeller Velocity Contour with Thrust Force                                                        | 89 |

|                                                                                                      |    |
|------------------------------------------------------------------------------------------------------|----|
| Fig. 8.11b Propeller Velocity Streamline                                                             | 90 |
| Fig. 8.12 Optimized Wing Lift & Drag                                                                 | 91 |
| Fig. 8.13 Combine Isometric View of Optimized wing Lift, Drag,<br>Downwash, Streamline At $10^0$ AOA | 92 |

## LIST OF ABBREVIATIONS

---

|       |                                             |
|-------|---------------------------------------------|
| UAV   | Unmanned Aerial Vehicle                     |
| VTOL  | Vertical Take-Off and Landing               |
| CG    | Center of Gravity                           |
| CAD   | Computer-Aided Design                       |
| CFD   | Computational Fluid Dynamics                |
| AoA   | Angle of Attack                             |
| BLDC  | Brushless DC Motor                          |
| GPS   | Ground Positioning System                   |
| Li-Po | Lithium Polymer Battery                     |
| ESC   | Electronic Speed Controller                 |
| AR    | Aspect Ratio                                |
| MAC   | Mean Aerodynamic Chord                      |
| MTOW  | Maximum Take-Off Weight                     |
| EW    | Empty Weight                                |
| AUW   | All Up Weight                               |
| NACA  | National Advisory Committee for Aeronautics |

## NOMENCLATURE

---

| <b>Symbol</b> | <b>Description</b>                        |
|---------------|-------------------------------------------|
| $\gamma$      | Glide Angle                               |
| $\lambda$     | Taper Ratio                               |
| $\rho$        | Density                                   |
| L             | Lift                                      |
| D             | Drag                                      |
| W             | Weight                                    |
| $C_L$         | Coefficient of Lift                       |
| $C_d$         | Coefficient of Drag                       |
| $C_{root}$    | Root Chord                                |
| $C_{Tip}$     | Tip Chord                                 |
| S             | Wing Area                                 |
| b             | Wingspan                                  |
| V             | Velocity                                  |
| e             | Oswald Efficiency                         |
| $\mu$         | Dynamic viscosity of the fluid            |
| Re            | Reynolds Number                           |
| $V_{HT}$      | Volume coefficient of the horizontal tail |
| $V_{VT}$      | Volume coefficient of the vertical tail   |
| $L_{bt}$      | Lever arm length                          |
| $S_{VT}$      | Area of the vertical stabilizer           |

---

# Chapter 1

## INTRODUCTION

---

Unmanned Aerial Vehicles (UAVs) have emerged as transformative tools, reshaping industries such as agriculture, disaster management, surveillance, and beyond. Once experimental, drones were now handy helpers in many sectors. People are getting excited about hybrid drones. These drones combine the best of fixed-wing and rotary-wing aircraft. One of the biggest stars is the Vertical Take-Off and Landing (VTOL) fixed-wing drone. This aircraft is quite a performer. It hovers and takes off vertically like a helicopter. But it also travels far and saves energy like a fixed wing. Tilt-rotor drones can quickly switch from flying straight up to flying forward. With a turning propeller system, these drones break free from the limits of regular ones. They are complex to control but more flexible.

### 1.1 Background

For generations, people have looked to the skies with a desire to fly. Over time, consistent effort and innovation have helped turn this dream into reality. The first powered flight was successfully carried out by the Wright brothers in 1903 [1]. Aviation technology has dramatically evolved, leading to the common presence of advanced flying machines like unmanned aerial vehicles (UAVs) in today's skies. Massive improvements in materials and electronics have led to and come from the evolution of today's UAV designs. The use of UAVs is not a new idea, with the development of the technology starting in the early 20th century, back to the First World War, where radio-controlled aircraft were used, but not widely adopted until as late as the Vietnam War, where they were mainly used for aerial surveillance. The technology of UAVs has developed rapidly in the 21st century because of the advances achieved in onboard computers, sensors and communication networks. Drones are very common today among various industries. In the agricultural industry, as a special case, unmanned aerial vehicles equipped with specific sensors simplify field monitoring and management for the farmers. In disaster recovery, they can capture real-time aerial photos and help search and rescue teams find the missing [2].

In the future, fixed-wing VTOL (Vertical Take-Off and Landing) UAVs are considered a promising area of development. Such hybrid aircraft can take off and land vertically, as if they were helicopters, making them relatively easy to use across cities. The concept of VTOL dates to the mid-20th century, with the development of tilt-rotor aircraft such as the Bell XV-15 and

the V-22 Osprey [3-4]. These early prototypes demonstrated the potential of VTOL technology to overcome the limitations of conventional aircraft designs, paving the way for its integration into UAV platforms. Most of the modern UAVs have tilted rotors to give a two-fold functionality. Such a design provides advantages in places where little space is available or the ground is difficult. With ongoing advancements, the long-standing goal of achieving reliable and versatile flight is coming closer to being fully realized. In the 21st century, advancements in sensor technology and miniaturization accelerated the capabilities of UAVs, opening new frontiers in aerial exploration.

### **1.1.1 Types of UAVs**

There are many types of UAVs depending on the applications, size, shape, and propulsion system [5]. Some of the few are:

- Fixed-Wing UAVs
- Rotary-Wing UAVs
- Hybrid UAVs
- Nano UAVs
- Micro UAVs
- Mini UAVs
- Tactical UAVs

Apart from the above classifications, UAVs can be classified into more segments, based on altitude, based on size, etc. Normally, UAVs are used to accomplish missions that are impossible or dangerous for human beings to perform and can lead to serious injuries. But nowadays, commercial or civil UAV usage can be seen more frequently.

## **1.2 Problem Statements**

While rising tech gives us new flying drones that take off and land like helicopters but fly like planes, they still have some tricky issues. The way these tilt-rotor drones are built means they have to face complex problems tied to how they fly, their engines, design, and control systems. A tough time for these drones is the "change phase". This is when they're switching from a helicopter-like take-off or landing to an airplane-like forward flight. The control and stability during this period are tough to handle. Some other big problems include:

- Keeping a steady flight at all times.
- Working out the weight balance and control system in two flight modes.

- Keeping a strong structure under various loads depending on conditions.
- Fitting in the most cargo possible without losing performance.

To solve these problems, a deep understanding of many fields, including mechanical design, control theory, flight dynamics, and systems, is required.

### **1.3 Objectives**

After investigating existing UAV designs and technologies, gaps were identified and opportunities for innovation in VTOL tilt-rotor configurations.

The Main Objective of this project is to conceptualize and design a novel VTOL tilt-rotor UAV prototype that integrates dual rotors with thrust vectoring capabilities to achieve seamless transitions between vertical and horizontal flight modes. By conducting a comprehensive mechanical design analysis to optimize the structural integrity, aerodynamic performance, and overall efficiency of the VTOL tilt-rotor UAV. Also develop mathematical models and simulations to characterize the kinematic and dynamic behavior of the VTOL tilt-rotor UAV during various flight profiles, including hover, transition, and fixed-wing flight modes. The key objectives include,

- To identify and analyze existing VTOL tilt-rotor UAV designs and technologies.
- To develop a novel VTOL tilt-rotor UAV concept integrating dual rotors with thrust vectoring capabilities for seamless mode transitions.
- To conduct comprehensive mechanical design and analysis to optimize the UAV's structural integrity, aerodynamic performance, and overall efficiency.
- To conduct computational fluid dynamics (CFD) simulations to analyze and optimize the aerodynamic performance of the VTOL tilt-rotor UAV.
- To fabricate, test specific performance such as payload capacity, range, and flight speed of a full-scale VTOL tiltrotor UAV, and analyze the results.

### **1.4 Scopes of the Thesis**

This thesis aims to investigate the design and implementation of robust control algorithms for Vertical Takeoff and Landing (VTOL) Unmanned Aerial Vehicles (UAVs) with tilt-rotor technology to ensure stable and precise flight control across different operational scenarios, including takeoff, landing, and mid-flight maneuvers, to evaluate the practical feasibility and potential applications of the VTOL tilt-rotor UAV in real-world scenarios, such as aerial surveillance, disaster response, and agricultural monitoring.

## Chapter 2

# LITERATURE REVIEW

---

Imagine a future where packages arrive at the doorstep as effortlessly as receiving an email. Amazon, one of the world's tech giants, is at the forefront of redefining the logistics industry. Na, W. et al. [6] examined a specific instance using Amazon's drone delivery system. Their ambitious Prime Air project envisions a world where UAVs safely navigate our skies, delivering packages with speed and efficiency. To make this vision a reality, Amazon is investing heavily in the development of advanced drone technology. These autonomous aircraft will not only be capable of independent flight but also possess the intelligence to communicate and coordinate with one another, forming a complex aerial network. This sophisticated system will optimize delivery routes, avoid obstacles automatically, and ensure the safe integration of drones into our existing airspace.



Figure 2.1: Drone delivery setup of Amazon. (Courtesy of AV web) [7].

By streamlining the delivery process, Amazon's drone delivery initiative holds the promise of transforming the global supply chain. The drone delivery market, valued at \$234.4 million in 2021, is expected to reach \$3,119.3 million by 2028, with Amazon potentially leading due to rapid deliveries and a 53.94% growth rate. As this groundbreaking technology continues to evolve, it has the potential to reshape entire industries and redefine our expectations for convenience and speed.

Zilberstein et al. [8] investigated an unmanned glider system designed for the purpose of payload dispersal. The Quantum Tron is a pioneering hybrid aircraft that promises to revolutionize logistics and humanitarian aid. Combining the agility of a quad with the efficiency of a glider, the innovative design offers versatile solutions to complex delivery problems. Key patents include US2007/018033, which details a deployable wing system for aerial delivery, and US2012138727, describing a sonar buoy with folding wings.

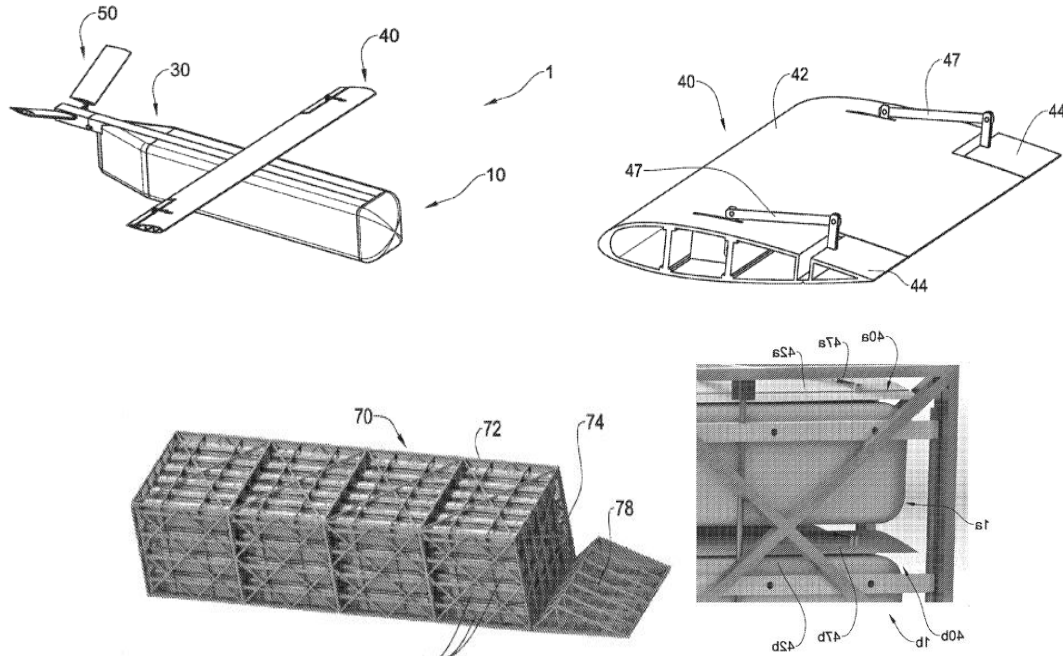


Figure 2.2: The glider patent for payload disposal with folding wing.

The gliders utilize a pressurized container for structural integrity and payload dispersion, achieving a payload-to-container weight ratio of up to 1:100. The Quantum Tron can seamlessly transition between vertical takeoff and landing along with horizontal flight, overcoming obstacles that have traditionally hindered aerial transportation. While the full potential remains to be realized, the Quantum Tron represents a significant step up in the development of hybrid unmanned aerial system.

Delivering critical medical supplies to remote regions often means overcoming significant logistical challenges. The challenges of delivering critical aid to these areas have inspired researchers at Kennesaw State University to develop a ground-breaking solution: a hybrid glider-quadcopter unmanned aerial system. Delarosa et al. [9] created a versatile glider-quadcopter. By combining the endurance of a glider with the maneuverability of a quadcopter, this innovative design aims to revolutionize humanitarian logistics.



Figure 2.3: The hybrid design of glider and quadcopter.

The researchers focused on creating a dual-stage UAS capable of carrying medical supplies

over long distances and precisely delivering them to their intended recipients by detaching the glider with the payload. While their prototype demonstrated promising results, it also revealed challenges related to manufacturing and aerodynamics performance at higher speeds. By separating the structural and aerodynamic components of the frame which reduces the vibrational effect at higher velocities, future iterations of this design could potentially enhance its overall performance and durability. This research is a valuable foundation for further exploration of hybrid UAS systems and their applications in humanitarian aid.

Wang et al. [10] performed a study on the design, development, modeling, and flight testing of a VTOL UAV. VTOL vehicles are an invention in the field of aviation technology since it can ascend and descend vertically and can be operated within small areas. VTOL, an abbreviation for Vertical Takeoff and Landing, was developed initially during the mid-20th century. One of the key breakthroughs was the development by Bertin Technologies of the Hover Eye platform, demonstrating what could be achieved with robotic VTOL (Vertical Takeoff and Landing) systems. Today, several Vertical Takeoff and Landing aircraft configurations exist, including flying, helicopter-type, and ducted designs. All have different advantages and applications.

Czyba, R et al. [11] conducted a study on the effect of control structure on flight performance of a multi-rotor VTOL platform. The most dominant objective of research in this domain is to achieve an increase in velocity, stability, and controllability of VTOL vehicles. This is only made possible in order to extend the possible applications and versatility of such vehicles to domains like the military, business, and pleasure.

Ducard et al. [12] carried out research design and flight control method of hybrid and convertible VTOL UAVs. Unmanned aerial vehicles are increasingly being used in many sectors, such as agriculture, film production, monitoring, and intelligence gathering. The development of control systems that guarantee stability, ability to perform self-rotation, and flight of unmanned aerial vehicles is of great importance.

In the study by Choi et al. [13], machine learning techniques have been presented for unmanned aerial vehicles (UAVs). Many control methodologies—such as adaptive control algorithms, proportional integral derivative (PID) controllers, and model predictive control (MPC) have been explored in this specific research area.

Roghair et al. [14] did a study on a deep reinforcement learning system that uses vision to help unmanned aerial vehicles (UAVs) avoid obstacles. This research enhances UAV obstacle avoidance by extending the Dueling Double Deep Q Network (D3QN) algorithm from 2D to 3D environments. Using a stereo camera, it improves depth estimation by integrating object detection, allowing for better handling of both static and dynamic obstacles. A key contribution

is the introduction of a domain network and Gaussian mixture model to optimize exploration in complex environments, leading to more efficient learning and faster convergence compared to conventional D3QN approaches. Simulated 3D environments were configured for deep reinforcement learning tasks. The improved exploration algorithms, particularly guidance exploration, significantly outperformed existing methods like D3QN and convergence exploration, achieving up to 200% improvement in average rewards in complex environments. The enhanced performance is attributed to faster learning of optimal policies and more efficient exploration of unseen states. However, future work is necessary to refine the dynamic network structure, stabilize performance in more complex environments, and further integrate real-time object detection and tracking for real-world UAV applications.

Leong et al. [15] constructed a hover control system for a quadcopter using a low-cost microcontroller. Hover stability is essential for quadcopter applications such as surveillance, crop monitoring, and imaging, helping to prevent crashes due to wind or weight imbalances. This paper introduces a cost-effective Hover Control System using the Arduino Duemilanove microcontroller, an affordable alternative to high-end controllers like DJI Naza. The system integrates three main subsystems: the quadcopter, an ultrasound sensor, and the microcontroller. The PID control algorithm is used to maintain a stable hover altitude by adjusting throttle inputs based on the difference between the actual and desired altitude. This setup simplifies the control from six to three degrees of freedom, allowing easier maneuverability. The microcontroller communicates with the quadcopter's gyroscope and electronic speed controller (ESC) to maintain a constant hover while responding to altitude variations. The system's low cost, portability, and compatibility with existing quadcopter components make it a customizable solution, with potential for broader applications across different UAV systems. The software simulation tested P, PI, and PID controls on a quadcopter's hover stability. PID was selected for its zero steady-state error and lower overshoot. However, hardware implementation using simulation parameters proved unstable. An empirical tuning method yielded optimal PID values of 0.005, 0.01, and 0.003, achieving stable hover control with a  $\pm 2$  cm error during a 5-minute flight.

Zhimin Sun et al. [16] conducted an in-depth analysis of control techniques for brushless DC motors, specifically in the context of unmanned aerial vehicles (UAVs). This research focuses on optimizing motor performance through advanced control strategies, such as field-oriented control (FOC) and pulse-width modulation (PWM). FOC enhances efficiency by adjusting the electrical currents to align with the rotor's magnetic field, significantly improving torque generation and responsiveness. PWM, on the other hand, allows for precise control of voltage

levels, resulting in smoother and more effective motor operation. The combined implementation of these control strategies aims to achieve accurate thrust control, which is crucial for enhancing flight stability and maneuverability in UAVs. These advancements not only bolster the efficiency of the propulsion systems but also contribute to the overall reliability of modern UAV operations, allowing for more complex tasks and improved operational capabilities. The insights from this study are vital for the ongoing development of UAV technology, supporting innovations in various applications such as surveillance, agricultural monitoring, and logistics.

Millán-Arias et al. [17] performed research on the use of reinforcement learning to operate unmanned aerial vehicles (UAVs) using policy and reward shaping techniques. The paper explores the integration of machine learning, specifically Reinforcement Learning (RL), into the control of Unmanned Aerial Vehicles (UAVs). Initially, it outlines the progression of UAVs from their early development by Archibald Low in 1916 to their modern applications in various sectors like agriculture, military, and recreation. A significant challenge identified is the difficulty in creating accurate models for UAVs to operate autonomously in real-world environments, due to limited or unreliable prior information. The study focuses on using RL, where an agent learns by interacting with its environment, making decisions based on rewards for its actions. A key issue with traditional RL is the time taken for an agent to learn due to complex state-action spaces. The paper introduces Interactive Reinforcement Learning (IRL) as a potential solution, where a human trainer helps speed up learning by providing real-time feedback. Two methods, reward-shaping and policy-shaping, are analyzed. Reward-shaping allows the trainer to adjust rewards, while policy-shaping guides the agent in action selection. The results show that these methods can enhance the learning process and improve UAV control, ensuring more precise and stable operations.

The text is referred to as [18] H. K. Khalil, "Nonlinear Systems," 2002. The book gives the reader a framework for the analysis and control of the nonlinear dynamics of unmanned aerial vehicles. Advanced methods of approaching the intrinsic nonlinearities of the UAV systems are presented: stability analysis, feedback linearization, and Lyapunov-based control. They serve as a fundamental basis in the execution of complicated maneuvers with stability under changing conditions and disturbances. Khalil's concepts can be used to expand the capabilities of UAVs in executing complex maneuvers and gathering stability in difficult environments, thereby resulting in the design of control systems that are both reliable and efficient.

Xie et al. [19] did research on the implementation of recursive sliding mode attitude control for tiltrotor UAV. The work from Cornell University introduces an adaptive recursive sliding mode

attitude control system designed specifically for tiltrotor UAVs to provide smooth flight mode transitions. The paper introduces a Super-Twisting Extended State Observer (STESO) combined with Adaptive Recursive Sliding Mode Control (ARSMC) to manage the transition between hover and forward modes. This approach improves robustness, handles model uncertainties, and ensures fast convergence by estimating disturbances and using Lyapunov-based stability analysis. The proposed control method shows significant performance improvements, reducing transition time and ensuring superior attitude tracking compared to conventional methods like Sliding Mode Control (SMC) or Model Predictive Control (MPC). The paper also highlights the novelty of applying the SAC method in both the conversion and reconversion phases, which had been studied separately in prior research. This integrated approach, verified through comparative simulations, positions the SAC strategy as a viable solution for attitude control during transition, making it suitable for tiltrotor UAVs and other complex nonlinear systems. In this paper, six degrees of freedom dynamic and kinematic equations for a tiltrotor UAV are derived. Based on the nonlinear model, a SAC method is proposed and tested through simulations. Results demonstrate that SAC offers higher control accuracy, faster response, and better robustness than FTSMC and RSMC methods in controlling the roll, pitch, and yaw angles during transition phases.

D'Amato et al. [20] did research on the use of nonlinear dynamic inversion and neural networks to a tilt tri-rotor unmanned aerial vehicle (UAV). In this paper, tiltrotor UAVs, capable of both hovering and high-speed forward flight, are analyzed for their complex dynamics and control challenges during transition phases. The nonlinear dynamics of such UAVs demand distinct control strategies for hover and forward modes. A promising approach for UAV control is Nonlinear Dynamic Inversion (NDI), which attempts to linearize systems and decouple control variables, although it's sensitive to model errors and disturbances. To address these issues, Incremental NDI (INDI) and adaptive control methods are employed. The paper further integrates a Radial Basis Function Neural Network (RBF-NN) with NDI to enhance control robustness against modeling uncertainties. Simulation results on a small-scale tri-rotor UAV demonstrate the effectiveness of these methods, including their potential for transition phases from hover to forward flight. The numerical simulations in this paper demonstrate the performance of the proposed controller for tiltrotor UAVs under various input signals. Maneuvers along the x, y, and z axes, and yaw rotation, were simulated, with a focus on Neural Network (NN) adaptation to unmodeled dynamics such as aerodynamic drag. Simulations were performed both with and without external disturbances like gusts and turbulence. Results show that the NN compensator significantly improves control performance, especially in lateral

movement under gust conditions. The controller also maintains robust stability during the critical transition phase between hovering and forward flight.

Zhao et al. [21] did a study on the method for transitioning between different flying modes in tilt-rotor VTOL UAVs. Unmanned Aerial Vehicles (UAVs) are crucial in smart city development, particularly in urban settings. They can be categorized into two main types: fixed-wing UAVs, known for high speed and efficiency, and helicopters, which excel in vertical takeoff and landing but suffer from low speed and aerodynamic inefficiency. The tilt-rotor VTOL UAV combines the strengths of both, allowing vertical takeoff, hovering, and high-speed flight. However, its transition phase from hover to cruise involves complex dynamics like actuator redundancy and cross-coupling. To address these challenges, researchers have developed various strategies to optimize the transition process, focusing on stability and performance. This study proposes a novel strategy that enhances transition efficiency, achieving faster and more stable transitions while optimizing control input and attitude. The paper provides a comprehensive account of the creation of a versatile flight transition plan for tilt-rotor VTOL UAVs. The suggested technique enables seamless shifts between vertical and horizontal flying modes, effectively tackling the aerodynamic and control difficulties associated with such operations. The technique guarantees consistent and efficient mode changeover by enhancing control algorithms and using real-time data. The research showcases notable improvements in the flying performance and dependability, underscoring the efficacy of the multimode method in augmenting the adaptability and operating capacity of tilt-rotor VTOL UAVs.

Betancourt-Vera et al. [22] did research on stability and tracking control algorithms for VTOL aircraft. The article shows Planar Vertical Takeoff and Landing (PVTOL) aircraft which is a simplified model used to study vertical takeoff and landing systems like helicopters or quadcopters. This model focuses on the longitudinal dynamics of such vehicles, considering two motors that produce force and torque to control movement. The system is underactuated, meaning there are fewer controls than degrees of freedom, which adds complexity to stabilization. The PVTOL dynamics assume a rigid, symmetrical structure where the center of mass coincides with the origin. The vehicle's motion is affected by external forces and torques, primarily due to thrust and gravity. In simplified models, the pitch moment (rotation about the horizontal axis) creates a perpendicular force to the vertical axis, controlling vertical motion and altitude, while the lateral motion is controlled indirectly by adjusting the pitch angle. For control, feedback linearization is commonly used to regulate vertical motion, ensuring the vehicle hovers at a desired altitude. Backstepping and saturation functions are two key methods

applied to stabilize this underactuated system, allowing for controlled takeoff, hovering, and landing. These control methods are critical for managing the nonlinear dynamics of PVTOL systems, enabling precise maneuvering and altitude regulation. This paper evaluates popular control algorithms for vertical takeoff and landing (VTOL) vehicles, analyzing both classical and virtual control approaches. Four algorithms were studied, including linear and nonlinear backstepping, nested saturation functions for underactuated dynamics, and hyperbolic saturation for a virtual fully actuated system. Lyapunov theory was used for stability analysis. Results show that the virtual approach achieves smoother convergence and requires less control effort, making it promising for certain missions, though controller choice depends on specific requirements.

Nugroho et al. [23] did research on the advancement of VTOL aircraft, focusing on computational fluid dynamics. The primary objective of the research was to design and optimize a VTOL plane mainly for surveillance and monitoring applications. The objective was to improve stability, overall efficiency, and flight dynamics through various configurations. They used ANSYS Fluent for mesh generation and turbulence modeling using the SST k-Omega model for accuracy in wall calculations.

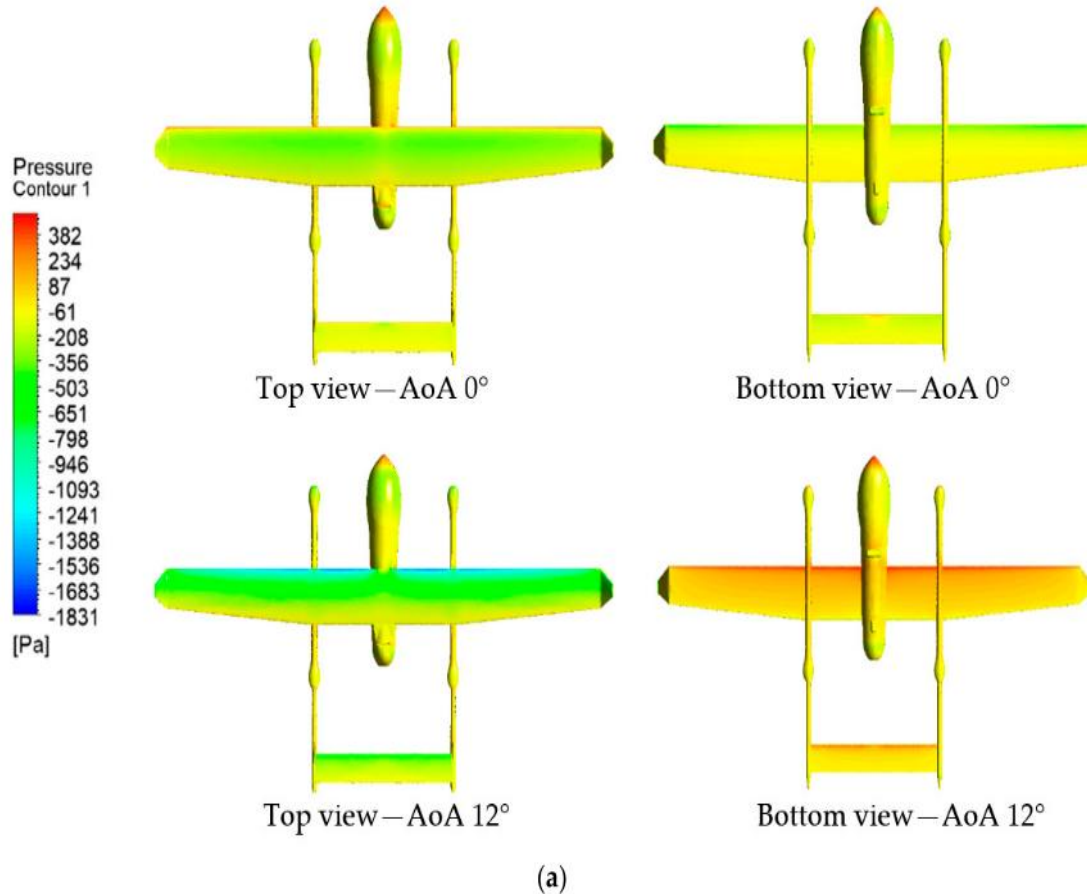


Figure 2.4: Pressure Contour for various angles of attack for lift and drag.

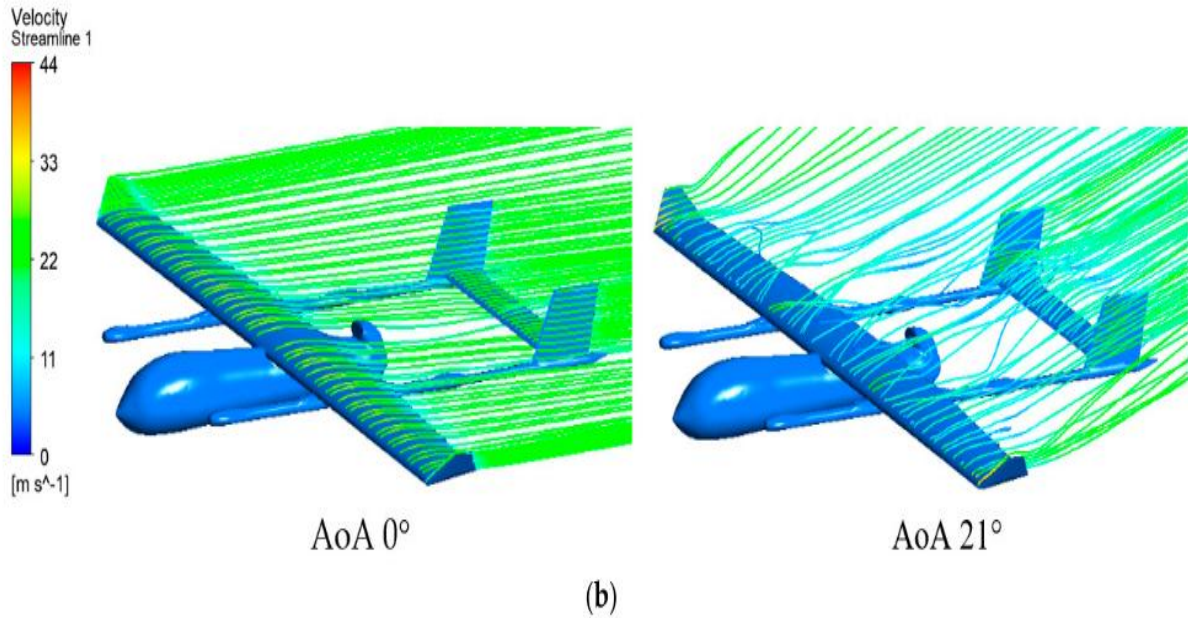


Figure 2.5: Velocity Streamline for stall phenomenon.

The findings highlighted the significance of mesh quality and size simulation results. The study successfully identified the best configuration for improved aerodynamic performance and stability. Additionally, the design requirements were met, ensuring compliance with Civil Aviation Safety Regulations (CASR). The finding of the research indicates that the inverted U-shaped boom configuration provided excellent longitudinal stability but required lateral stability optimization. The addition of a ventral fin improved lateral stability but requires further flight tests to validate the design under real conditions.

Wang et al. [24] researched tiltrotor unmanned aerial vehicles (TRUAV) to explore the existing research on the dynamics and control of TRUAV. The paper involved analyzing various aerodynamic modeling, numerical simulations, and control strategies. The literature highlighted the complexity of TRUAV control and reviewed a comparative framework for future experimental tests. This framework serves as the basis for subsequent studies aimed at refining drone-based turbulence measurement and improving its reliability.

Yoshua et al [25] researched on the aerodynamic performance of VTOL arm configurations using computational fluid dynamics. The VTOL configurations analyzed were a quad-plane, a twin-tail boom, a tandem wing, and a transverse arm. A CFD approach is employed to simulate real flight conditions, allowing for the assessment of lift, drag characteristics, stall conditions, efficiency, and maneuverability. The results conclude that each VTOL arm configuration offers distinct advantages and disadvantages. The results showed that the twin-tail boom offers the most advantages with fewer limitations.

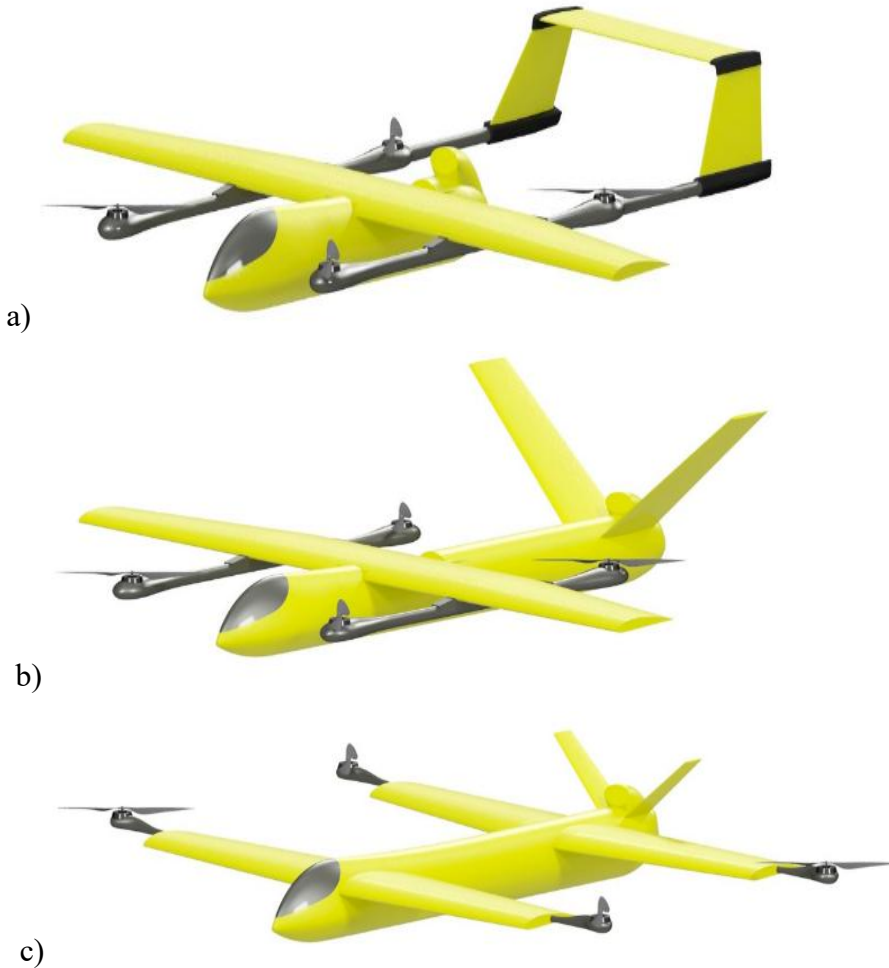


Figure 2.6: 3D model of the VTOL plane with, a) twin-tail boom, b) transverse arm, c) tandem wing configuration.

Kyoung-moo min et al. [26] conducted CFD analysis of low-altitude VTOL UAVs using ANSYS Workbench V14.5 and hybrid meshing. The study examined aerodynamic characteristics, revealing the impact of design choices on lift, drag, and vortex formation at specific angles of attack—key factors for stability. Findings emphasize the importance of precise airfoil selection, weight estimation, and mission profiling to optimize performance in both vertical and horizontal flight modes, advancing understanding of VTOL UAV design.

Kaparos et al. [27] researched on aerodynamic and stability characteristics of a VTOL fixed wing UAV MPU RX-4. The analysis of MPU RX-4 showed that the disruption in lift coefficient at 12-degree angle of attack, with subsequent stall occurring at 18-degree angle of attack. The Spalart-Allmaras turbulence model was employed for predicting the turbulent flows around the airfoils and wing under various conditions.

## 2.1 Research Gaps and Future Works

The innovative “Multipurpose Glider-Quadcopter UAS” project faced some backlash due to a small-scale prototype and a lack of extensive testing and developing a robust control algorithm. The 3D printed frame had poor fittings, which resulted in vibration and thus instability. As a result, it lacks basic real-world performance evaluation. Thus, future work requires a full-scale model to test and advance, or careful manufacturing. Also, research in VTOL aircraft systems is crucial for reaching the aerial vehicle. But a significant gap exists between real-time implementation and comparative evaluation, such as stability, robustness, and energy efficiency. PID tuning methods in different environments are required. Empowering machine learning capabilities will unlock new potential and increase the efficiency of the system. Though commercial providers like DJI have demonstrated sophisticated VTOL and quadcopter movement algorithms, those systems are proprietary and have no visible description of the methods and parameters employed in them [28]. This limits them for use by academia and development purposes. So, this can be a great research opportunity. To address this research gap and advance VTOL aircraft control systems, targeted studies and experiment-based validation are crucial.

Thus, the motivation of this research is driven by a desire to improve the existing VTOL UAV technology and contribute to developing some key addressable challenges for more efficient and sustainable aerial vehicles.

## Chapter 3

# METHODOLOGY

### 3.1 Designing of setup

A comprehensive review of the existing projects and research was conducted to identify key design principles and areas for potential improvement. Preliminary calculations, based on necessary assumptions, determined the initial design parameters, including wingspan and fuselage length. These parameters formed the basis for calculating fundamental aerodynamic forces like lift and drag. An initial drone design incorporating basic stability elements and symmetric wing profiles was developed using these parameters. Subsequent research refined this initial design by optimizing airfoil selection, considering weight, payload, and budgetary constraints. Two-dimensional simulations supported these design iterations. The Procedural flowchart depicting the methodology employed in this thesis is given in Fig. 3.1. The Fig. 3.2 shows the overall design process. Each phase of the flowchart is elaborated upon in subsequent sections of this report.

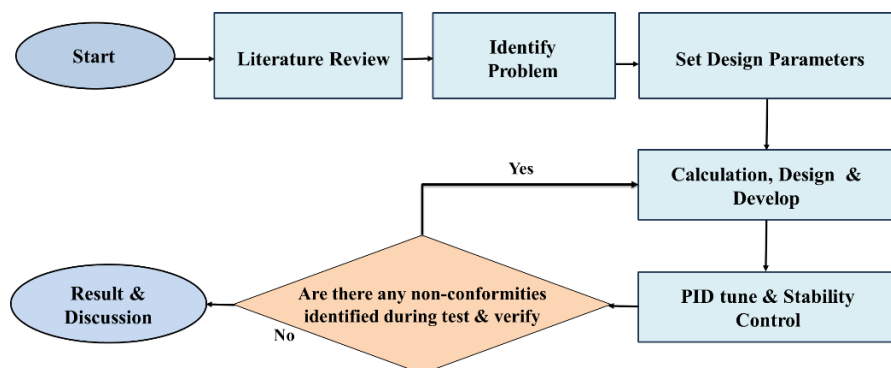


*Figure 3.1: Flow chart of the overall methodology*

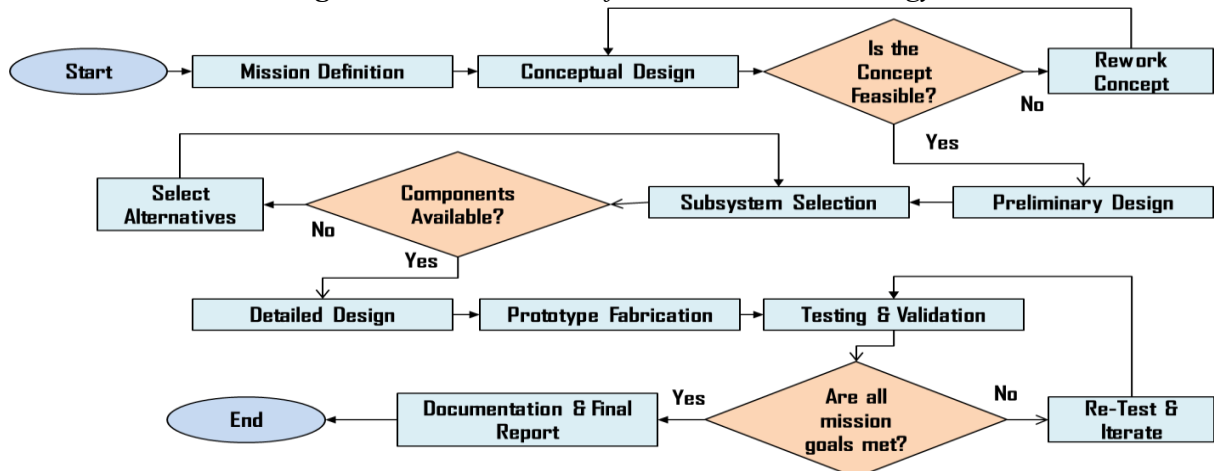


*Figure 3.2: Flow chart of design methodology.*

### 3.3 Electrical Components Selection with Comparison

From all the motors in Table 3.1, T-Motor AS2820 880kv was selected. Due to its ability to generate larger thrust, higher efficiency, and increased power output. Although this motor is significantly bigger than all, its exceptional ability to generate higher thrust was the main priority, which will benefit the stability of the UAV and increase payload capacity. This larger thrust means it can achieve greater speeds compared to motors with lower thrust. Also, higher efficiency indicates a higher utilization of input power. The availability of the motor was another big factor in the selection.

**Table 3.1: Comparison of motors according to their thrust, power & efficiency**

| Model                                              | Weight (gm) | Thrust (G) | Battery Support | Power (W) | Efficiency (G/W) |
|----------------------------------------------------|-------------|------------|-----------------|-----------|------------------|
| <b>Emax XA2212-980KV Outrunner</b>                 | 55          | 980        | 2-3S            | 181.2     | 4.85             |
| <b>Sunny sky V2216 900KV outrunner</b>             | 77          | 800        | 3S              | 250       | 3.2              |
| <b>RS2205-2300 2205 2300KV Cooling Series</b>      | 30          | 1024       | 3S              | 478.4     | 2.14             |
| <b>T-motor AS2820 880KV</b>                        | 136         | 2284       | 3-4S            | 626       | 3.64             |
| <b>T-Motor AIR FPV 2205 2650KV Brushless Motor</b> | 25          | 1000       | 2-4S            | 460       | 2.17             |

The 12x6 propellers (see Table 3.2) are recommended as the best choice because they can generate larger thrust when paired with the chosen motor, T-Motor 880KV. For maximum thrust, the given propeller size was suggested according to the motor manufacturer. The size and pitch of the propeller blades contribute to their ability to efficiently convert motor power into thrust, allowing for improved performance and maneuverability. This combination ensures optimal compatibility and effectiveness of the UAV with the added capability of maximum payload capacity.

**Table 3.2: Comparison of different types of propellers**

| Model                                                        | Weight (gm) | Shaft Diameter (mm) | Quantity |
|--------------------------------------------------------------|-------------|---------------------|----------|
| <b>1245 12×4.5 12 Inch Carbon Nylon CW/CCW Propeller EPP</b> | 20          | 6                   | 2        |
| <b>12×6.0 Carbon Fiber Propellers CW/CCW</b>                 | 44          | 6                   | 2        |
| <b>1045 Carbon Nylon</b>                                     | 25          | 9.5                 | 2        |
| <b>12×4.5 Carbon Fiber Propellers CW/CCW</b>                 | 20          | 8                   | 2        |
| <b>1147 Carbon Nylon</b>                                     | 20          | 9.5                 | 2        |

**Table 3.3: Comparison of different types of electric speed controllers (ESC)**

| <b>Model</b>                                                  | <b>Weight<br/>(gm)</b> | <b>Continuous<br/>Current<br/>(A)</b> | <b>Battery<br/>Support</b> | <b>BEC Mode</b> | <b>Programmable</b> |
|---------------------------------------------------------------|------------------------|---------------------------------------|----------------------------|-----------------|---------------------|
| <b>HW30A 30A<br/>ESC</b>                                      | 27                     | 30                                    | 2-3S                       | Yes 5V/3A       | No                  |
| <b>HITSAN<br/>HTIRC Hornet<br/>2-6S 40A<br/>Brushless ESC</b> | 43                     | 40                                    | 2-6S                       | Switch<br>5V/4A | Yes                 |
| <b>Emax BLHeli<br/>50A ESC with<br/>5V3A BEC</b>              | 41                     | 50                                    | 2-6S                       | Yes, Linear     | Yes                 |
| <b>ZTW Flash 30A<br/>Brushless ESC</b>                        | 11                     | 30                                    | 2-4S                       | No              | Yes                 |

From Table 3.3, the Emax BLHeli 50A ESC with a 5V 3A BEC is ideal for this purpose, offering reliable performance, robust power handling, and integrated features that support both motor control and power supply needs, making it well-suited for the demands of VTOL UAV operations. The recommended continuous current and features like programmable were the key selection factors.

**Table 3.4: Comparison of Servo Motors according to Torque, Speed**

| <b>Model</b>                                                      | <b>Weight<br/>(gm)</b> | <b>Torque<br/>(kg-cm)</b> | <b>Operating<br/>Voltage (V)</b> | <b>Speed<br/>(sec/60°)</b> |
|-------------------------------------------------------------------|------------------------|---------------------------|----------------------------------|----------------------------|
| <b>Analog Feedback Servo<br/>MG996R</b>                           | 55                     | 9.4/11                    | 4.8-6.6                          | 0.15/0.19                  |
| <b>DS Servo DS3218 20KG</b>                                       | 60                     | 19/21.5                   | 4.8-6.8                          | 0.16                       |
| <b>TD-8320MG 20kg<br/>Waterproof Digital Metal<br/>Gear Servo</b> | 60                     | 17.2/20.5                 | 4.8-6.6                          | 0.17/0.19                  |
| <b>Hiwonder LDX-227<br/>Double Shaft Digital Servo</b>            | 60                     | 15/17                     | 6-8.4                            | 0.16                       |

From Table 3.4, the TD-8320MG 20KG is an ideal choice for VTOL UAVs due to its high torque of 20 kg-cm, which ensures it can handle significant loads, and its fast response speed, which is essential for the quick adjustments required during vertical takeoff and landing. It provides the necessary torque and speed to adjust control surfaces and other movable parts. The metal gear

servo is also waterproof, which provides additional protection from moisture and rain.

The following Table 3.5 shows the equipment used in the process of building a VTOL with a fixed-wing tilt-rotor UAV-

**Table 3.5: Specifications & Weight estimation of equipment used in the project**

| Items             | Quantity | Description                                                          | Weight(gm)     | Remarks |
|-------------------|----------|----------------------------------------------------------------------|----------------|---------|
| Motors (BLDC)     | 2        | <i>T-motor AS2820<br/>880KV</i>                                      | 136*2          | [29]    |
| Propellers        | 2        | <i>12×6.0 Carbon Fiber<br/>Propellers CW/CCW</i>                     | 44             | [29]    |
| Battery           | 1        | <i>Red Volcano 11.1V<br/>3S li-po 5200mah</i>                        | 370            | [30]    |
| Flight Controller | 1        | <i>Teensy 4.0</i>                                                    | 10             | [29]    |
| ESC               | 2        | <i>Emax BLHeli 50A<br/>ESC with 5V3A BEC</i>                         | 41*2           | [29]    |
| Servo             | 2        | <i>DS Servo DS3218<br/>20KG Digital Metal<br/>Servo</i>              | 60*2           | [30]    |
| RC Receiver       | 1        | <i>Fly sky IA10B 10CH<br/>Receiver</i>                               | 10             | [29]    |
| Carbon Fiber Tube | 2        | <i>1m long 3K Full<br/>Carbon Fiber Tube</i>                         | 200*2          | [29]    |
| GPS Camera & VTX  | 1        | <i>Ublox NEO 7M<br/>Run Cam Phoenix 2<br/>&amp;<br/>RUSH TANK II</i> | 26<br>16       | [30]    |
| <b>Total-</b>     |          |                                                                      | <b>1350 gm</b> |         |

To achieve the desired functionality for the UAV project, this table outlines the chosen components with their specifications and estimated weights. Key selections include BLDC motors for propulsion, servos for control surfaces, a battery for power, a propeller for thrust, a camera for capturing footage, a VTX for video transmission, a GPS for navigation, and other necessary elements. The total estimated weight of the UAV with these components is approximately 1350 grams.

# Chapter 4

## THEORY AND CALCULATION

## 4.1 Theory

**Lift:** Lift is a fundamental aerodynamic force that acts perpendicular to the direction of motion, which causes the object to rise higher or stay still when opposed by weight. Lift is generated by the pressure difference between the top and bottom of an object. Lift acts opposite to weight, and when the lift force is higher than the weight, the object rises higher. It can be explained by both Bernoulli's principle and Newton's third law. According to Bernoulli's principle, faster-moving air exerts lower pressure at the top, and then the higher-pressure surface pushes the wing upward, which is lifted. According to Newton, air pushes the wing back when the wing pushes air downward. Lift depends on wing shape, angle of attack, and air properties.

Where L is the lift force

$\rho$  is the density of air

$v$  is the velocity of air

$S$  is the platform wing area

$C_L$  is the lift coefficient at the desired angle of attack, Mach number, and Reynolds number

**Thrust:** Thrust is a forward-moving force that is opposite to drag. Thrust force propels an object forward when it is more than the drag and when the lift is counteracted by weight. It is necessary to have a thrust-to-weight ratio greater than 1 for sustained flight or hovering. Thrust depends on the air properties, exit velocity, and area. The equation for thrust is given below,

Where,

$\rho$  is the density of fluid

A is the cross-sectional area of the propeller through which fluid exists

$v_f$  is the final exit velocity

**Drag:** Drag is an aerodynamic force that acts parallel to the direction of motion of the fluid when the object is moving within a fluid or fluid flow when the object is stationary. Drag can be of two types, mainly, i) Parasitic Drag, ii) Induced Drag. Parasitic drag is due to the friction of the object's surface and the surrounding fluid, and Induced drag is due to vortices of fluid from behind the wing when it generates lift.

Here,

D is the Drag of the aircraft

$C_d$  is the drag coefficient

$\rho$  is the density of air

$v$  is the velocity of the air and

S is the area of the wing

## 4.2 Dimensions for calculation

An initial wing length of 1.2m was chosen, while an assumption was made regarding the aircraft's flight speed at 10m/s to 30m/s. Max flight altitude typically ranges from 15 m to 50 m in manual control range with a 1.5 kg UAV (without payload) weight and a typical battery (3S ~ 3300mAh), altitude of 20–30 m is practical.

Let,

Wing length = 1.2m

Wing tube length = 0.75m each, thickness =0.002m, diameter =0.02m

Fuselage = 0.08m height, 0.4m length, 0.1cm width

Tail tube = 0.7m, thickness =0.002m, diameter =0.02m

Elevator = 0.3m

Rudder = 0.1m

Max Payload < 500 g

Max Weight of UAV < 1.5kg

### 4.3 Minimum Success Criteria

- To design a conceptual model with an easy VTOL mechanism that looks aesthetically

descent.

- To develop a prototype & verify the CFD with actual data.

#### 4.4 System Design Approach

Minimum thrust generated by the motor around,  $T_{total} = 4\text{kg}$

Estimated weight around,  $W_{total} = 2\text{kg} = AUW$

The maximum voltage supply to the motor for the required thrust, a 14.8V 4S lipo battery that is 4 cells in series, was chosen.

$$\text{Now, UAV operating time at max load, } t = \frac{I_b \times \text{Discharge}}{\text{AAD}}$$

$$= \frac{3300 \times 0.65 \times 60}{23 \times 1000} = 5.6\text{min}$$

$$P = 170\text{W/kg}$$

$$I_b = \text{Battery Capacity} = 3300\text{mAh}$$

$$\text{AAD} = \frac{AUW \times P}{V} = \frac{2 \times 170}{14.8} = 23\text{A}$$

Motor burnout factor at max. continuous current,  $FOS = t_{I_{max}} / t$

$$= \frac{180}{128} = 1.4$$

Minimum thrust requirement for UAV,  $T_{min} = W_{total} \times 2$

$$= 2 \times 2 = 4\text{kg}$$

With a minimum load factor of 2, each motor 2kg=T

$$\therefore T_{total} = 4\text{kg}$$

$$\text{So, Load Factor} = \frac{T_{total}}{W_{total}} = \frac{4}{2} = 2$$

$$\text{Glide ratio, } \frac{L}{D} = \frac{\text{Horizontal distance traveled}}{\text{Altitude lost}} = \frac{6500}{1000} = 6.5$$

$$\text{Glide Angle, } \gamma = \tan^{-1} \frac{1}{L/D}$$

$$= \tan^{-1} \frac{1}{10} = 8.74$$

$$\text{Wing aspect ratio, } AR = a \frac{L^c}{D}$$

$$= 0.86 (6.5)^{1.3} = 10$$

$$a = \text{glider constant [32]}$$

$$c = \text{glider constant [32]}$$

From Table-4.1:  $S = \frac{(b)^n}{AR}$

$$= 1.2^2/10 = 0.144\text{m}^2$$

Dynamic pressure,  $q = \frac{1}{2} \times \rho(v)^2$

$$= 0.5 \times 1.225(24.5)^2 = 367.65 \text{ Pa [33]}$$

$L = W \cos \gamma = 2 \times 9.81 \cos(8.74) = 19.39 \text{ N}$

$D = W \sin \gamma = 2 \times 9.81 \sin(8.74) = 2.98 \text{ N}$

Lift Coefficient,  $C_L = \frac{L}{qS} = \frac{19.39}{367.65 \times 0.144} = 0.366$

Drag Coefficient,  $C_D = \frac{D}{qS} = \frac{2.98}{367.65 \times 0.144} = 0.056$

$$\frac{C_L}{C_D} = \frac{0.366}{0.056} = 6.5$$

Now, assuming, Taper ratio,  $d = 0.4$ , Sweep angle,  $\lambda = 1.28^\circ$

Chord root,  $C_{root} = \frac{2S}{b(l+d)} = \frac{2 \times 0.144}{1.2(1.28+0.4)} = 0.1428 \text{ m}$

Chord tip,  $C_{tip} = d \times C_{root} = 0.4 \times 0.1428 = 0.0571 \text{ m}$

$$\begin{aligned} \text{Mean Aerodynamic Chord (MAC)}, \bar{c} &= \frac{2}{3} C_{root} \frac{l+d+d^2}{l+d} \\ &= \frac{2}{3} \times 0.1428 \times \frac{1.28+0.4+0.4^2}{1.28+0.4} = 0.10426 \end{aligned}$$

### Reynolds Number,

**For  $v = 5 \text{ m/s}:$**

$$R_e = \frac{v \bar{c}}{\nu} = \frac{5 \times 0.10608}{1.89 \times 10^{-5}} = 28063.5$$

**For  $v = 20 \text{ m/s}:$**

$$R_e = \frac{v \bar{c}}{\nu} = \frac{20 \times 0.10608}{1.89 \times 10^{-5}} = 112,254$$

The following Table 4.1 details the final design parameter of the UAV after calculation,

**Table 4.1: Design Parameters of the UAV**

|                                         |      |
|-----------------------------------------|------|
| Wing of span (b)                        | 1.2m |
| Chord length (c)                        | 0.2m |
| Width of wing (w)                       | 0.2m |
| Width of the fuselage (w <sub>f</sub> ) | 0.1m |

|                                           |                      |
|-------------------------------------------|----------------------|
| Maximum thickness of the airfoil          | 0.02m                |
| Area of wing (s)                          | 0.144 m <sup>2</sup> |
| Root Chord, (C <sub>r</sub> )             | 0.1428m              |
| Tip Chord (C <sub>t</sub> )               | 0.05712m             |
| Oswald efficiency (e)                     | 0.8                  |
| Maximum flight velocity (V <sub>∞</sub> ) | 10-30 m/s            |
| Aspect ratio (AR)                         | 6.5                  |
| Taper ratio, ( $\lambda$ )                | 0.4                  |
| Mean Aerodynamic Chord, (MAC)             | 0.10426              |
| Sweep angle                               | 0 degree             |
| Airfoil                                   | NACA 4412            |
| Weight of the aircraft                    | 1.5kg                |
| Payload capacity                          | 0.5kg                |

A parametric study (see Table 4.2) was conducted to determine the optimal wing loading for the UAV. Three wing loading values were taken from the glider's general wing loading and aerodynamic properties, for each was calculated to optimize. The wing loading of 20kg/m<sup>3</sup> was selected for the following reasons,

- **Moderate Wing Loading:** A wing loading of 20kg/m<sup>3</sup> offers a balance between higher wing loading due to reduction of maneuverability and higher structural weight, and lower wing loading at lower lift and longer takeoff and landing distance.
- **Optimized Aerodynamic Performance:** The corresponding aerodynamic parameters, like lift, lift-to-drag ratio, and lift coefficient, demonstrated favorable values at this wing loading.
- **Structural Consideration:** Without compromising strength or weight, this wing loading allows reasonable wing structure

While the other wing loadings were also a viable option, the middle value was ultimately chosen for this reason, for the best overall performance.

The following Table 4.2 is the calculated numerical value of the required different wing parameters of VTOL UAV:

**Table 4.2: Numerical Value of Different Parameters According to Different Wing Loading (W/S) Ratios**

| Parameter                                            | W/S = 10<br>(kg/m <sup>2</sup> ) | W/S = 20<br>(kg/m <sup>2</sup> ) | W/S = 30<br>(kg/m <sup>2</sup> ) | Units          |
|------------------------------------------------------|----------------------------------|----------------------------------|----------------------------------|----------------|
| Wing Aspect ratio (AR)                               |                                  | 10                               |                                  | -              |
| V <sub>∞</sub>                                       |                                  | 24.5                             |                                  | -              |
| Glide angle (γ)                                      |                                  | 8.74                             |                                  | deg            |
| b                                                    | 1.414                            | 1.2                              | 0.8165                           | m              |
| S (m <sup>2</sup> )                                  | 0.2                              | 0.144                            | 0.067                            | m <sup>2</sup> |
| Total weight including payload (W <sub>total</sub> ) |                                  | 19.62                            |                                  | N              |
| Height                                               |                                  | 1000                             |                                  | m              |
| Distance                                             |                                  | 6500                             |                                  | m              |
| Glide ratio(L/D)                                     |                                  | 10                               |                                  | -              |
| L                                                    |                                  | 19.39                            |                                  | N              |
| D                                                    |                                  | 2.98                             |                                  | N              |
| Lift Coefficient (C <sub>L</sub> )                   | 0.319                            | 0.366                            | 0.95                             | -              |
| Drag Coefficient (C <sub>D</sub> )                   | 0.0318                           | 0.056                            | 0.095                            | -              |
| C <sub>L</sub> /C <sub>D</sub>                       |                                  | 6.5                              |                                  | -              |
| Lambda                                               |                                  | 0.4                              |                                  | -              |
| Chord root                                           | 0.2021                           | 0.1428                           | 0.1172                           | m              |
| Chord tip                                            | 0.08084                          | 0.0571                           | 0.0469                           | m              |
| Mean Aerodynamic Chord (MAC)                         | 0.15                             | 0.10426                          | 0.087                            | m              |

## 4.5 Graphical Comparison of Estimated Data

The graphs (Figure 8.2) show the comparative analysis of lift coefficient (C<sub>L</sub>), drag coefficient (C<sub>D</sub>) & their ratios concerning angle of attack (α).

Let's take the angle of attack, α = 10° and operating speed = 10-30 m/s [due to structural limitation]

At primary design conditions using NACA 4412 airfoil, which is an asymmetric airfoil.

From the C<sub>L</sub> vs α graph, lift coefficient, C<sub>L</sub>=1.3 [35]

So, Lift will be L = ½ × ρ(v)<sup>2</sup> × S C<sub>L</sub>

$$= \frac{1}{2} \times 1.225(10)^2 \times 0.144 \times 1.3$$

$$= 11.466N$$

From the C<sub>L</sub> vs C<sub>D</sub> graph, drag coefficient, C<sub>D</sub>= 0.0312

So, Drag D = C<sub>d</sub> × ½ × ρ(v)<sup>2</sup> × S

$$= 0.0312 \times \frac{1}{2} \times 1.225(10)^2 \times 0.144$$

$$= 0.275N$$

Similarly, at the operating max operating speed 30m/s, the Lift, L = 103.2 N, and Drag, D = 2.48 N.

The theoretical maximum velocity, also referred to as the liftoff velocity, was also determined.

For a safety margin,

$$\text{Stalling Velocity, } V_s = \sqrt{(2W / (\rho \times S \times CL_{\max}))}$$

$$= \sqrt{(2 \times 19.62 / (1.225 \times 0.144 \times 1.3))}$$

$$= 13.08 \text{ m/s} \approx V_{\min}$$

$$\text{Lift-off Velocity, } V_{LO} \approx 1.2 \times V_s = 1.2 \times 13.08 = 15.7 \text{ m/s}$$

The lift-off velocity ( $V_{LO}$ ) computation maintains a velocity that is almost 20% higher than the stalling velocity ( $V_s$ ). Notably, due to its lift-off velocity of 15.7 m/s, the aircraft will not be able to fly at 10 m/s. Because of this, the aircraft is built to fly at a range of 20 to 30m/s.

Calculations reveal that the aircraft generates a lift force of around 11.96 N, equivalent to a mass of 1.2 kg. Considering the aircraft's weight, it has been established that it can support a payload of 1.5 kg, yielding a total mass range of approximately 1.8 kg to 2.0 kg with a 500 g payload. To elevate a 2kg UAV (with payload), the aircraft must attain a minimum velocity of approximately 13 m/s under typical conditions.

## 4.6 Tail Calculation

Assuming,

Horizontal Volume Coefficient,  $V_{HT} = 0.5$

Vertical Volume Coefficient,  $V_{VT} = 0.02$

Horizontal Volume Coefficient,  $V_{HT} = 0.5$

Longitudinal Horizontal Tail,  $L_{HT} = 60\% \text{ of } W_o$   
 $= 0.12$

Longitudinal Vertical Tail,  $L_{VT} = 0.12$

Elevator,  $b = 0.3 \text{ m}$

Rudder = 0.1m

Fuselage length,  $aW_o^c$  where  $W_o = 8\text{-}10\% \text{ of } W$

$$= 0.86(0.2)^{0.48}$$

$$= 0.347 \text{ m} \sim 0.4 \text{ m}$$

The specifications of the horizontal tail of the UAV are shown in *Table 4.3 (a)*. The volume coefficient is a dimensionless parameter of the tail section, which is always in between 0.3-0.6. For this project, the value of the volume coefficient is 0.5.

In *Table 4.3 (b)*, in the case of the vertical tail, the volume coefficient always remains between 0.02 to 0.05.

**Table-4.3: Horizontal & Vertical tail parameters**

| <b>For Horizontal Tail<br/>(a)</b>                                                                                                 | <b>For Vertical Tail<br/>(b)</b>                                                                                                    |
|------------------------------------------------------------------------------------------------------------------------------------|-------------------------------------------------------------------------------------------------------------------------------------|
| <b>Assuming,</b><br><b>aspect ratio =8; taper ratio=0.4</b>                                                                        | <b>Assuming,</b><br><b>aspect ratio=1.75; taper ratio=0.5</b>                                                                       |
| $S = \frac{(b)^n}{AR} = \frac{0.3^2}{8} = 0.0113$                                                                                  | $S = \frac{(b)^n}{AR} = \frac{0.1^2}{1.75} = 0.0057$                                                                                |
| <b>Chord root, <math>C_{root} = \frac{2S}{b(l+d)} = \frac{2 \times 0.0113}{0.3(1+0.4)}</math></b><br>= 0.054m                      | <b>Chord root, <math>C_{root} = \frac{2S}{b(l+d)} = \frac{2 \times 0.0057}{0.1(1+0.5)}</math></b><br>= 0.076m                       |
| <b>Chord tip, <math>C_{tip} = d \times C_{root} = 0.4 \times 0.054</math></b><br>= 0.0216m                                         | <b>Chord tip, <math>C_{tip} = d \times C_{root} = 0.5 \times 0.076</math></b><br>= 0.038m                                           |
| $MAC, \ddot{c} = \frac{2}{3} C_{root} \frac{l+d+d^2}{l+d}$<br>$= \frac{2}{3} \times 0.054 \times \frac{1+0.4+0.4^2}{1+0.4} = 0.04$ | $MAC, \ddot{c} = \frac{2}{3} C_{root} \frac{l+d+d^2}{l+d}$<br>$= \frac{2}{3} \times 0.076 \times \frac{1+0.5+0.5^2}{1+0.5} = 0.059$ |
| <b>V<sub>HT</sub> - 0.5</b>                                                                                                        | <b>V<sub>VT</sub> - 0.02</b>                                                                                                        |
| <b>L<sub>HT</sub> - 0.12</b>                                                                                                       | <b>L<sub>VT</sub> - 0.12</b>                                                                                                        |
| <b>Aspect ratio - 8</b>                                                                                                            | <b>Aspect ratio - 1.75</b>                                                                                                          |
| <b>Span - 0.3</b>                                                                                                                  | <b>Span - 0.1</b>                                                                                                                   |
| <b>Sweep - 35°</b>                                                                                                                 | <b>Sweep - 27.5°</b>                                                                                                                |

## 4.7 UAV Performance Estimation Code

This section of the report details the code used to estimate the performance of the VTOL UAV in MATLAB. The code takes user input for various parameters and calculates flight time, aerodynamic properties, and wing characteristics. Calculations were performed using MATLAB software for computational efficiency [37].

**Code:**

```
% Constants
air density = 1.225; % kg/m^3 (at 40°C)

% Define Glider Constants
a = 0.86;
```

```

c = 1.3;

% Wing Span (assuming a fixed value for now)
wingspan = 1.2;

% User Input
weight = input('Enter weight of the UAV (kg): ');
battery_Mah = input('Enter battery size in Mah: ');
motor_count = input('Enter number of motors: ');

% Battery Calculations
discharge_rate = input('Enter battery discharge rate (C): ');
battery_capacity_ah = battery_Mah / 1000;

% Motor Calculations
motor_thrust = input('Enter motor thrust per motor (kg): ');
total_thrust = motor_thrust * motor_count;
peak_motor_current = input('Enter peak motor current (A): ');

% Combined Motor Average Current Draw (limited by battery or motor)
avg_current_draw = (peak_motor_current*2)/3;

% Flight Time Estimation
flight_time_minutes = (battery_capacity_ah*60) / avg_current_draw;

% Load Factor
load_factor = total_thrust / weight;

% Wing Design
distance = input('Enter horizontal distance traveled (m): ');

% Glide Ratio with corrected formula (using the user-entered distance)
glide_ratio = distance / 1000;
glide_angle = tan(1 / glide_ratio);

% Aspect Ratio with corrected formula
aspect_ratio = a * power(glide_ratio, c);

% Wing Area with corrected formula (use calculated aspect ratio)
wingarea = wing_span^2 / aspect_ratio;

% User Input for Average Air Velocity
avg_velocity = input('Enter average air velocity (m/s): ');

% Dynamic Pressure Calculation
dynamic_pressure = 0.5 * air_density * avg_velocity^2;
fprintf('Dynamic Pressure: %.2f Pa\n', dynamic_pressure);

% Lift and Drag with corrected formulas
lift = weight * cos(glide_angle);

```

```

drag = weight * sin(glide_angle);

% Lift and Drag Coefficients
lift coefficient = lift / (dynamic_pressure * wing_area);
drag coefficient = drag / (dynamic pressure * wing area);

% Coefficient Ratio
coefficient ratio = lift_coefficient / drag_coefficient;

% Taper Ratio and Sweep Angle
taper_ratio = 0.4;
sweep_angle = 0; % degrees

% Wing Chords
root_chord = 2 * wing_area / ((1 + taper_ratio) * wing_span);
tip_chord = root_chord * taper_ratio;
mean_aerodynamic_chord = (2 * wing_area) / (wingspan * (1 + taper_ratio + sqrt(taper_ratio)));

% Display Results
fprintf('Flight Time (estimated): %.2f minutes\n', flight_time_minutes);

fprintf('Load Factor: %.2f\n', load_factor);
fprintf('Glide Ratio: %.2f\n', glide_ratio);
fprintf('Glide Angle: %.2f degrees\n', rad2deg(glide_angle));
fprintf('Aspect Ratio: %.2f\n', aspect_ratio);
fprintf('Wing Area: %.2f m^2\n', wing_area);
fprintf('Lift: %.2f N\n', lift);
fprintf('Drag: %.2f N\n', drag);
fprintf('Lift Coefficient: %.2f\n', lift_coefficient);
fprintf('Drag Coefficient: %.2f\n', drag_coefficient);
fprintf('Coefficient Ratio: %.2f\n', coefficient_ratio);
fprintf('Root Chord: %.2f m\n', root_chord);
fprintf('Tip Chord: %.2f m\n', tip_chord);
fprintf('Mean Aerodynamic Chord: %.2f m\n', mean_aerodynamic_chord);

```

#### Input Parameters:

Enter weight of the UAV (kg): 1.5  
 Enter number of motors: 2  
 Enter motor thrust per motor (kg): 2.5  
 Enter peak motor current (A): 30  
 Enter battery size in mAh: 3300  
 Enter battery discharge rate (C): 65  
 Enter horizontal distance traveled (m): 6500  
 Enter average air velocity (m/s): 24.1  
 Enter wing span (m) [suggested: 1.2]: 1.2

#### Output Parameters:

--- UAV Design Parameters ---  
 UAV Total Weight (AUW): 2.00 kg  
 Battery Capacity: 3300 mAh  
 Battery Voltage: 14.8 V  
 Discharge Rate (C): 0.65  
 Average Ampere Draw (AAD): 22.97 A  
 Flight Time (estimated based on new formula): 5.60 minutes  
 Load Factor (Thrust/Weight): 2.50  
 Glide Ratio (based on input distance/altitude): 6.50  
 Glide Angle: 8.75 degrees  
 Aspect Ratio (calculated): 9.80  
 Wing Span (user input/default): 1.20 m  
 Wing Area (calculated): 0.15 m^2  
 Lift (estimated): 1.98 N  
 Drag (estimated): 0.30 N  
 Dynamic Pressure: 355.75 Pa  
 Lift Coefficient: 0.0378  
 Drag Coefficient: 0.0058  
 Coefficient Ratio (Cl/Cd): 6.50  
 Root Chord (modified formula): 0.1458 m  
 Tip Chord (modified formula): 0.0583 m  
 Mean Aerodynamic Chord (MAC) (modified formula): 0.1064 m

# Chapter 5

## DESIGN

### 5.1 Structure Design

The Structural design process was followed systematically to establish a solid base for the physical development of the UAV. It started by choosing an airfoil appropriate for it and then conducting aerodynamic analysis and iterative CAD design. Each step was to determine whether the UAV design can fulfill performance, stability, and efficiency needs for VTOL flight. To initiate the UAV structural design process, these steps were followed-

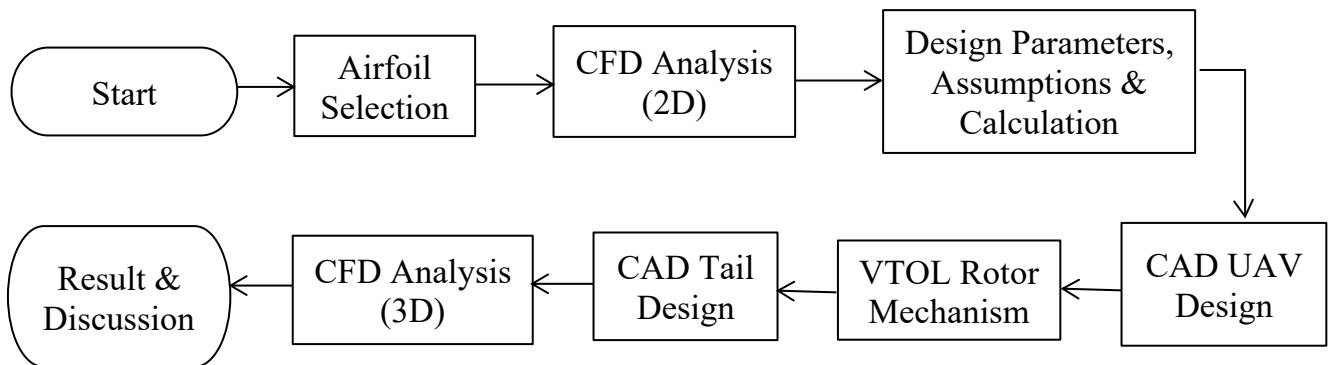


**Figure 5.1:** Block Diagram of Structural Design Process

#### 5.1.1 Airfoil Selection

There are various airfoil shapes to choose from, depending on the specific requirements. Here, some of the suitable airfoil shapes are compared,

**Table 5.1:** Comparative Illustration of Different Types of Airfoils

| Airfoil         | Description                                         | Advantages of Low Drag                                | Disadvantages                                                 | Best Use Cases                       |
|-----------------|-----------------------------------------------------|-------------------------------------------------------|---------------------------------------------------------------|--------------------------------------|
| NACA 2415       | Symmetrical airfoil, 15% thick                      | Relatively thin profile for low drag at high speeds   | Lower lift coefficient compared to some asymmetrical airfoils | Sailplanes, high-performance gliders |
| NACA 63 (1)-012 | Symmetrical airfoil, 12% thick                      | Thin profile for good cruise performance              | Lower lift coefficient compared to some asymmetrical airfoils | Powered gliders, high-speed UAVs     |
| Eppler 205      | Semi-symmetrical airfoil, designed for laminar flow | Exceptionally low-drag characteristics at high speeds | Requires a smooth surface finish for laminar flow, less       | Sailplanes, high-performance         |

|                           |                                                                  |                                                                          |                                                                            |                                                    |
|---------------------------|------------------------------------------------------------------|--------------------------------------------------------------------------|----------------------------------------------------------------------------|----------------------------------------------------|
|                           |                                                                  |                                                                          | forgiving of manufacturing imperfections                                   | gliders                                            |
| <b>RG-15</b>              | Reflexed symmetrical airfoil                                     | Good low-drag performance, improves stability at low speeds              | Slightly higher drag compared to a non-reflexed airfoil at high speeds     | Electric-powered gliders, general-purpose UAVs     |
| <b>Selig S7032</b>        | Very thin symmetrical airfoil, designed for low Reynolds numbers | Excellent low-drag performance at low air speeds (common for small UAVs) | A very thin profile might be more susceptible to structural issues         | Micro air vehicles (MAVs), low-speed gliders       |
| <b>NACA 4412</b>          | Symmetrical airfoil, 12% thick                                   | Good balance between low drag and lift coefficient                       | Not the most optimized for either low drag or high lift                    | General-purpose airfoil for various glider designs |
| <b>MS (1)-0317</b>        | Laminar flow airfoil with good low-drag characteristics          | Optimized for laminar flow, good cruise performance                      | Requires a smooth surface finish, sensitive to manufacturing imperfections | Sailplanes, high-performance gliders               |
| <b>Wortmann FX 63-137</b> | Semi-symmetrical airfoil designed for laminar flow               | Very good low-drag characteristics, good lift coefficient                | Requires a smooth surface finish, sensitive to manufacturing imperfections | Sailplanes, high-performance gliders               |
| <b>SD7037</b>             | Very thin symmetrical airfoil                                    | Exceptional low-drag performance at very low Reynolds numbers            | A very thin profile might be more susceptible to structural issues         | Micro air vehicles (MAVs), low-speed gliders       |
| <b>NACA 65(2)-415</b>     | Symmetrical airfoil, 15% thick                                   | Good balance between low drag and moderate lift                          | Not the most optimized for either low drag or high lift                    | General-purpose airfoil for various glider designs |

After eliminating different airfoil shapes based on required low Reynolds number and easy printability the following shapes are left from which the final airfoil will be selected.

### After Eliminating

**Table-5.1(a): Selection of Airfoil**

| Airfoil            | Advantages (Re < 10,000)                                               | Disadvantages                                                                              |
|--------------------|------------------------------------------------------------------------|--------------------------------------------------------------------------------------------|
| <b>Selig S7032</b> | Exceptional low drag at low speeds                                     | Very thin profile, potential structural concerns                                           |
| <b>RG-15</b>       | Good low drag, improved stability at low speeds                        | Slightly thicker profile, minor drag increase at high speeds (not a major concern for you) |
| <b>NACA 4412</b>   | Decent balance of low drag and lift, potentially easier to manufacture | Not the most optimized for low drag at very low Re                                         |

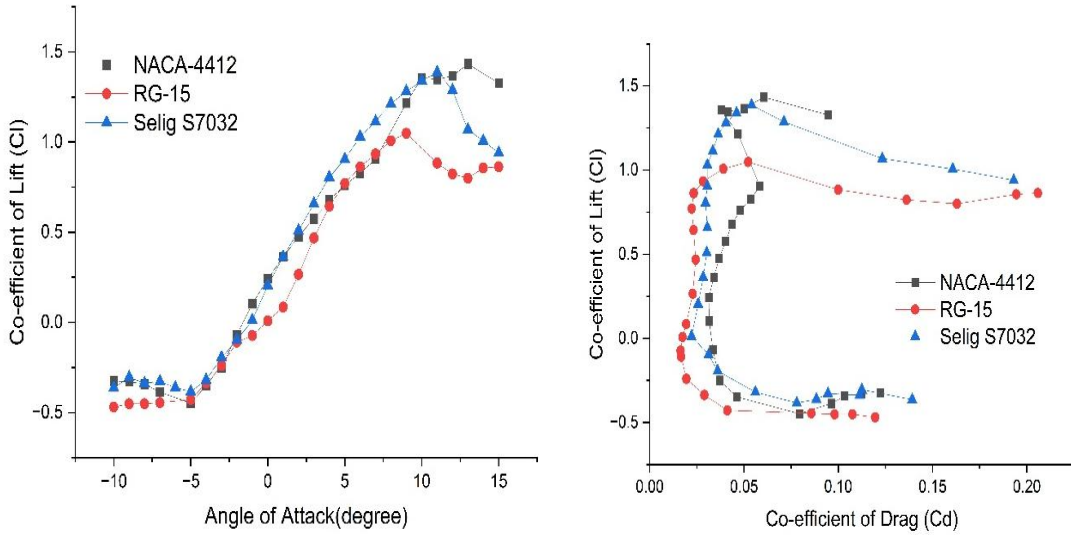


**Figure-5.1(b): Comparison of 3 airfoils with respect to  $C_l$  vs  $\alpha$ ,  $C_l$  vs  $C_d$**

Finally, the selected airfoil shape is NACA 4412 based on the following reasons,

- **Low Drag:** Although this airfoil shape isn't the finest at very low Reynolds numbers, but performs well within the predicted range of the UAV.
- **Low Coefficient:** It offers a good quantity lift, which is essential for gliding with enough speeds at low speeds.
- **Straight  $C_l$  vs AoA graph:** The wing shape has a linear graph between angles -5 and 9 degrees, which gives the freedom to tilt the UAV in a good AoA range.
- **3D Printability:** This wing shape is more forgiving to 3d printing errors as it has a thicker profile. Because a thicker profile creates a structurally robust wing.

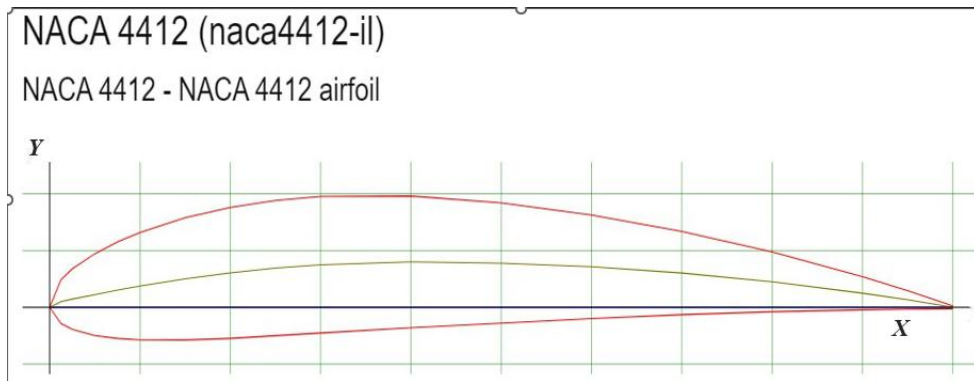


**Figure 5.1 (c): Wing and extremity profile [35].**

The other two types of wing shape were not chosen for the following reason,

**Selig S7032:** Although this wing shape has extremely low drag but requires a precise 3d printer as it has an extremely thin profile and thus is difficult to print. Also, due to this extremely thin profile,

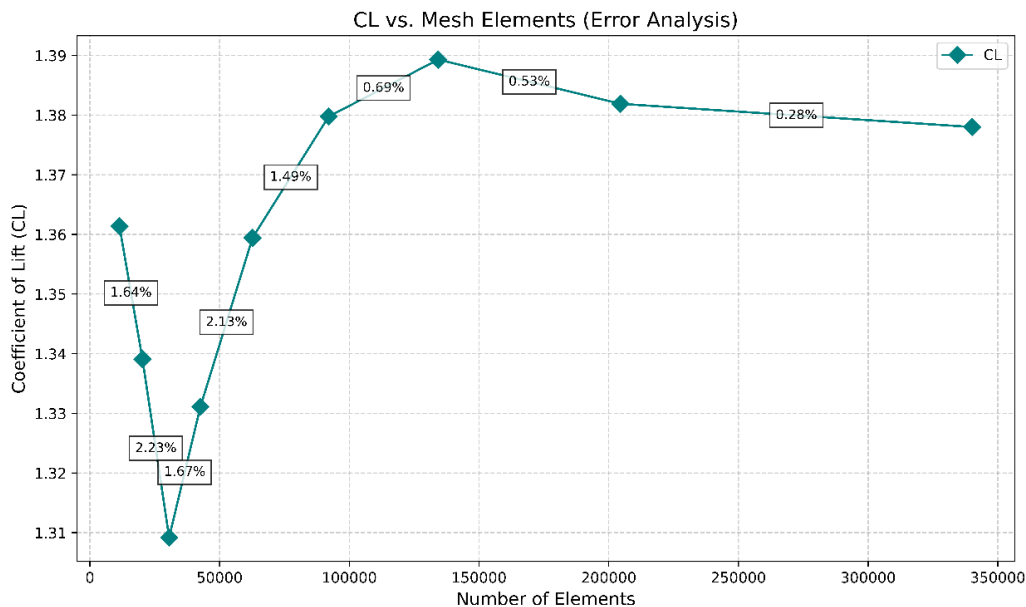
it may become structurally fragile.

**RG-15:** Although, this shape offers better balance and is somewhat easier to print than Selig-S7032 due to thicker profile, still NACA 4412 offers balance between both printability and performance.

### 5.1.2 CFD Analysis (2D)

#### 5.1.2.a Grid Independence Test

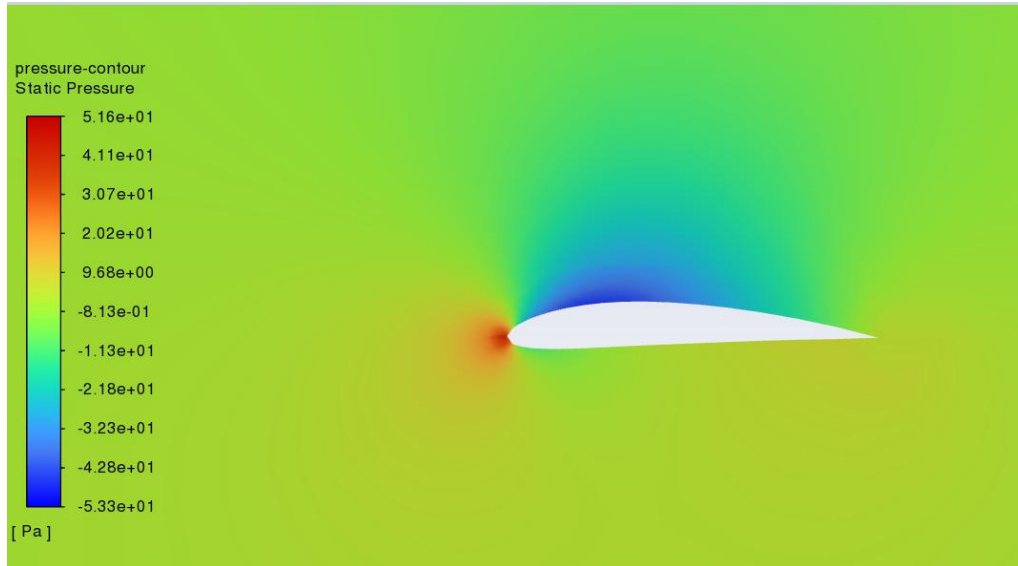
In computational fluid dynamics (CFD), this technique assesses simulation accuracy about the computational grid size. Its goal is to identify the smallest grid size required for reliable results that remain consistent regardless of further grid refinement. This assessment ensures simulations are robust and trustworthy, optimizing computational resources while accurately predicting fluid dynamics and related phenomena. Numerical output provides  $C_L$  stabilization for increasing numbers of mesh cells, with differences below 1% (see Fig. 5.2) for meshes with more than 134,290 cells. The final selected mesh for application in subsequent CFD calculations consists of  $N=204,516$  cells, with a computed error of only 0.53%, guaranteeing accuracy while constraining computational expense. This selection guarantees a feasible output without excessive refinement.



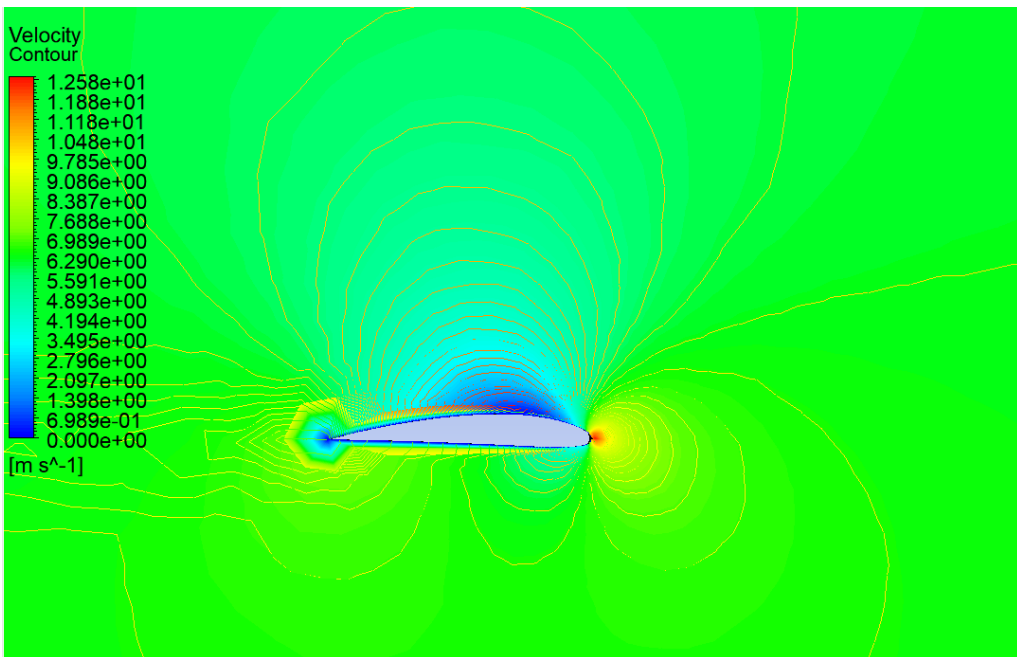
**Figure 5.2:** Grid independence Test.

Figure 5.3 shows the pressure contour on the optimized airfoil. It shows low pressure at the top surface and high pressure at the leading edge, typical of good lift. Figure 5.4 shows a velocity contour with higher flow velocity on the upper surface. This clearly shows a smooth and attached flow on the airfoil. This simulation was executed in ANSYS at a freestream velocity of 10 m/s and

an angle of attack of  $0^\circ$  using the default turbulence models. All these results are suitable for aerodynamic performance with attached flow and correct lifting generation. This confirms the performance of the design in steady flight conditions.



**Figure 5.3:** NACA-4412 airfoil Pressure Contour.



**Figure 5.4:** NACA-4412 airfoil Velocity Contour.

### 5.1.3 UAV CAD Design

Started the design with the wing of the UAV. In the initial design of the wing selected air-foil model (NACA- 4412) were used. The wing length of the UAV is considered 0.6m for each section to obtain a total wingspan of 1.2m, including chord-root 0.1428m & chord-tip 0.0571m.

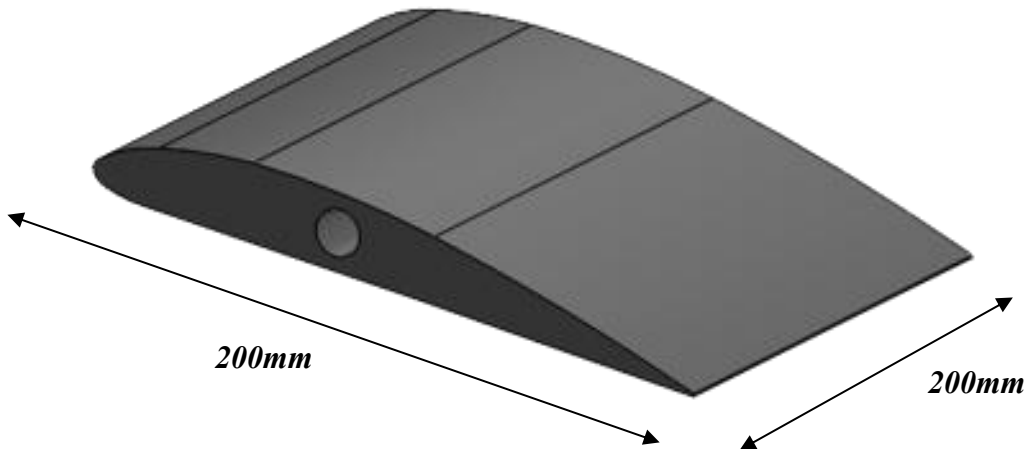


**Figure 5.5:** CAD Model of NACA 4412 Airfoil Based Wing

Using this wing, a base model of the UAV is constructed along with a ( $L \times W \times H = 0.4\text{ m} \times 0.2\text{ m} \times 0.08\text{ m}$ ) fuselage, a tail tube 0.7m & 0.15m elevator at each side. The total weight of the UAV is estimated to be 2kg with a maximum payload of 500 g.

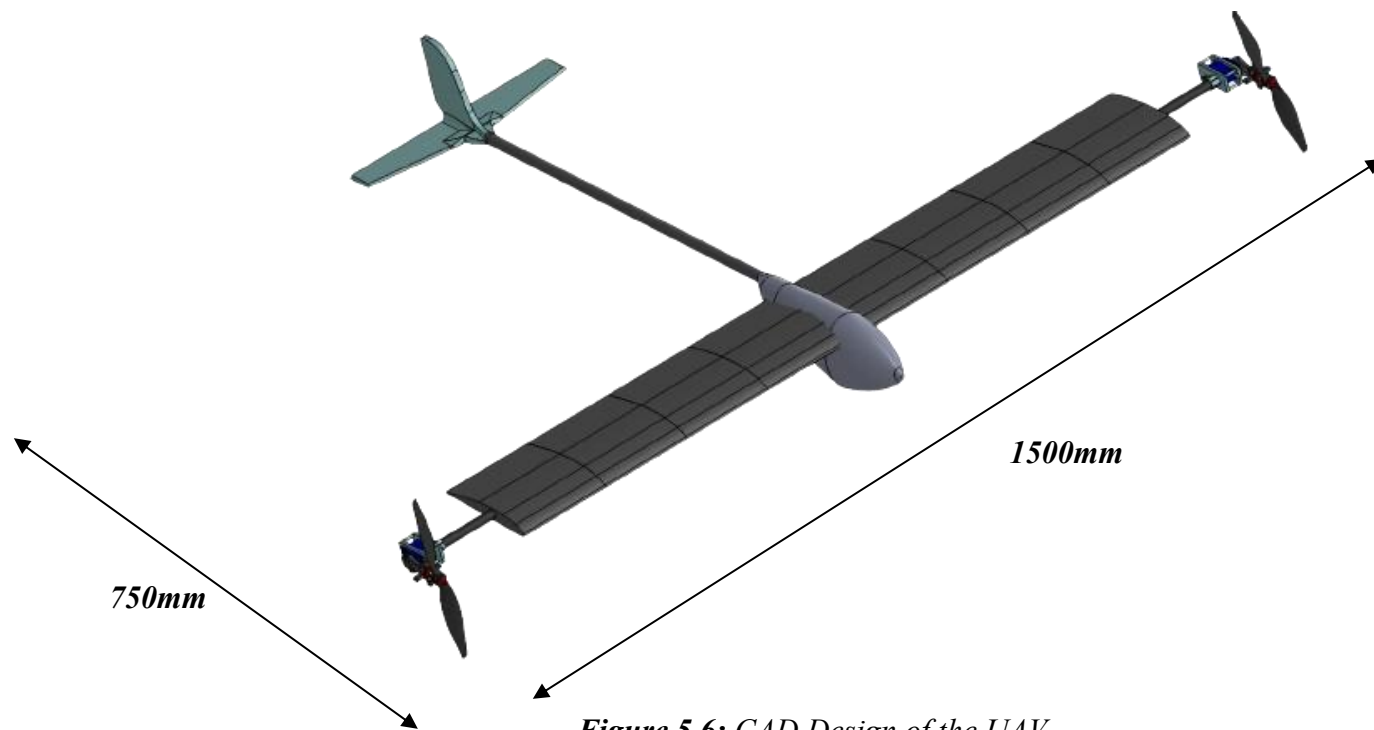


**Figure 5.6:** CAD Design of the UAV.

#### 5.1.4 VTOL Rotor Mechanism

The VTOL (Vertical Take-Off and Landing) UAV tiltrotor has the features of both rotary-wing aircraft and fixed-wing aircraft, that is, to be able to cover distances fast in a forward direction as

well as vertically take off and land. There are several significant elements and functions of the design that work together to enable a seamless transition between the vertical and the horizontal flight positions.

The foundation of the tiltrotor is in the rotors and in the blades. These are mounted on swiveling rotor mounts that are rotated or tilted vertically in take-off, landing, or hovering, and horizontally in forward flight. To achieve maximum efficiency on both designs, the rotor blades are also aerodynamic; they are made of lightweight materials, and mostly they are composite in nature. The tilt mechanism itself is critical, and it comes in the form of nacelles that house the motors, which can then be moved using accurate actuators. These are the electric or hydraulic actuators that rotate the nacelle to make the move between vertical and horizontal flights easy. Such rotors are usually operated with brushless electric motors because of their high reliability and efficiency.

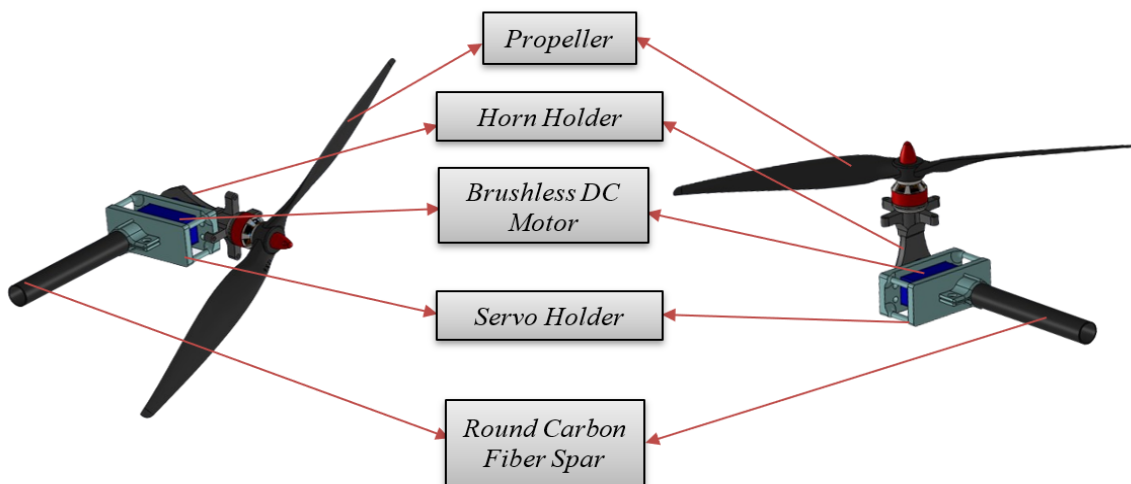


*Figure 5.7: VTOL Rotor Mechanism with Components*

#### 5.1.4.a Working Principle of VTOL

The operation of a VTOL UAV tiltrotor in flight comprises a series of parallel phases through which the air vehicle performs its mode switch between vertical and horizontal flight. First, the head of the UAV is placed vertically, and the UAV is taken off with the rotors straight up. The rotors are driven by brushless electric motors to produce the required upward thrust, and the Flight Control Unit (FCU) continuously regulates rotor speeds and blade pitches to maintain stability and lift, allowing the UAV to hover at any given time.

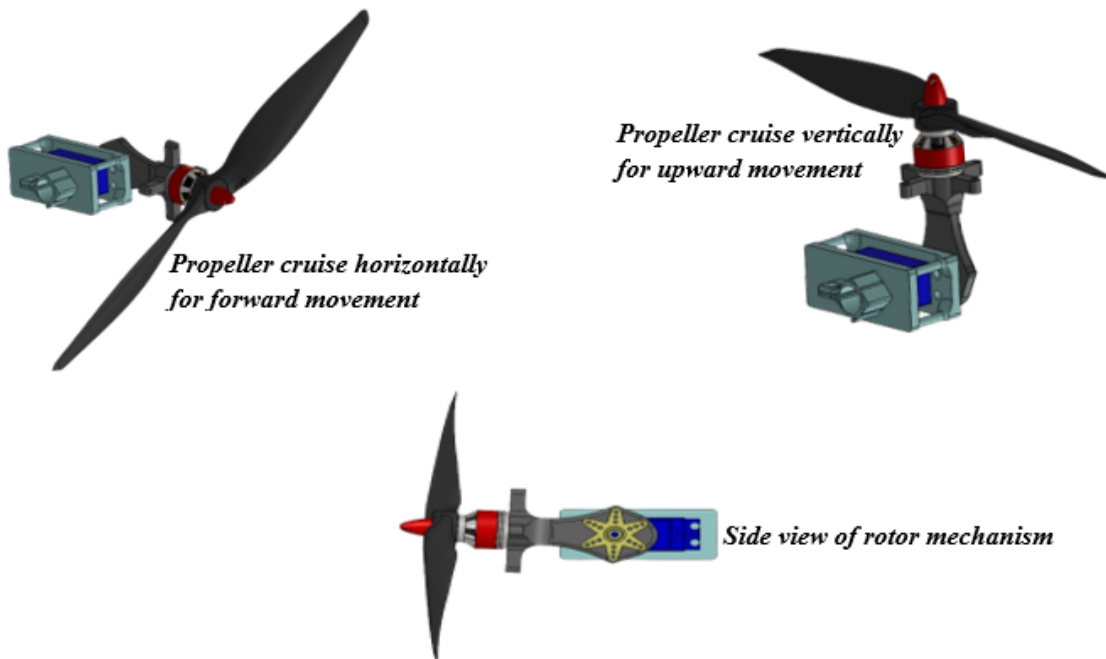


**Figure 5.8:** CAD Design of the VTOL Rotor Mechanism

**Transition to Forward Flight:** The FCU rotates the nacelles (in which the rotors are enclosed) in a gradual rotation, which converts a vertical orientation of the nacelles to a horizontal one. Actuators control this reorientation and closely monitor the angular position of the reorientation, so a smooth and gradual change is achieved. During flight, lifting (as tilted nacelles rotate clockwise), and forward propulsion are delivered by the rotors acting in unison. The FCU, to an extent, cancels out these forces by making adjustments to the rotor speeds and the blade pitches so as to combine vertical lift with the horizontal thrust needed to propel it forward.

**In The Cruising Phase:** Upon placing the nacelles at the horizontal, the rotors adopt a propeller style, offering the necessary pull to move forward for propulsion. At the same time, the wings of UAVs produce an aerodynamic lift, which reduces the reliance on the rotor lift and increases the total flight efficiency. The Flight Control Unit (FCU) controls rotor revolutions and pitch, so that it can maintain a favorable state to carry out stable and efficient forward flight.

**Transition Back to Vertical Flight:** When the transition is made between forward and vertical flight, the FCU begins the nacelles in rotational motion towards vertical orientation. Such a maneuver is planned to be carried out with a very small and exact change in thrust or lift to avoid any immediate change. During the period of passing through the transitional attitude, the rotors are changing the direction of the forward thrust into the vertical lift. The FCU makes the rotor dynamics precise to maintain altitude and aircraft stability throughout the transition.

In landings, the UAV is programmed to land vertically by slowly decreasing the speed of the rotors. The FCU controls the level of descent so that it makes the plane lands gently on the ground. During the landing, the FCU will actively track and update the position and the orientation of the UAV and correct it as required so that a stable landing can be obtained in an orderly and controlled manner.

### 5.1.5 CAD Tail Design

The tail design process flowchart is shown below for the selection of tail configurations based on the requirements for both vertical and horizontal tails.

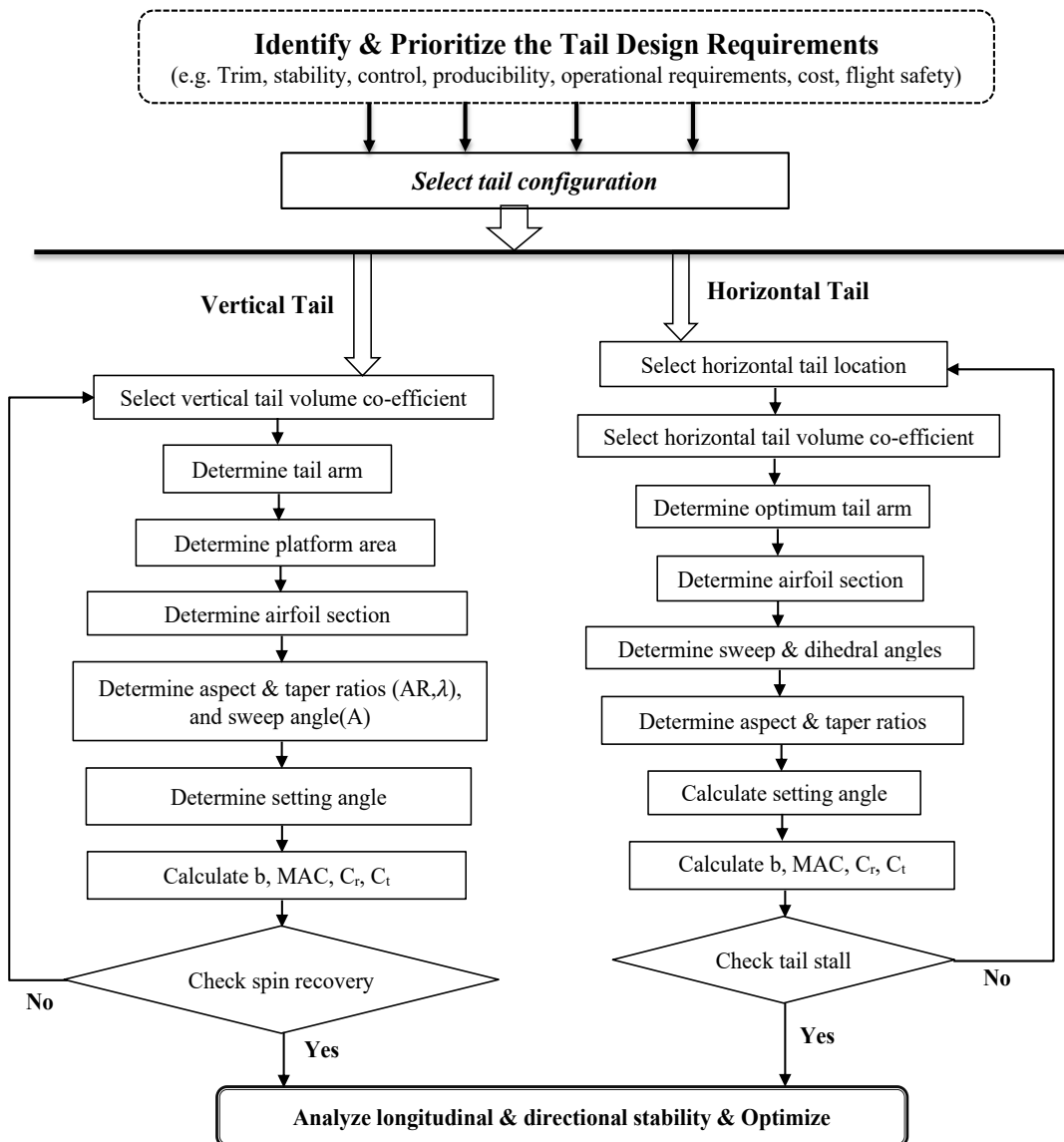


**Figure 5.9:** The tail design procedure.

Following the tail design process outlined in Figure 5.9, the tail configuration was selected, and the detailed calculations for the vertical and horizontal tail surfaces are presented in Section 4.6.

### 5.1.6 Final Design Dimension

The final design section presents the complete 3D model of the UAV, showcasing detailed views and dimensional specifications. These visuals represent the culmination of the structural and aerodynamic design process. Here are the final dimensions of the tilt-rotor VTOL full-body assembled UAV,

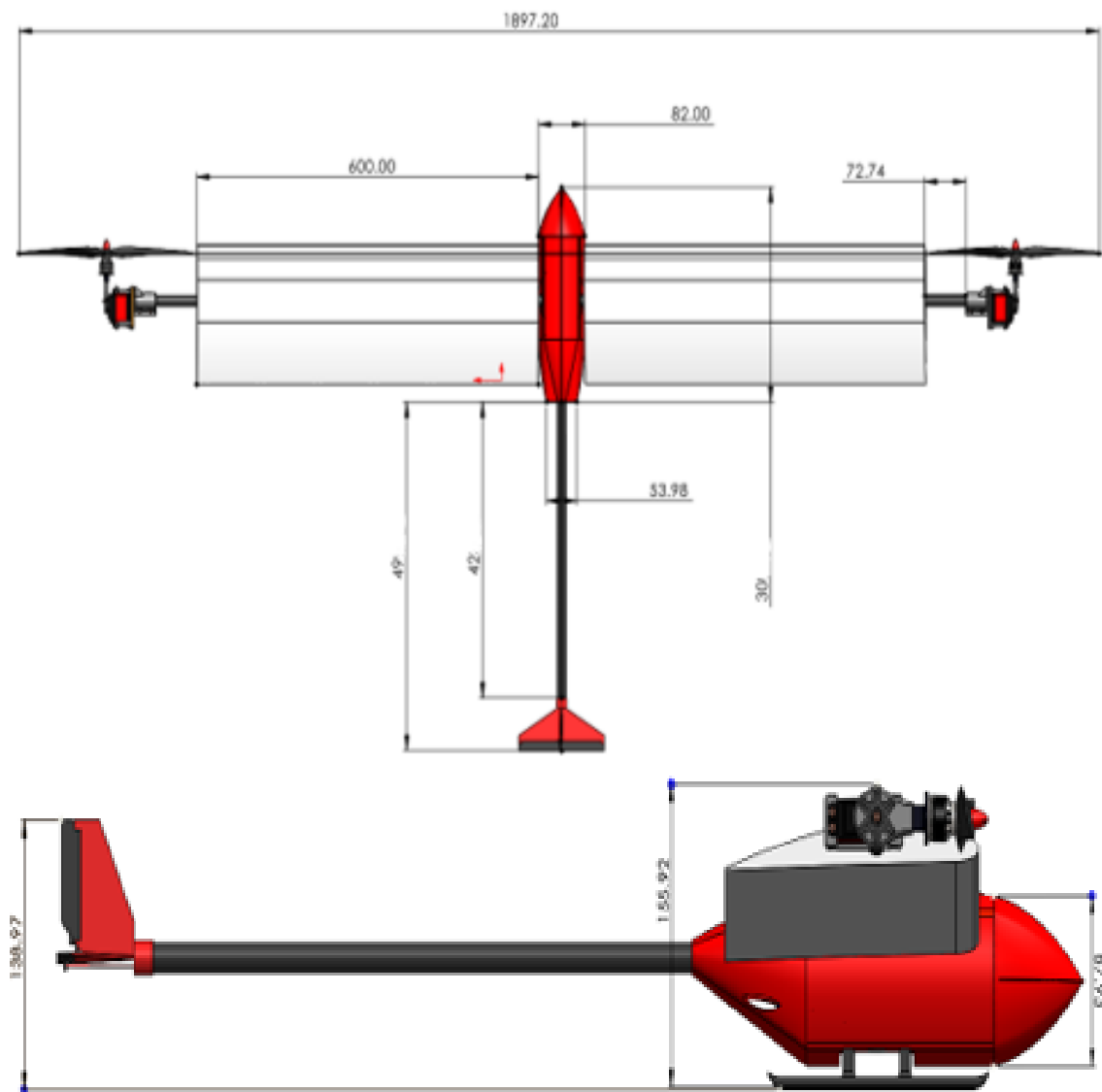


**Figure 5.10:** Dimensions of UAV from top view and side view. (Dimensions in mm)

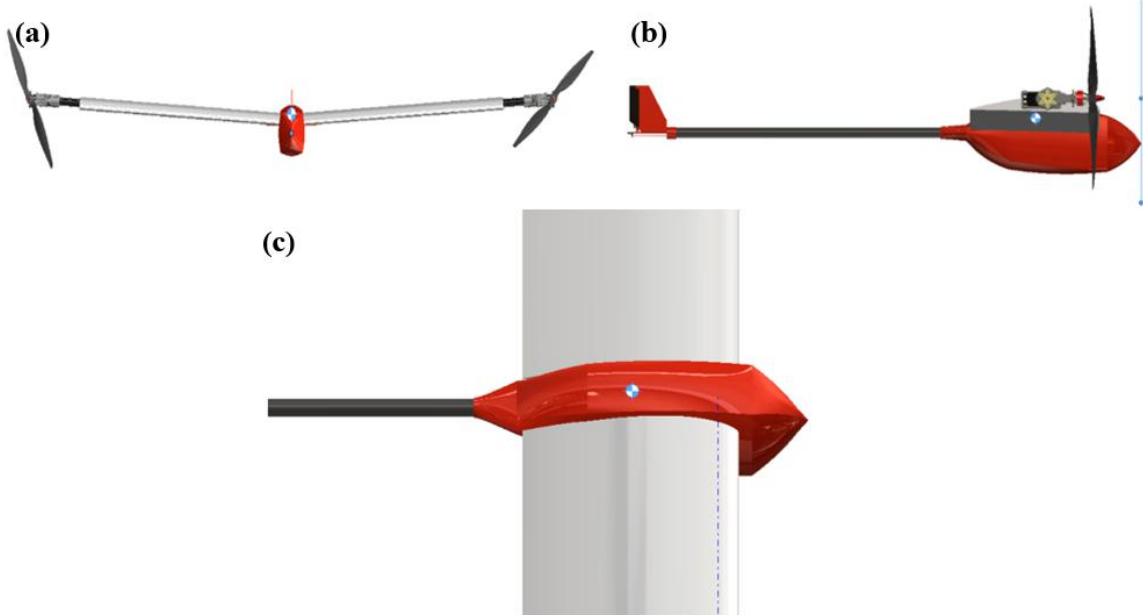
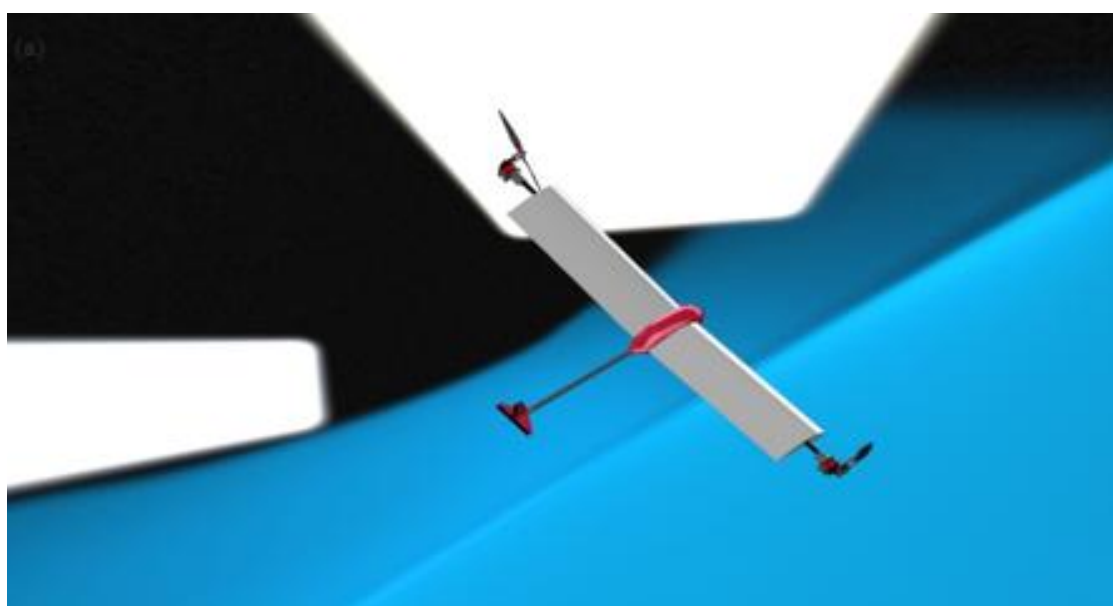
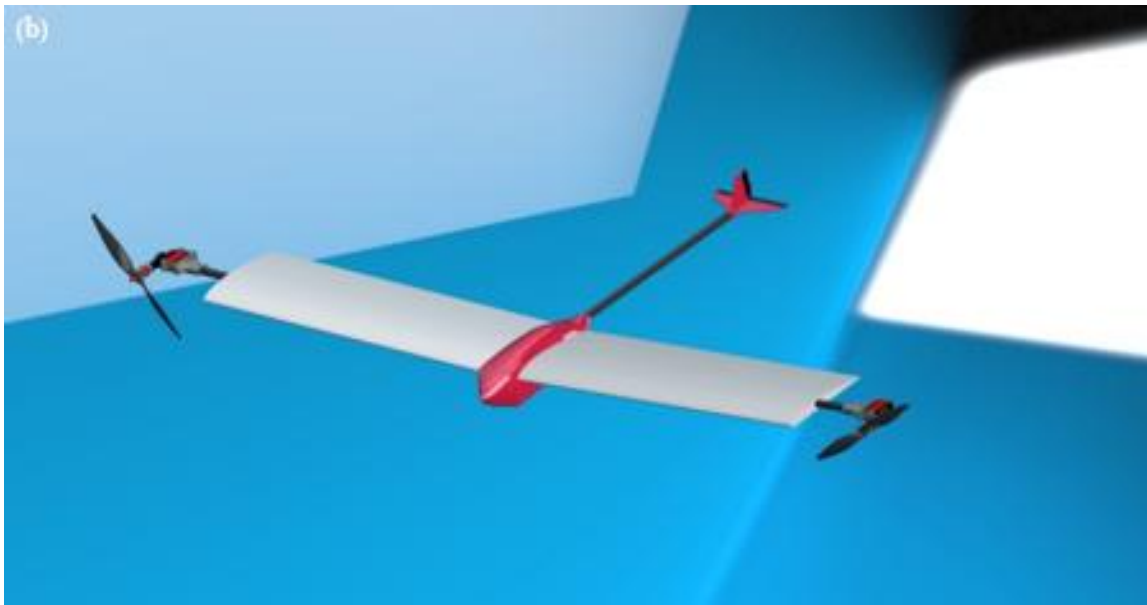


Figure 5.11: The CG location of the full model, a) front side, b) sideview, c) isometric view. Its center of mass (see Fig. 5.11) is at the position (-162.61, 0.05, 38.61) mm concerning the default origin at the nose cone or leading edge of the fuselage. This positions the center of mass approximately 162.61 mm to the rear, 0.05 mm off laterally, and 38.61 mm above the datum for the fuselage, positioning the equilibrium marginally aft and elevated. This type of positioning is critically important for maneuvering and stability for flight dynamics.

### 5.1.7 Final Design Render

These are the final render images of the finished UAV model, which has been designed in SolidWorks.





**Figure 5.11:** Final render of full model UAV a) Top view, b) Front Isometric view.

## 5.2 Control System Architecture and Process

In the meantime, a basic control system based on the initial design of the VTOL UAV is constructed, which is used,

**Brushless Motor:** A brushless motor, or BLDC (Brushless Direct Current) motor, is an electric motor that does not have the mechanical brushes and commutator of the typical brushed motors. Instead, it uses electronic commutation to control the direction of current to the motor windings. This makes it more efficient, less subject to wear and tear, and easier to be more accurate and in control. Brushless motors are most commonly used in electric vehicles, drones, and various industrial equipment that need to be reliable and function well. They are more efficient, more reliable, quieter, and have better speed-torque characteristics than brushed motors.



**Figure-5.12:** T-motor AS2820 880KV [38].

**Servo Motor:** The servo motor is an extremely controlled actuator and is generally used where the control over movement needs to be very fast and precise. It functions by taking a command signal

from the flight controller that tells it where the output must be, and then it uses a feedback system to shift the motion of the motor accordingly. These motors are very essential to the VTOL UAV so that it can smoothly transition from vertical takeoff and landing to horizontal mode of flight without any hitch. Servo motors are small, lighter, and highly responsive. They have the right amount of torque and speed to enable the control to be precise and trustworthy. Electronic signals are provided by the UAV flight controller. The signals can be from the pilot or an onboard autonomous system. VTOL UAV servo motors need to be efficient and reliable to impart stability and maneuverability in cramped spaces.

#### Dimensions



**Figure 5.13:** TD-8320MG 20kg Waterproof Digital Metal Gear Servo[39].

**Lithium Polymer Battery (Li-po):** The most popular battery for UAVs is the Lithium Polymer (LiPo) battery due to its light weight, energy density and its ability to supply high discharge currents. As a result, they are capable of delivering the large discharge current needed to facilitate long flight durations and large payload carrying capacity, ideal for flight-based applications of drones. LiPo batteries allow for a quick supply of power during aggressive maneuvers and exhibit minimal self-discharge. A LiPo battery was used in the project to supply effective and stable power to onboard electronics and propulsion.



**Figure 5.14:** Red Volcano 11.1V 3S Li-PO 5200mAh Battery[29].

**Electric Speed Controller (ESC):** An ESC is used to manage the direction and speed of electric motors by adjusting the power fed to them. It takes input from the flight controller and adjusts

motor speed by using PWM (pulse-width modulation). ESCs are crucial to brushless motors on drones, providing smooth throttle response and overheating protection along with programmability for adjusting performance. ESCs used in the project allow for precise motor control during hovering as well as during flight in the forward direction and help provide stable as well as responsive maneuverability.



**Figure 5.15:** Emax BLHeli 50A ESC with 5V3A BEC [29].

**Propeller:** UAVs utilize propellers for vertical takeoff and landing. Propellers are normally made of composite polymers or carbon fiber. They are light and durable and always provide excellent performance. The vehicle was made capable of taking off, hovering, and landing vertically at slow speeds by lifting it substantially. UAV propeller blades and pitch are normally such that they will maximize flight stability and performance. Variable pitch systems are among the high-tech aspects of some propellers, with the ability of the angles of blades being made adjustable to enhance steering and adapt to changing flying conditions. For VTOL UAVs having high lift, control, and energy efficiency, their propeller design should be taken into account.



**Figure 5.16:** 12×6.0 Carbon Fiber Propellers CW/CCW [29].

**Transmitter & Receiver:** Transmitter and receiver systems are necessary to provide clear communication between the VTOL UAV and the operator. The transmitter is usually worn by the operator and also acts as the control interface to allow precise control of the VTOL UAV. It is usually a hand-held device with real-time telemetry feedback, perhaps with a screen, joysticks,

and other controls. These transmitters usually employ assigned radio frequencies, e.g., 2.4 GHz or 5.8 GHz, to ensure clear communication over a distance. The VTOL UAV incorporates a receiver that picks up signals transmitted by the transmitter. The throttle, pitch, roll, and yaw of the aircraft are controlled by the operator since the receiver responds to the operator's commands. The receiver should accurately and promptly interpret the commands for the flight to succeed.



**Figure 5.17:** Fly sky FS-i6X 2.4GHz 6CH Transmitter [29].

**Microcontroller:** The Teensy 4.0 microcontroller, with its 600 MHz ARM Cortex-M7 processor, was selected for its real-time capability and reliability in UAV flight control. It boasts 1024 KB RAM and 1984 KB Flash storage for effective processing of flight algorithms and sensor inputs. With 40 digital I/O pins, 14 analog inputs, 31 PWM outputs, and 3 SPI and 2 I2C buses support, it offers flexible sensor, ESC, and telemetry module interfacing. Its USB

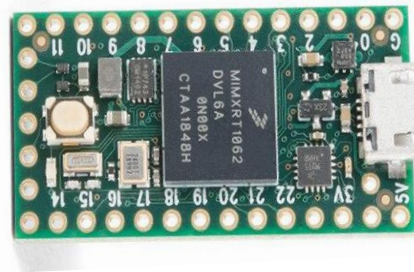


**Figure 5.18:** Teensy 4.0 microcontroller unit [30].

ports offer high-speed communication and debugging. DMA channels, CAN bus support, and onboard cryptographic acceleration offer increased data throughput, protocol interfacing, and security—ideal for small, high-performance aerial systems.

**IMU:** MPU6050 is a 6-DOF IMU used for real-time drone (UAV) orientation estimation. It consists of a 3-axis accelerometer and a 3-axis gyroscope integrated to sense the linear acceleration

and angular speed with accuracy. The gyroscope has a selectable +/-250 to +/-2000 °/s range option with sensitivity from 131 to 16.4 LSB/(°/s). It benefits from low noise (0.05 °/s-rms at 100 Hz), low power usage, and excellent frequency of output of a maximum of 8 kHz. The sensor has stable readings of zero-rate drift as low as  $\pm 20$  °/s and cross-sensitivity as low as  $\pm 2\%$ . Its compact nature and stable operation qualify it for VTOL flight controllers requiring accurate motion sensing and fast response to the controller.

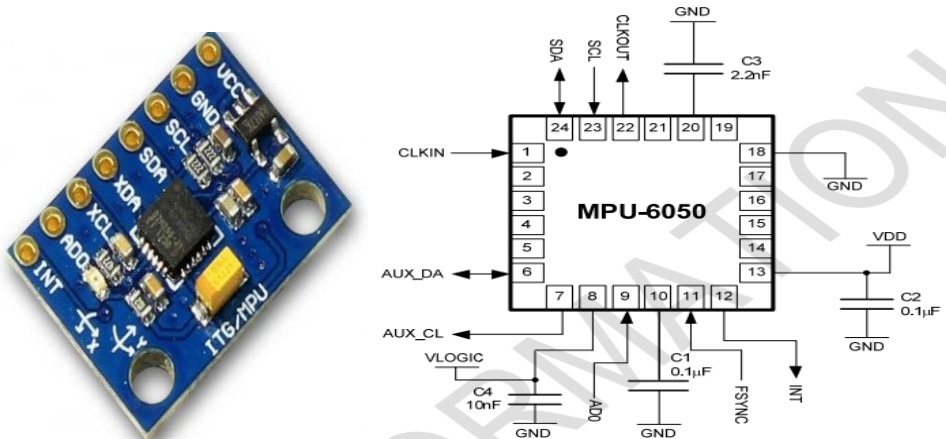


Figure 5.19: MPU-6050 IMU sensor [30].

**SD Card Module:** A Micro SD Card Adapter Module was integrated into the flight controller to facilitate support for post-flight analysis as well as autonomous operation. With an operating voltage range of 4.5V–5.5V, the module itself has an internal 3.3V voltage regulator and utilizes SPI communication for the reliable transmission of the data. It supports FAT file systems and microSD cards of up to 2 GB and SDHC cards of up to 32 GB. It stores key flight parameters like input commands and output signals, and sensor readings. The records stored are used to help debug the system, analyze performance, and perform optimizations of the control algorithms. The data storage helps facilitate such higher-level flight capabilities as predictive control and learning by adapting.

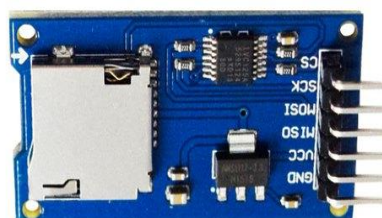


Figure 5.20: Micro SD card module [30].

**Buck Converter:** The Mini-360 buck converter was used for stable voltage regulation of onboard

electronics. It has an input voltage range of 4.75–23 V and an adjustable output of 1–17 V, making it compatible with various power sources. It is able to supply a continuous current of a maximum of 1.8 A (3 A peak) with the MP2307DN regulator and offers high efficiency of up to 95%, with minimal energy lost in the process of conversion. Its switching frequency of 340 kHz ensures good transient response and compact filtering. Mini-360's ~30 mV low output ripple, 160°C thermal shutdown, and compact dimensions (17×11×3.8 mm) make the module well suited to lightweight and efficient UAV applications.

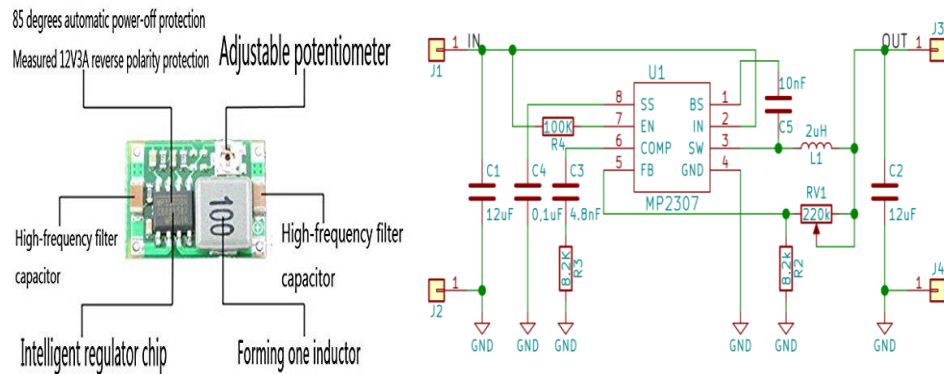


Figure 5.21: Mini 360 buck converter module [30].

### 5.3 Circuit Design

To develop the flight control code, the user-friendly Arduino IDE was employed. This versatile development environment provides a simplified interface for writing and uploading code to Teensy 4.0. The development process was streamlined by leveraging Arduino IDE's intuitive features, allowing for rapid prototyping and testing [40]. The IDE's clear syntax highlighting, code completion, and debugging tools facilitated efficient code development and troubleshooting.

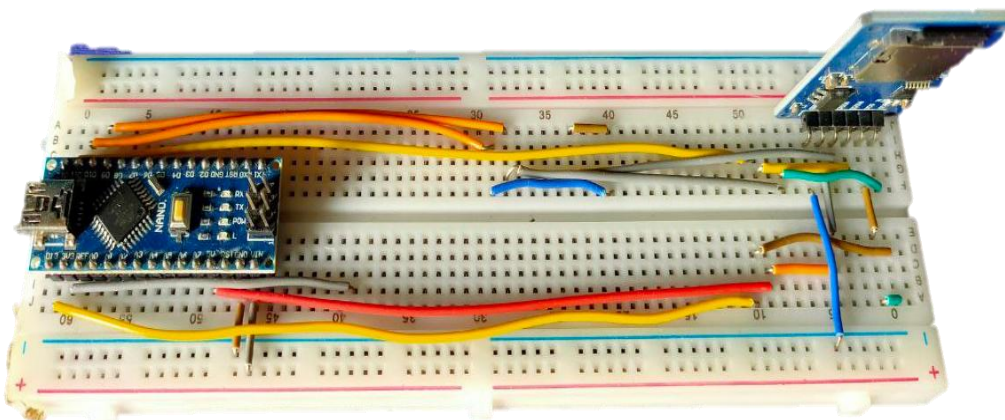


Figure 5.22: Micro SD card module setup on a breadboard.

Figure 5.22 shows the micro-SD card module setup on a breadboard using an Arduino. The Arduino code initializes the SD card module and opens a file to check the module. Once the file is open, data can be written to it. After writing the data on the card, the file is closed. Figure 5.23 shows the full circuit setup with the Teensy 4.0 microcontroller along with the MPU 6050 IMU and micro-SD card module. Teensy 4.0 is connected to the MPU 6050 via I2C communication, which allows the Teensy to read the sensor data from the IMU. Teensy can write data to the SD card using SPI communication to connect to the microSD card module. A mini 360 module is used for a regulated power supply to all components. The building consists of a 6-channel receiver, which allows for controlling the movement of the UAV by incorporating servos in control surfaces such as the rudder and elevator. These servos, along with a tilt mechanism servo, are connected to the Teensy microcontroller, which can be seen in Figure 5.23. For stable and efficient flight, these control surfaces enable precise and coordinated movement of the UAV. To determine the UAV's current orientation and movement, the controller continuously reads data from the orientation sensor. The Teensy then analyzes the required control inputs to keep the UAV stable. Actuators receive control inputs to ensure stability, and the microSD card stores relevant information for post-flight analysis and future optimization.

Figure 5.24 shows the PCB designed for this VTOL project to make a compact and efficient system. The design prioritizes smaller form factors by utilizing component placement and modularity. It uses the same Teensy 4.0 microcontroller unit that is used in the testing process

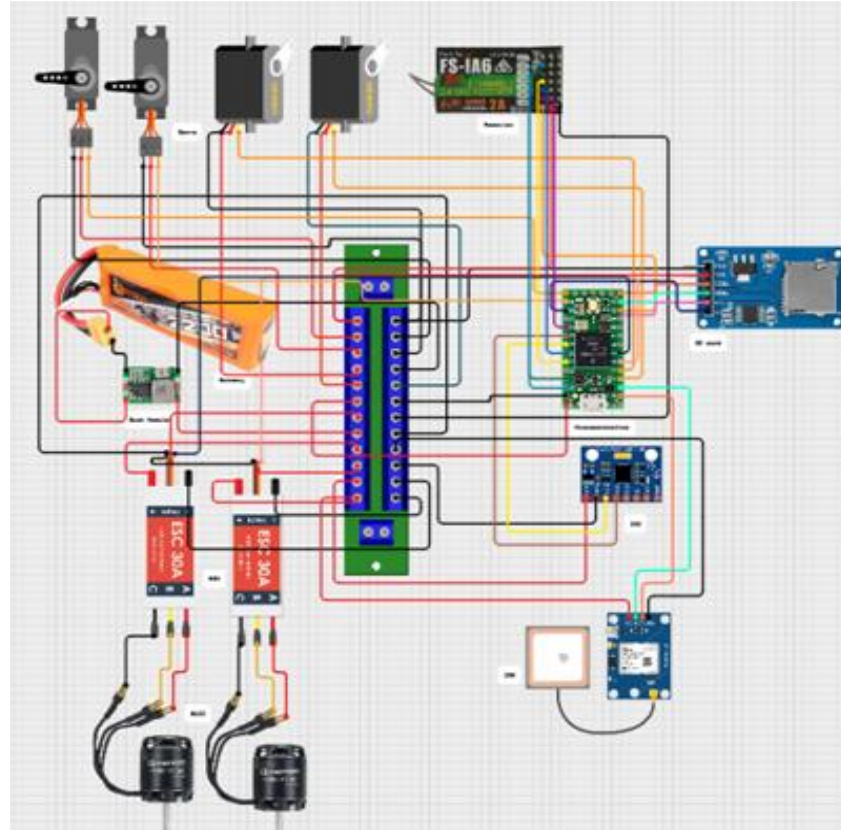
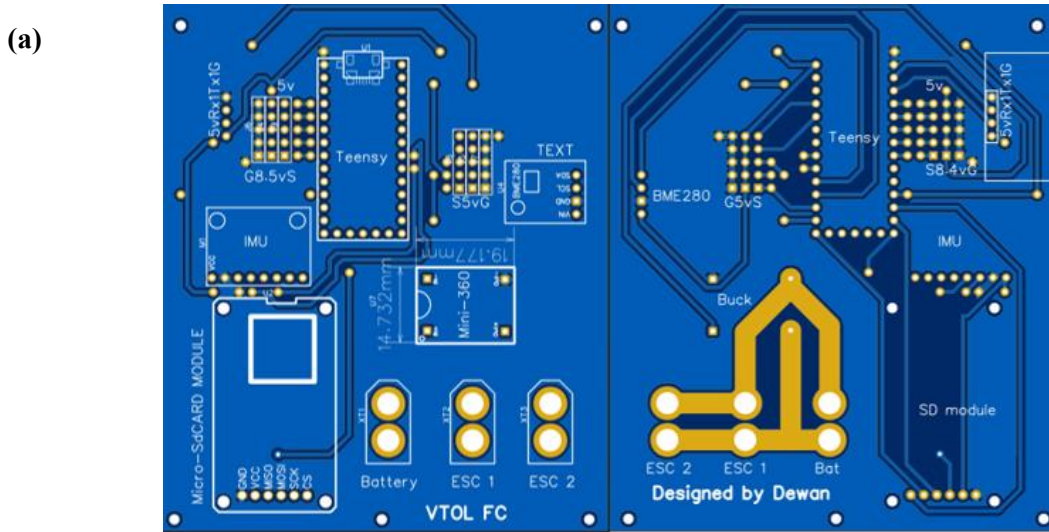


Figure 5.23: The Circuit Diagram designed for VTOL.



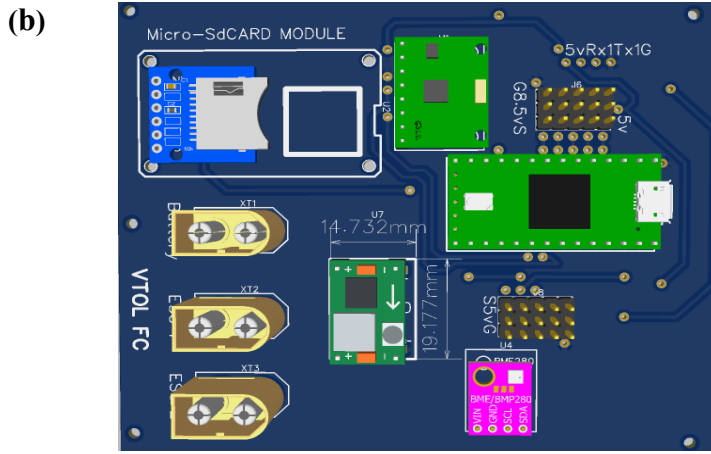


Figure 5.24: The PCB design for VTOL UAV, a) 2D View, b) 3D View.

throughout the development, and the same IMU, microSD card module, etc. Still, there is room left for future sensor integration for various testing purposes and data logging to store data. The PCB dimensions are 90mm×105mm (L×W). This PCB design contributes to a reliable and scalable VTOL system.

## 5.4 Control System Integration and Calibration

A strong VTOL UAV needs a lot of work to get its control system to work together and be accurate. It requires various sensors, actuators, and flight control algorithms to work seamlessly for stable flight performance. Moreover, the efficiency of the UAV depends on the calibration of the control system. Otherwise, the attitude stability and controllability of the UAV will be compromised. Figure 5.25 represents a closed-loop system that regulates the UAV's rotational speed. In this case, by comparing the desired rotation rate with the actual rate, then by calculating the difference (error), and then using a PID controller to adjust the motor power.

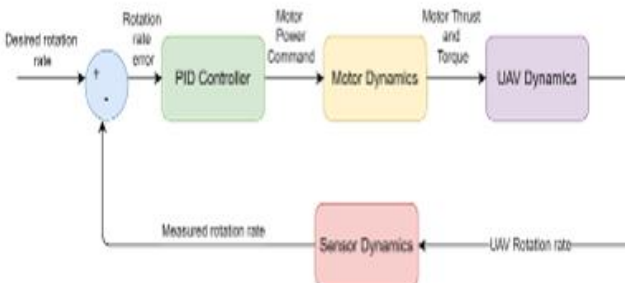


Figure 5.25: Detailed block diagram of a UAV rotation rate control system, illustrating the error between desired and measured rotation, the PID controller's role, motor and UAV dynamics, and the sensor feedback mechanism.

| Output                                                                                                                                                                                                                                                                                                                                                                                                                                               | Serial Monitor X                                                                                                                                                                                                                                                                                                                                                                                                                           |
|------------------------------------------------------------------------------------------------------------------------------------------------------------------------------------------------------------------------------------------------------------------------------------------------------------------------------------------------------------------------------------------------------------------------------------------------------|--------------------------------------------------------------------------------------------------------------------------------------------------------------------------------------------------------------------------------------------------------------------------------------------------------------------------------------------------------------------------------------------------------------------------------------------|
| Message (Enter to send message to 'Teensy 4.0' on                                                                                                                                                                                                                                                                                                                                                                                                    |                                                                                                                                                                                                                                                                                                                                                                                                                                            |
| GyroX:8.35, GyroY:-3.25, GyroZ:-1.47<br>GyroX:8.35, GyroY:-3.25, GyroZ:-1.47<br>GyroX:8.35, GyroY:-3.25, GyroZ:-1.46<br>GyroX:8.35, GyroY:-3.25, GyroZ:-1.46<br>GyroX:8.34, GyroY:-3.25, GyroZ:-1.46<br>GyroX:8.34, GyroY:-3.25, GyroZ:-1.46<br>GyroX:8.34, GyroY:-3.25, GyroZ:-1.46<br>GyroX:8.34, GyroY:-3.25, GyroZ:-1.45<br>GyroX:8.34, GyroY:-3.25, GyroZ:-1.45<br>GyroX:8.35, GyroY:-3.25, GyroZ:-1.45<br>GyroX:8.35, GyroY:-3.25, GyroZ:-1.45 | GyroX:0.00, GyroY:-0.00, GyroZ:0.00<br>GyroX:0.00, GyroY:0.00, GyroZ:0.00<br>GyroX:0.00, GyroY:-0.00, GyroZ:0.01<br>GyroX:0.00, GyroY:-0.00, GyroZ:0.01<br>GyroX:0.00, GyroY:-0.00, GyroZ:0.01<br>GyroX:-0.00, GyroY:-0.00, GyroZ:0.01<br>GyroX:-0.00, GyroY:-0.00, GyroZ:0.01<br>GyroX:-0.00, GyroY:0.00, GyroZ:0.01<br>GyroX:-0.00, GyroY:0.00, GyroZ:0.01<br>GyroX:-0.01, GyroY:0.01, GyroZ:0.01<br>GyroX:-0.01, GyroY:0.01, GyroZ:0.01 |

Figure 5.27: Gyroscope readings from the IMU, illustrating the raw data before calibration (left) and the improved stability and accuracy of the data after calibration (right).

Based on the data, the designed VTOL flight controller adjusts its position for stable operation. This graph and Figure 5.27 illustrate the calibrated IMU data with and without calibration in the Arduino IDE serial monitor. Figure 5.28 shows the dynamic behavior of the IMU sensor roll, pitch, and yaw values before and after calibration. The stationary line in the graph indicates that the IMU is quiescent, and the fluctuating line indicates that the IMU is experiencing movements. The rotation rates are measured in degrees per second by the IMU. In the precision control of the VTOL

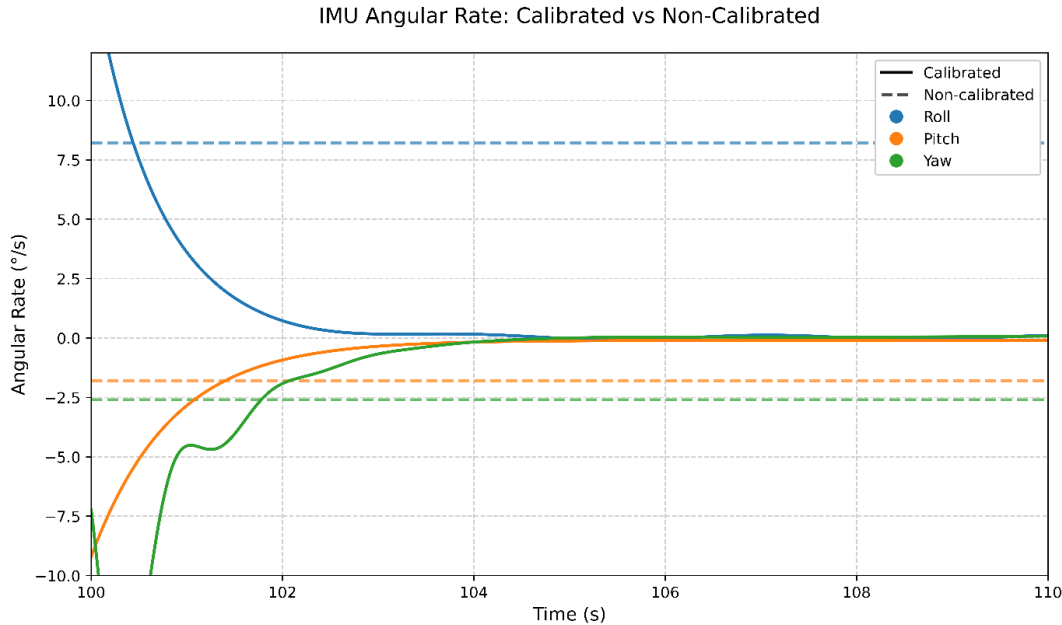


Figure 5.28: Time-series plot visualizing the IMU data, highlighting the fluctuation in rotational rates with calibration.

UAV, the raw data transmitted from the remote controller had to be known. It entailed intercepting and demodulating the data received by the UAV's receiver. The first step was normalizing the control inputs. The raw transmitter signals (see Fig. 5.29) were scaled between -1000 and 1000. Scaling provides the control inputs with a symmetrical and known range and simplifies the rest of the programming immensely. The middle stick position would thus ideally correspond with value 0 and full deflection, one way with the value -1000 and the other with the value +1000. However, the first tests revealed that the transmitter controllers' center, or middle positions, were not always putting out a value of 0. To rectify this, the trimming process was implemented. This involved making fine adjustments necessary to the transmitter configurations to trim the centers of the control sticks and potentiometer to put out a value as close to 0 as could be made. The trimming process was needed so the UAV control system could accurately record the middle positions of the control sticks and would not produce any undesirable movement or instability. To view these maps and, where necessary, trimmed values, the receiver was interfaced with a computer, and the Serial Monitor feature of the Arduino IDE was employed. The latter displayed the numerical value of all control channels live. The values shown on the Serial Monitor were the following:

- Channels 1 through 5 are the primary control inputs for flight control, i.e., aileron, elevator, throttle, and rudder, and redundant input from a potentiometer. The readings displayed by these channels mimicked the motion of the control sticks from the transmitter and the potentiometer. The trimming process ensured the channels displayed around 0 value whenever the control was in the middle, i.e., the middle calibration was precise.
- Channel 6 displayed a binary value corresponding to the switch status. It would either be a value of 0 or 1 for the 'off' and 'on' positions of the switch.

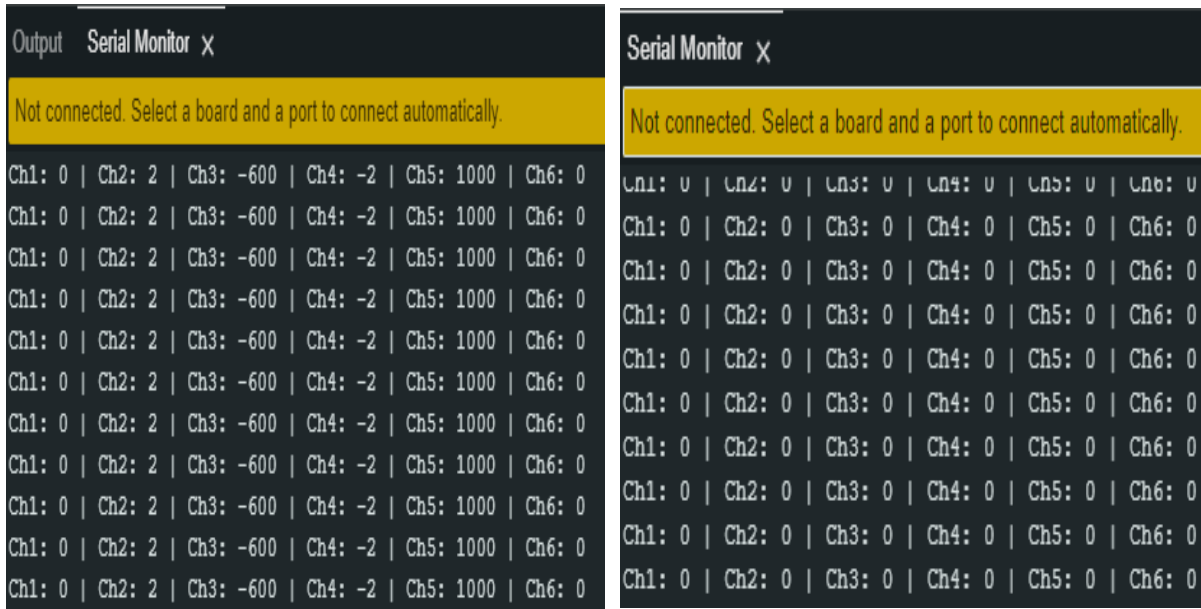


Figure 5.29: Visualization of Transmitter Calibration. The left image shows the initial Serial Monitor output, highlighting the need for trimming. The right image shows the corrected output after trimming, ensuring precise control inputs for the VTOL UAV.

Real-time visualization of the control data, especially after trimming, is essential for the debugging process and for tuning the control system of the UAV. By seeing the actual numerical values that result from every control input, we can design accurate and responsive control algorithms for the VTOL UAV.

# Chapter 6

## DEVELOPMENT

---

Developing a fixed-wing UAV with VTOL capabilities involves a series of methodical steps to ensure the design, testing, and production of reliable and efficient aircraft. Here is a description of each step in the development process:

- 1. Requirement Analysis:** The first step involved gathering and defining the requirements for the UAV. This includes understanding the specific needs and constraints of the intended application, such as payload capacity, range, flight duration, environmental conditions, and regulatory considerations. Potential users and regulatory bodies are consulted to ensure that all necessary criteria are considered.
- 2. Conceptual Design:** Based on the requirements, initial design concepts were created. This stage involves brainstorming different configurations and selecting a design that meets the requirements. The focus is on the overall layout, including the placement of wings, rotors, and control surfaces. Aerodynamic properties, weight distribution, and propulsion methods are key considerations. Sketches and basic models were developed to visualize and evaluate different concepts.
- 3. Detailed Design:** Once a concept was chosen, detailed design work began. This includes creating precise engineering drawings and specifications for each component. Computer-aided design (CAD) software is used to develop 3D models that include every part of the UAV, from the airframe to the electronic systems. Detailed simulations are performed to analyze the aerodynamics, structural integrity, and performance characteristics.
- 4. Construction:** With detailed designs in place, prototypes were built (see App. A1-4). This stage involves fabricating parts, assembling the prototype, and integrating the necessary electronics and control systems. Rapid prototyping techniques, such as 3D printing, were used to quickly produce parts for testing.
- 5. Electronics:** Once the aircraft has been constructed, the electronics are installed (see App. A5-6). That includes FS-i6X 10-channel receiver, TD-8320MG servo motor, AS2820 brushless DC motor, and battery.

**6. Testing and tuning:** End of construction, and all the electronics were installed; it is time to test the aircraft and tune it. This involves adjusting the control system parameters and testing the aircraft in flight to ensure that it is stable and flies well. But due to some constraints, comprehensive testing could not be done. One of the difficulties is time constraints. This is one reason for failing to fly and test the aircraft. But some initial tests were conducted to see how the system works. The system runs back and forth smoothly with the selected motors.

## 6.1 Weight of the Aircraft

The measured weight of the UAV with all the electronics components onboard is shown in Table 6.1

*Table 6.1: Weight of the aircraft*

| Name of the equipment   | Quantity | Weight     |
|-------------------------|----------|------------|
| Teensy                  | 1        | 10 grams   |
| Servo motor             | 3        | 100 grams  |
| Brushless motor         | 2        | 250 grams  |
| ESC                     | 2        | 75 grams   |
| MPU-6050 Gyroscope      | 1        | 5 grams    |
| LiPo battery (3300 mAh) | 1        | 270 grams  |
| Propeller               | 2        | 40 grams   |
| Wing weight             |          | 400 grams  |
| Tail weight             |          | 100 grams  |
| Fuselage weight         |          | 100 grams  |
| Others                  |          | 100gm      |
| Total weight            |          | 1450 grams |

## 6.2 Fabrication

Different manufacturing processes have been discussed below for fabricating the UAV.

| Methods | Advantages | Disadvantages |
|---------|------------|---------------|
|---------|------------|---------------|

|                                 |                                                                                                                                                      |                                                                                                                                                                                                          |
|---------------------------------|------------------------------------------------------------------------------------------------------------------------------------------------------|----------------------------------------------------------------------------------------------------------------------------------------------------------------------------------------------------------|
| <b>3D-printing</b>              | <ul style="list-style-type: none"> <li>➤ Low cost</li> <li>➤ Capable of making very complex parts</li> <li>➤ Parts can be quickly printed</li> </ul> | <ul style="list-style-type: none"> <li>➤ Relatively fragile</li> <li>➤ Parts size restricted to printer size</li> <li>➤ Parts are isotropic</li> </ul>                                                   |
| <b>Balsa/Plywood</b>            | <ul style="list-style-type: none"> <li>➤ Low cost</li> <li>➤ Parts can be made expediently</li> </ul>                                                | <ul style="list-style-type: none"> <li>➤ Requires complex digital modeling to design</li> </ul>                                                                                                          |
| <b>Carbon fiber composites</b>  | <ul style="list-style-type: none"> <li>➤ High stiffness-to-weight ratio</li> <li>➤ Lightweight</li> </ul>                                            | <ul style="list-style-type: none"> <li>➤ Expensive</li> <li>➤ Time-consuming layup process</li> <li>➤ Blocks certain frequencies of radio signals</li> </ul>                                             |
| <b>Fiberglass composites</b>    | <ul style="list-style-type: none"> <li>➤ Does not block radio frequencies</li> <li>➤ High strength-to-weight ratio</li> </ul>                        | <ul style="list-style-type: none"> <li>➤ Comparatively weaker than carbon fiber</li> <li>➤ Shrinks and distorts when wetted with epoxy resin</li> <li>➤ Soaks up more resin increasing weight</li> </ul> |
| <b>Foam-core structures</b>     | <ul style="list-style-type: none"> <li>➤ Can act as spacers to increase overall strength</li> <li>➤ Allows for quick prototyping</li> </ul>          | <ul style="list-style-type: none"> <li>➤ Requires sanding for a smooth surface</li> </ul>                                                                                                                |
| <b>Hollow molded structures</b> | <ul style="list-style-type: none"> <li>➤ Close resemblance to design profiles</li> <li>➤ Can be created using various materials</li> </ul>           | <ul style="list-style-type: none"> <li>➤ Time-consuming to fabricate the mold</li> </ul>                                                                                                                 |

3D printing's capacity for swift production and low overhead costs made it the ideal choice for this project. So, the process of fabricating the UAV is discussed below,

#### Materials:

- **3D Printing:**
  - Filament:
    - **Strong ABS filament** (considering durability)
    - **Lightweight PLA filament** (considering weight reduction)
  - **Software:** SolidWorks (for design)
  - **Software:** Cura (for slicing)
  - **Hardware:** FDM printer (e.g., Ender 3 S1 Pro)
- **Wings:** Carbon fiber tubes (size based on design)

- **Assembly:** Epoxy resin, carbon fiber cloth
- **Finishing:** Sandpaper (various grits)
- **Electronics:** Motors, flight controller (as per design)

#### Steps:

##### 1. Design & Print the Body:

- Used SolidWorks to design the UAV body, considering internal structures for strength and weight optimization.
- Exported to the 3D model in a slicer-compatible format (e.g., STL).
- Used Cura to slice the 3D model for printing. Configuration settings like infill density, layer height, and printing temperature are based on the chosen filament (PLA) and desired balance between strength and weight.
- 3D printed body parts using our Ender 3 S1 Pro printer.

##### 2. Prepare the Carbon Fiber Wings: (optional)

- Cut the carbon fiber tubes to the desired wingspan.
- Sanded the tube ends for better epoxy adhesion.
- Wrapped the tubes with carbon fiber cloth and secured with epoxy for extra reinforcement.

##### 3. Sanding and Finishing:

- Once the epoxy was cured, sand down any rough edges or imperfections on the 3D-printed parts and wing joints.
- Used progressively finer sandpaper grits to achieve a smooth finish.

##### 4. Integrate Electronic Components:

- Mounted the motors, flight controller, and other electronics in designated locations within the 3D-printed body.
- Secured the components with appropriate fasteners and ensured proper wiring connections.

##### 5. Testing and Calibration:

- Performed pre-flight checks on all electronic components and control systems.
- Conduct initial test flights in a safe and controlled environment to calibrate sensors and ensure proper flight characteristics.

By following these steps and adapting them to the specific design, the VTOL UAV can be successfully built with a 3D-printed body and strong carbon fiber wings.

# Chapter 7

## SUSTAINABILITY

---

### 7.1 Social Impact Assessment

The development of VTOL UAV holds considerable promise for influencing the local community in both a social and economic manner. The project has the potential to enhance various aspects of the local community's social life while also fulfilling several Sustainable Development Goals (SDGs) aimed at improving the overall welfare of society [44].

#### 7.1.1 Social Benefits of the Project

This project has the potential to influence the long-term betterment of the social aspect of the people of the region. Some of these benefits are-

- **Job Creation:** The development and operation of VTOLs create job opportunities mainly in the fields of engineering, manufacturing, and drone piloting.
- **Public Safety:** The design motivation was that the UAV can be used in various public applications, mainly in search and rescue, disaster response, and surveillance. This improves community safety and well-being.
- **Economic Development:** The UAV can contribute to economic development by manufacturing or by enabling efficient data collection for various sectors, including agriculture, forestry, and infrastructure, while being affordable.

#### 7.1.2 Critical Analysis of Sustainable Development Goals (SDGs)

The project is closely aligned with multiple Sustainable Development Goals (SDGs), making it a significant contributor to sustainability efforts. The SDGs that are being addressed are-

1. **Affordable and Clean Energy (SDG 7):** By minimizing energy consumption due to electric propulsion, VTOLs can reduce greenhouse gas emissions and cleaner environment. By promoting sustainable and efficient energy use while reducing reliance on fossil fuels, the project achieves that goal.
2. **Industry, Innovation and Infrastructure (SDG 9):** VTOL technology represents a significant innovation in the modern aviation industry, pushing the boundaries of transportation and logistics. The advanced VTOL development can foster innovation and create new industries.

3. **Sustainable cities and communities** (SDG 11): VTOLs can play a critical role in reducing traffic congestion and improving urban mobility by enabling efficient urban mobility for transportation of goods.
4. **Climate Action** (SDG 13): An efficient VTOL can reduce a significant amount of carbon emissions compared to conventional quadcopters, as it utilizes a wing. So, VTOLs can help to mitigate climate change and contribute to a more sustainable future.
5. **Partnership for the Goals** (SDG 17): Successful development of VTOL technology requires collaboration between different stakeholders, including government agencies, industry partners, and research institutions. By fostering partnerships, the development and adaptation of sustainable VTOL solutions can accelerate and achieve a broader sustainable development goal.



Figure 7.1: A Holistic Approach to Sustainable Design (Courtesy of SOLIDWORKS [45]).

## 7.2 Environmental Impact Assessment

An Environmental Impact Assessment is an essential component in the planning of any project to evaluate its implications at local, regional, and global levels. The environmental impacts and benefits of VTOL UAVs can be classified as follows Fig. 7.2:

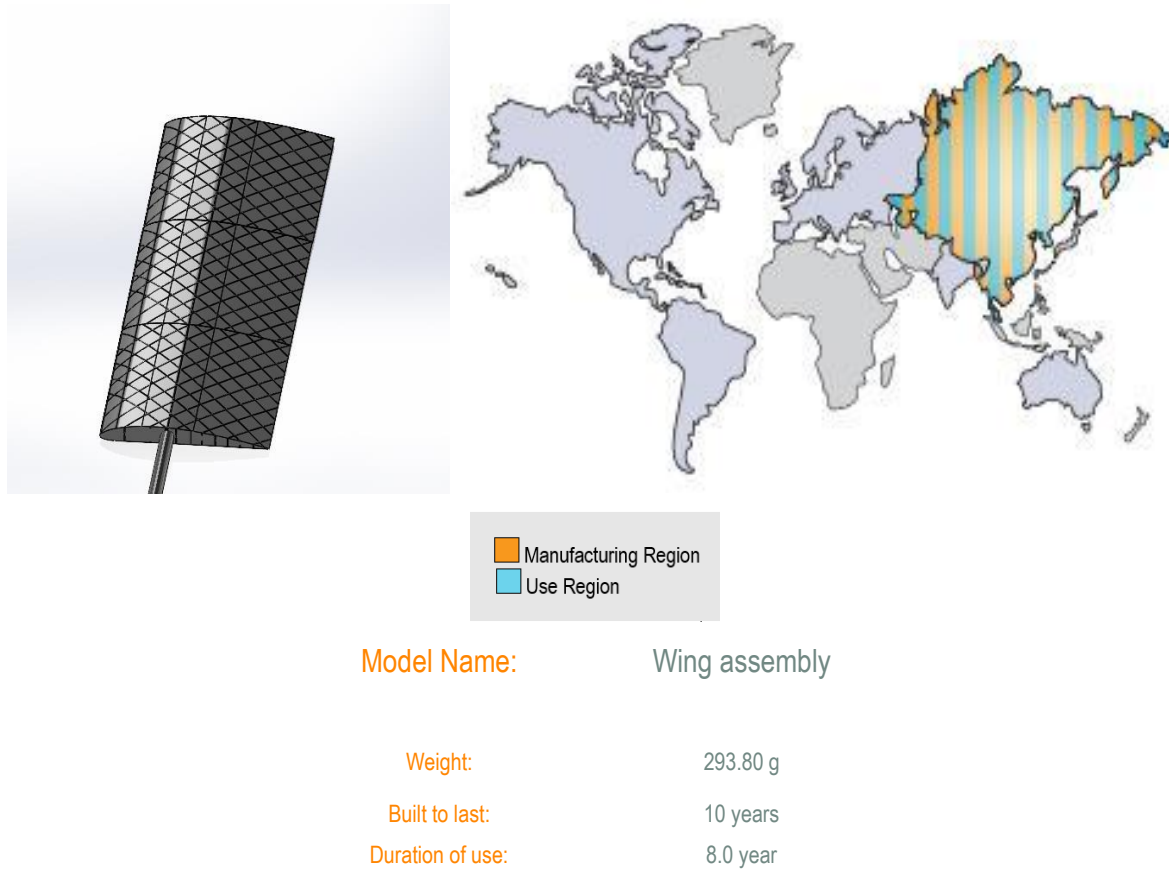


Figure 7.2: Key Environmental Impact parameters of the wing assembly's LCA. (Courtesy to SOLIDWORKS [45])

### Component Environmental Impact

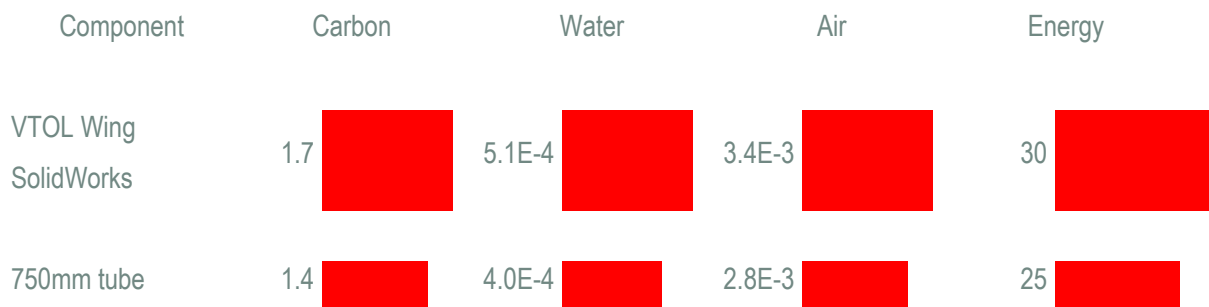


Figure 7.3: Components contributing most to the four areas of environmental impact [45].

Figure 7.3 shows the environmental impact of one side of the VTOL wing and the tube made of carbon fiber. The analysis focuses on four key areas for environmental impact assessment: carbon emission, water consumption, air pollution, and energy usage. The data reveals that the impact of the wing on the environment is higher across all categories. This is likely due to the wing's larger

size and complexity, which results in higher energy consumption and carbon emissions in manufacturing. The wing contributes 1.7 kg CO<sub>2</sub> to carbon emissions, 5.1E-4 m<sup>3</sup> to water consumption, 3.4E-3 kg SO<sub>2</sub> emission into air pollution, and 30 MJ energy usage. In contrast, the data for tube manufacturing consumes less energy and releases less carbon for a simple design.

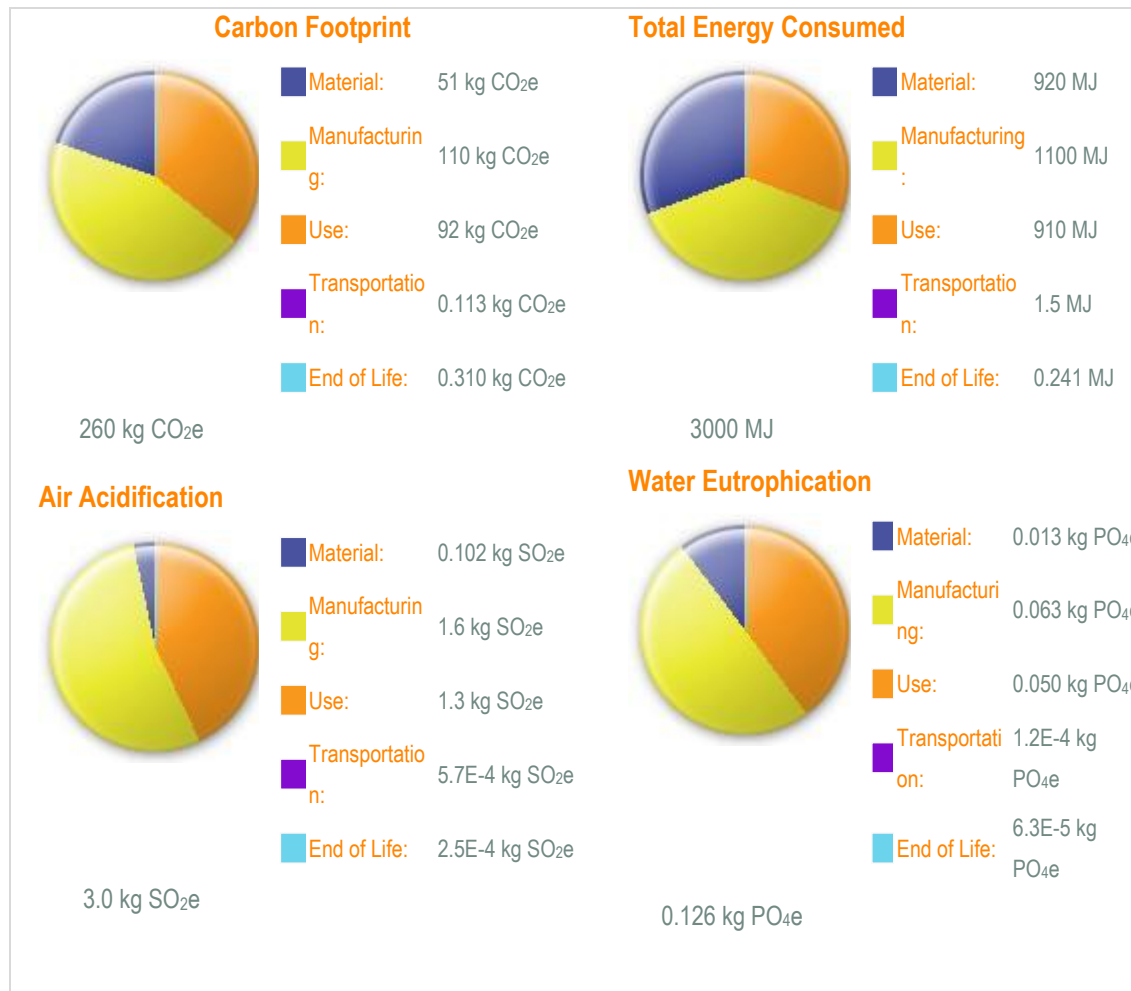


Figure 7.4: Environmental Impact (calculated using CML impact assessment methodology [45]).

Figure 7.4 represents the environmental impact of the product's life cycle. The analysis focuses on four key areas: carbon footprint, total energy consumed, air acidification, and water eutrophication. The data reveals that the major impact of the carbon footprint and energy consumption comes from the manufacturing stage. This is due to the energy required to transform raw materials into final products. The next major contributor is the use phase, where the usage of the product consumes energy. In the case of air acidification and water eutrophication, a similar pattern can be observed where manufacturing is the major contributor, followed by the use phase. So, manufacturing is the key area to focus on for the reduction of environmental impacts for a sustainable design.

# Chapter 8

## RESULTS & DISCUSSION

### 8.1 Experimental Data for Validation

Utilizing experimental data from 'A Catalog of Low Reynolds Number Airfoil Data for Wind Turbine Application' by Miley, S. J. (1982), the NACA 4412 airfoil was validated [46]. The Department of Aerospace Engineering at Texas A&M University, located in College Station, Texas 77843, created this extensive catalog. The experimental validation involves selecting the coefficient of lift and drag for a Reynolds number of 330,000. The provided data represent the lift and drag coefficients of the NACA 4412 airfoil at various angles of attack under the specified Reynolds number.

- Tunnel: NACA LTT / Date: 1945 / Test 2-D / Turbulence: 0.03% / Surface: Smooth Table

**Table 8.1:** Values of Lift and Drag Coefficient for different angles of attack

| Angle of Attack, $\alpha$<br>(°) | Coefficient of<br>Lift, $C_L$ | Coefficient of Drag, $C_d$ |
|----------------------------------|-------------------------------|----------------------------|
| -6                               | -0.19                         | 0.0193                     |
| -5                               | -0.11                         | 0.0166                     |
| -4                               | -0.03                         | 0.0149                     |
| -3                               | 0.07                          | 0.014                      |
| -2                               | 0.17                          | 0.0136                     |
| -1                               | 0.27                          | 0.0131                     |
| 0                                | 0.37                          | 0.0126                     |
| 1                                | 0.47                          | 0.0122                     |
| 2                                | 0.56                          | 0.0116                     |
| 3                                | 0.65                          | 0.012                      |
| 4                                | 0.74                          | 0.0123                     |
| 5                                | 0.82                          | 0.0128                     |
| 6                                | 0.9                           | 0.0141                     |
| 7                                | 0.98                          | 0.0157                     |
| 8                                | 1.05                          | 0.0182                     |
| 9                                | 1.11                          | 0.0219                     |
| 10                               | 1.13                          | 0.0288                     |
| 11                               | 1.22                          | 0.0373                     |
| 12                               | 1.26                          | 0.0543                     |
| 13                               | 1.29                          | -                          |
| 14                               | 1.29                          | -                          |
| 15                               | 1.29                          | -                          |
| 16                               | 1.18                          | -                          |
| 17                               | 1.12                          | -                          |
| 18                               | 1.08                          | -                          |
| 19                               | 1.05                          | -                          |
| 20                               | 1                             | -                          |

## 8.2 Validation Analysis with Miley Airfoil Data

As the main methods for evaluating accuracy and dependability, verification and validation are crucial parts of every computer simulation process. In order to assess if the computational model is in line with physical reality, the validation procedure entails a thorough analysis of the model's analyses and a comparison of the results with experimental findings. Examining the model's analyses in comparison to experimental data is part of this procedure. The validation phase in this work was completed by comparing data sets from XFLR5 that represented the lift and drag coefficients of the NACA 4412 airfoil with those from Miley's report. The accuracy and dependability of the computer simulation under study are confirmed by this thorough analysis and comparison with actual data.

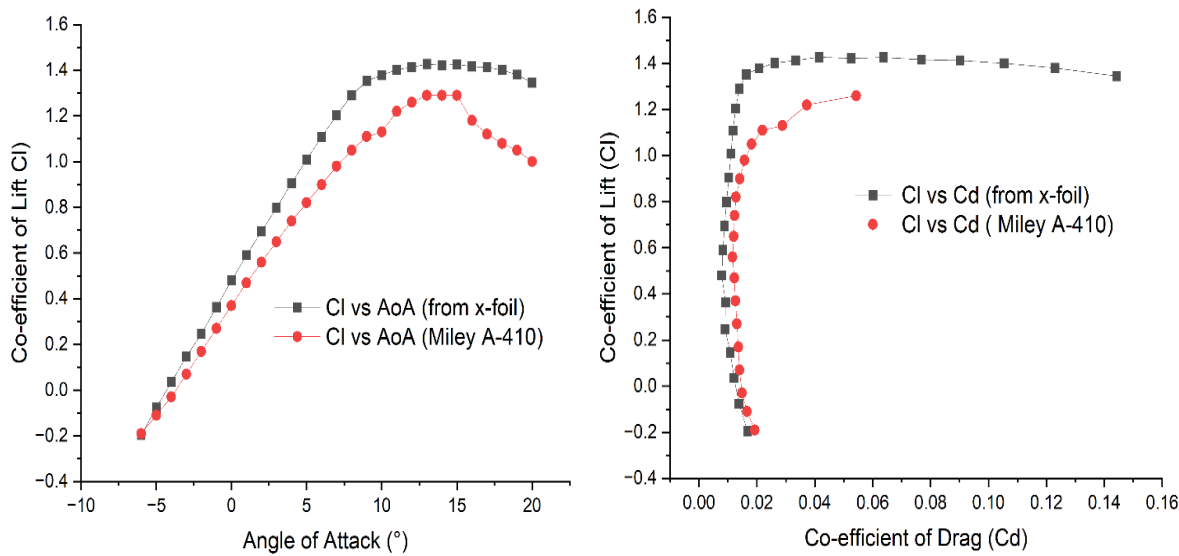


**Figure 8.1:** Comparison between (a) Left one:  $C_l$  vs  $AoA$ ; & (b) Right one:  $C_l$  vs  $C_d$ ; from XFLR5 and Miley's report

The results on Fig. 8.1 show that the lift coefficient of NACA 4412 derived using XFLR5 is comparable to the data published by Miley in 1982. At lower angles of attack, the data shows strong correspondence, whereas at higher angles, there are minor differences. It makes sense to conclude that the lift coefficient values from XFLR5 and Miley's study are validated. Also there appears to be a substantial resemblance between the drag coefficients of NACA 4412 reported by Miley in 1982 and those derived using XFLR5. Over a spectrum of low and high angles of attack, the values show a strong correlation. It is plausible to conclude that the drag coefficient values from XFLR5 match those in Miley's study.

### 8.3 Results

Table 8.2 represents the calculated value of lift (L), drag (D) from speed 5m/s to 30m/s. The graph in Fig. 8.2 depicts the angle of attack ( $\alpha$ ), according to the lift coefficient ( $C_l$ ) for different velocities.

**Table-8.2: Numerical Calculated Value of Lift(L) & Drag(D) at Different Velocities**

| Velocity, v<br>(m/s) | Reynolds<br>Number,<br>Re | Critical<br>Angle of<br>Attack, $\alpha$<br>( $^{\circ}$ ) | Lift<br>Coefficient,<br>$C_l$ | Lift<br>(N) | Drag<br>Coefficient,<br>$C_d$ | Drag<br>(N) |
|----------------------|---------------------------|------------------------------------------------------------|-------------------------------|-------------|-------------------------------|-------------|
| 5                    | 28063                     | 10                                                         | 0.670266                      | 1.47        | 0.125195                      | 0.27        |
| 10                   | 56127                     | 10                                                         | 1.367024                      | 12.05       | 0.037991                      | 0.33        |
| 15                   | 84190                     | 10                                                         | 1.372048                      | 27.2        | 0.028732                      | 0.57        |
| 20                   | 112254                    | 10                                                         | 1.372784                      | 48.4        | 0.025486                      | 0.90        |
| 25                   | 140317                    | 10                                                         | 1.372662                      | 75.6        | 0.023893                      | 1.31        |
| 30                   | 168381                    | 10                                                         | 1.371956                      | 108.9       | 0.022975                      | 1.82        |

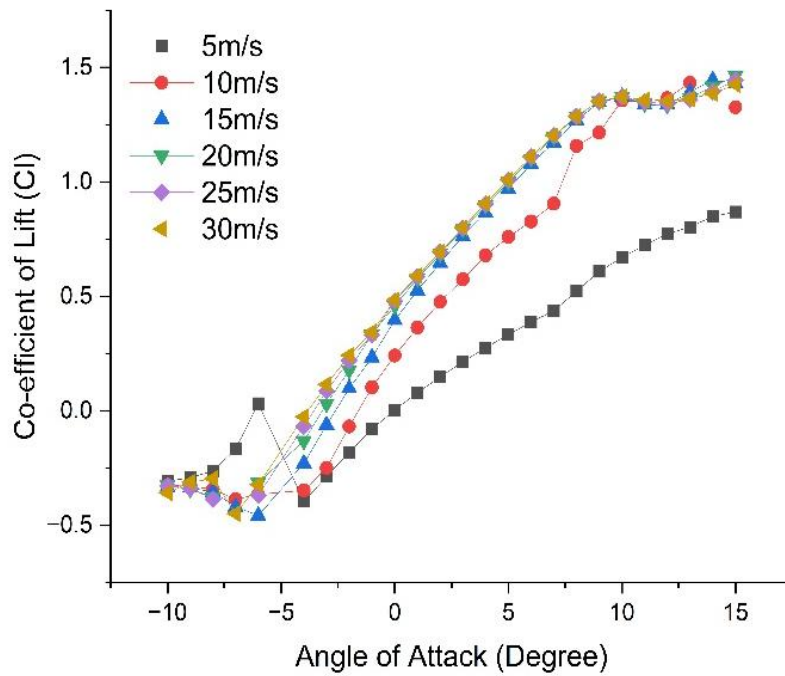


**Figure 8.2: Lift Coefficient vs Angle of Attack at Different Velocities**

The graph in Fig. 8.3 shows the lift coefficient ( $C_l$ ) vs drag coefficient ( $C_d$ ) for different velocities.

The lift and drag at various velocities are shown in Table 8.2. Plots of these velocities are then shown in Figures 8.2 and 8.3. Firstly, Reynolds numbers were found during the computation process. The matching lift and drag coefficients were found via XFLR5 (2D) simulation using those Reynolds numbers. The lift and drag were computed using those coefficients.

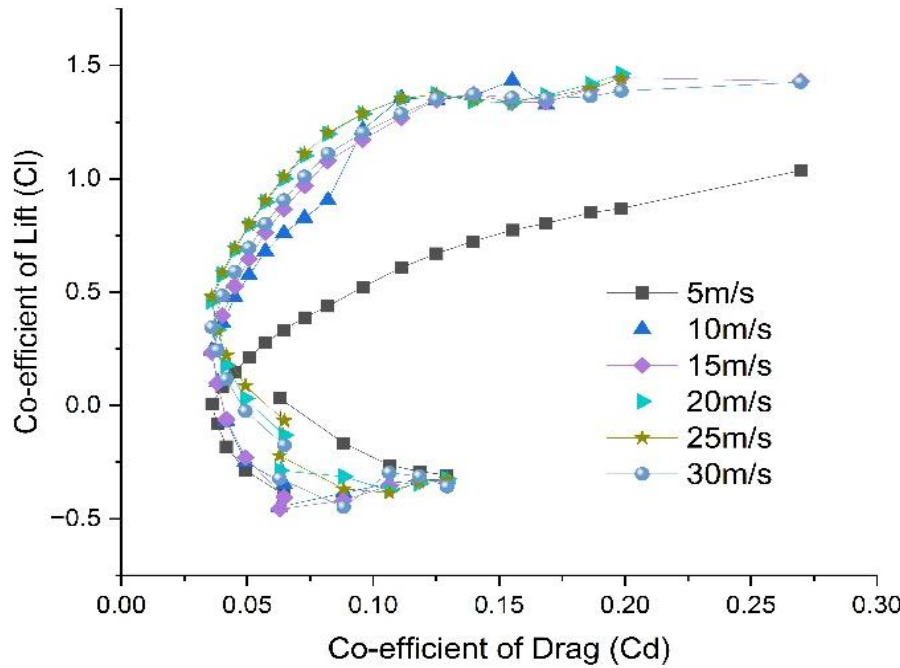


**Figure 8.3:** Lift Coefficient vs Drag Coefficient at Different Velocities

## 8.4 Validation Against Open-Source Airfoil Data

The simulated Lift coefficient vs Angle of Attack graph is validated below. Data for the validation is compared to airfoilstool.com and simulation data from XFLR5. In Fig. 8.4, the square black box reflects the experimental results, and the red circle represents the simulations. There is a discrepancy between the experimental and simulation plots. While computations only account for optimal conditions, experimental situations examine a wide range of factors. 9,10 & 11-degree angles of attack are where the two graphs almost match. But after that, they start to differ from one another.

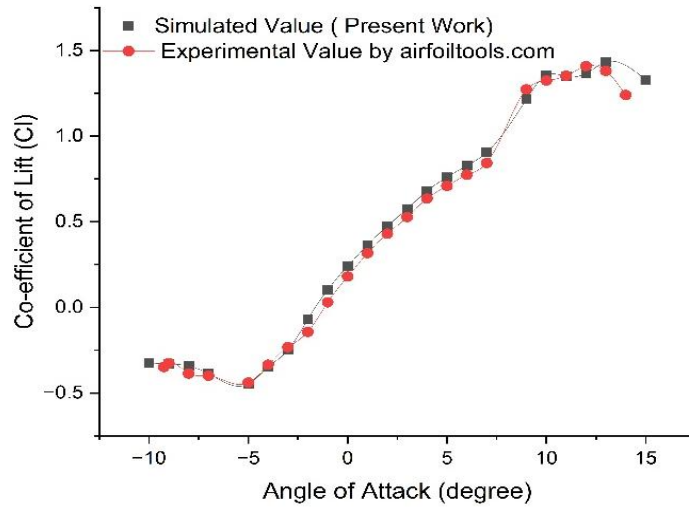


**Figure 8.4:** Comparison Between Computational Data & Experimental Data of Lift Coefficient vs Angle of Attack

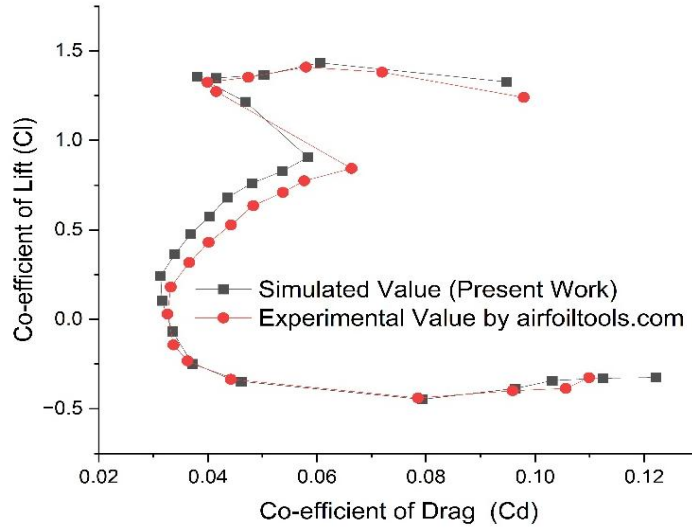


**Figure 8.5:** Comparison Between Computational Data & Experimental Data of Lift Coefficient vs Drag Coefficient.

Figure 8.5 illustrates that the experimental and computational data for NACA 4412 are presented in the  $C_L$  vs  $C_D$  graph. The simulated value derived from XFLR5 is denoted by the red circle, whereas the experimental value is indicated by the black box. There are evident discrepancies between the two curves. The simulation considered only the optimal situation. In contrast, the experimental approach considers the surroundings. Nonetheless, the two plots are virtually indistinguishable. It intersected in specific areas. Consequently, the computational graph and the experimental graph corroborate each other.

In validating the computational data against experimental data for 10m/s velocity at different

angles of attack [35]. Typically, AoA influences both the drag & lift forces experienced by an airfoil NACA-4412. The following *Table 8.3* illustrates the raw data that is extracted from the validated graphs (*Fig. 8.4 & 8.5*).

**Table 8.3: Comparison of Computational & Experimental Data for Different AoA at 10m/s velocity**

| <b>Computational data</b>  |                                            |                                            | <b>Experimental Data [35]</b> |                                            |                                            |
|----------------------------|--------------------------------------------|--------------------------------------------|-------------------------------|--------------------------------------------|--------------------------------------------|
| <b>Angle of Attack (°)</b> | <b>Coefficient of Lift (C<sub>L</sub>)</b> | <b>Coefficient of Drag (C<sub>D</sub>)</b> | <b>Angle of Attack (°)</b>    | <b>Coefficient of Lift (C<sub>L</sub>)</b> | <b>Coefficient of Drag (C<sub>D</sub>)</b> |
| -9                         | -0.32909                                   | 0.11243                                    | -9                            | -0.3263                                    | 0.10991                                    |
| -8                         | -0.34225                                   | 0.10317                                    | -8                            | -0.3862                                    | 0.10566                                    |
| -7                         | -0.38621                                   | 0.0964                                     | -7                            | -0.3988                                    | 0.0959                                     |
| -5                         | -0.44722                                   | 0.07935                                    | -5                            | -0.4394                                    | 0.0785                                     |
| -4                         | -0.34724                                   | 0.04612                                    | -4                            | -0.3354                                    | 0.04419                                    |
| -3                         | -0.24884                                   | 0.03717                                    | -3                            | -0.2321                                    | 0.03627                                    |
| -2                         | -0.06817                                   | 0.0335                                     | -2                            | -0.1432                                    | 0.03369                                    |
| -1                         | 0.10331                                    | 0.03156                                    | -1                            | 0.0297                                     | 0.03258                                    |
| 0                          | 0.24157                                    | 0.03135                                    | 0                             | 0.1804                                     | 0.03318                                    |
| 1                          | 0.36393                                    | 0.03395                                    | 1                             | 0.3166                                     | 0.03657                                    |
| 2                          | 0.47617                                    | 0.03682                                    | 2                             | 0.4299                                     | 0.04014                                    |
| 3                          | 0.57519                                    | 0.04025                                    | 3                             | 0.5279                                     | 0.04426                                    |
| 4                          | 0.67944                                    | 0.04356                                    | 4                             | 0.635                                      | 0.04832                                    |
| 5                          | 0.7605                                     | 0.04809                                    | 5                             | 0.7094                                     | 0.05375                                    |
| 6                          | 0.8277                                     | 0.05366                                    | 6                             | 0.7737                                     | 0.05768                                    |
| 7                          | 0.90533                                    | 0.05834                                    | 7                             | 0.843                                      | 0.06634                                    |
| 9                          | 1.21622                                    | 0.04685                                    | 9                             | 1.2725                                     | 0.04155                                    |
| 10                         | 1.35702                                    | 0.03799                                    | 10                            | 1.3248                                     | 0.03991                                    |
| 11                         | 1.34795                                    | 0.04153                                    | 11                            | 1.3527                                     | 0.04742                                    |
| 12                         | 1.36656                                    | 0.05027                                    | 12                            | 1.4092                                     | 0.05796                                    |
| 13                         | 1.43303                                    | 0.06053                                    | 13                            | 1.381                                      | 0.07194                                    |
| 15                         | 1.32701                                    | 0.09478                                    | 14                            | 1.2403                                     | 0.09792                                    |

## 8.5 CFD Analysis (3D)

Using the X-Foil (XFLR5) simulation application, different profiles for lift and drag, as well as data for viscous drag, streamlines, and vortices through simulation, were generated [47].

### 8.5.1 Lift

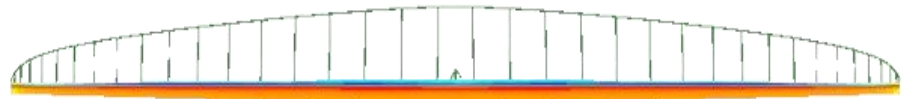


**Figure 8.6a:** Lift Profile at  $10^{\circ}$  Angle of Attack

As the airfoil maintains an elliptical lift distribution, as depicted in the picture, which illustrates the lift distribution generated by the wing in an elliptical configuration. Elliptical lift is ideal because it minimizes induced drag. It's often used as a target distribution in aerodynamic design. A significantly greater lift is generated at the wing's root chord compared to its tip chord. The lift generated follows a reverse exponential profile, decreasing from the tip chord to the root chord.



**Figure 8.6 b:** Lift Profile at  $-9^{\circ}$  Angle of Attack

### 8.5.2 Drag

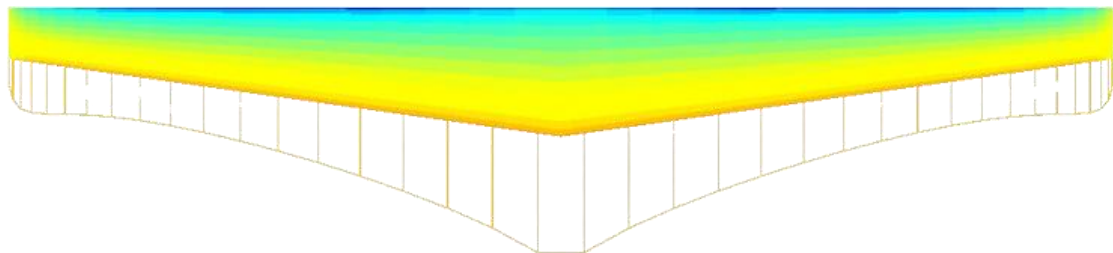


**Figure 8.7a:** Induced Drag (top view)

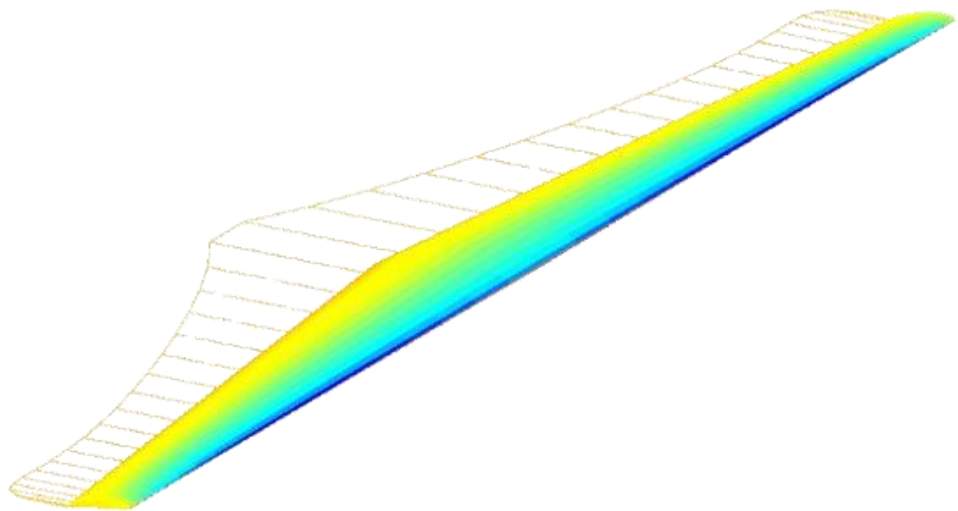


**Figure 8.7b:** Induced Drag Profile (isometric view)

The drag stays the same at both positive and negative points of attack. The drag profile shows how drag is spread out over the wing. The drag is strongest at the chord root, but it is weaker at the tip chord. The drag profile of the whole wing looks like a triangle.

### 8.5.3 Downwash

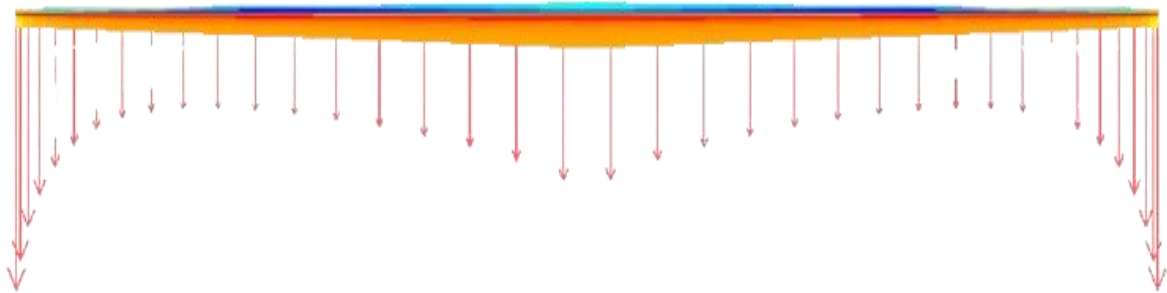


**Figure 8.8a:** Downwash Profile at  $10^{\circ}$  Angle of Attack

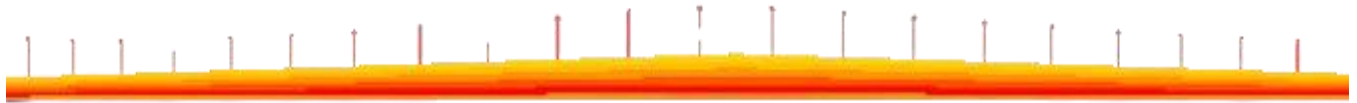


**Figure 8.8b:** Downwash Profile at  $-9^{\circ}$  Angle of Attack

The downwash profile illustrates the downward airflow occurring over the entire wing. The magnitude (length) of the arrows shows how much air is being deflected downward at each point along the span. The most significant downwash effect occurs at the wingtip chord, whereas the least significant occurs at the root chord. This profile illustrates a curved form owing to the symmetrical characteristics of the airfoil.

#### 8.5.4 Streamline

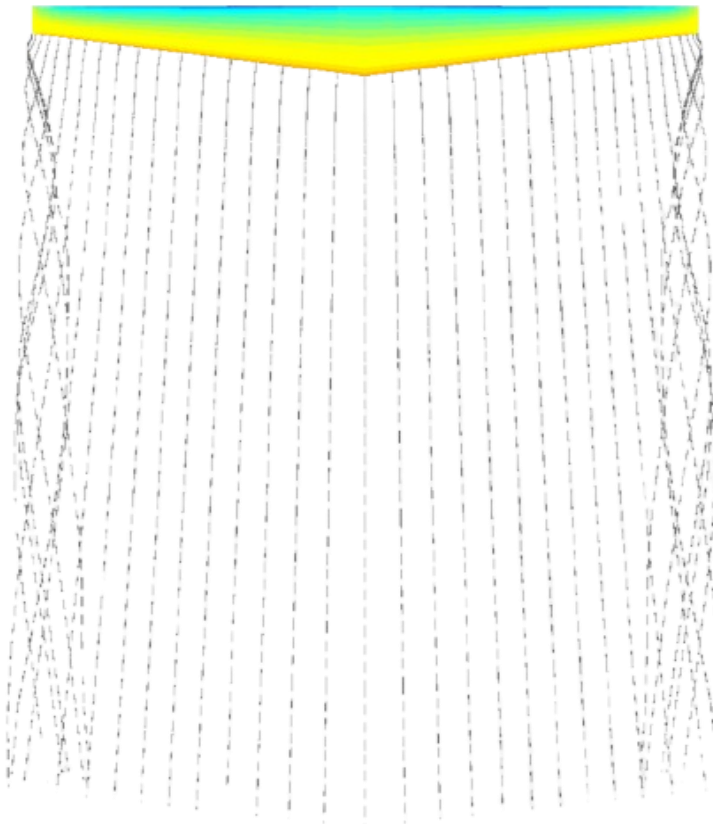


**Figure 8.9a:** Streamline Profile (top view)

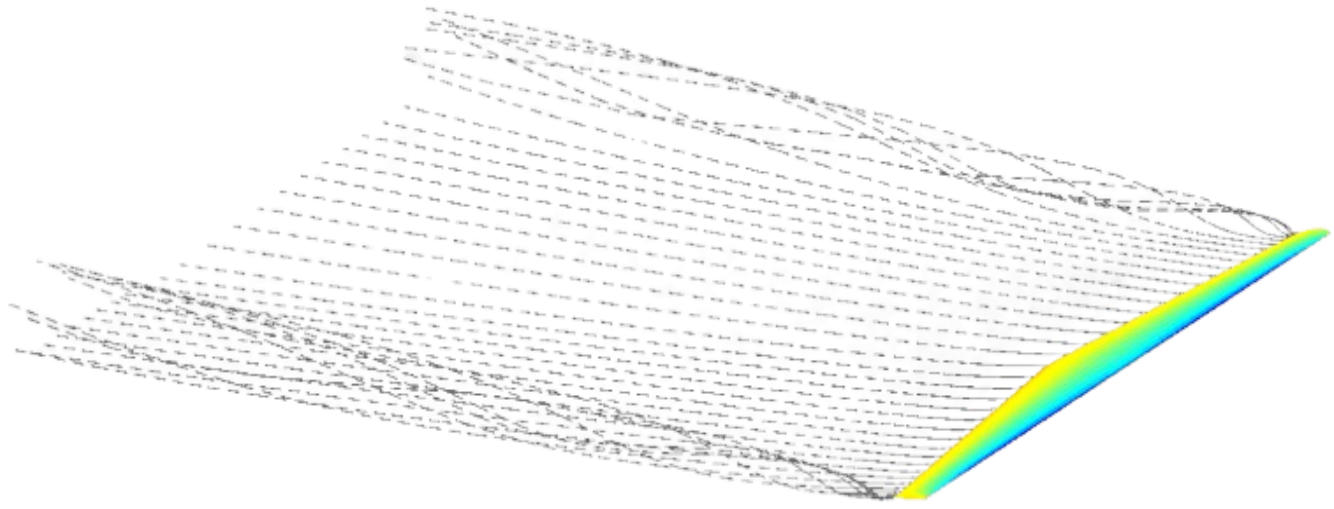


**Figure 8.9 b:** Streamline Profile at  $10^{\circ}$  Angle of Attack

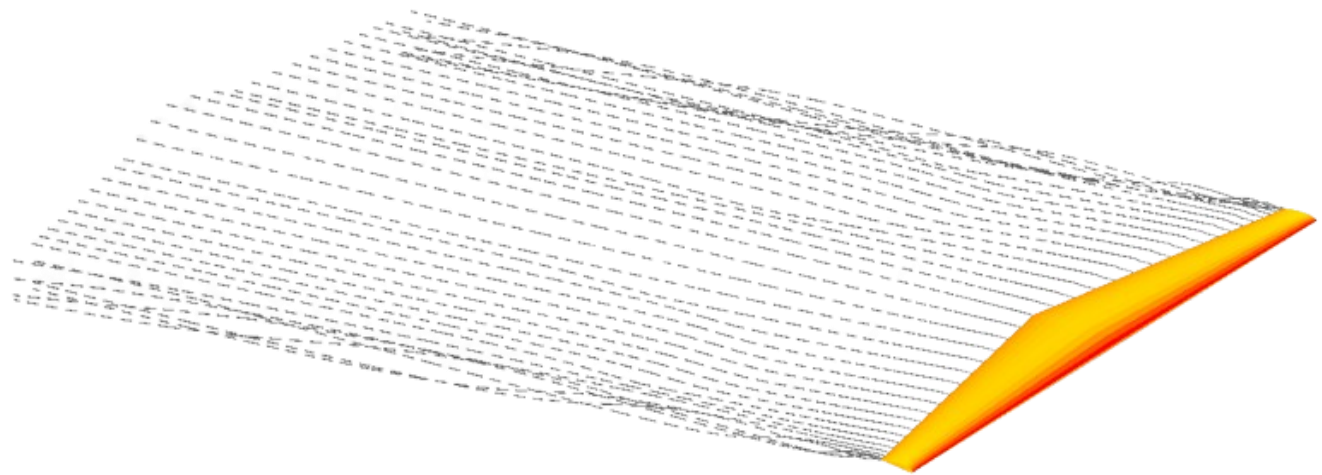


**Figure 8.9c:** Streamline Profile at  $-9^{\circ}$  Angle of Attack

The streamlined profile shows the airflow's passage across the wing. Interestingly, a vortex is visible at the chord of the wing tip, which is consistent with the known presence of vortices at this position. The only area of the wing where there is a streamline disturbance is the tip chord; the airflow remains smooth across the wing.

Overall simulation is illustrated in the two figures below. It is a complete illustration of all the

simulations combined.

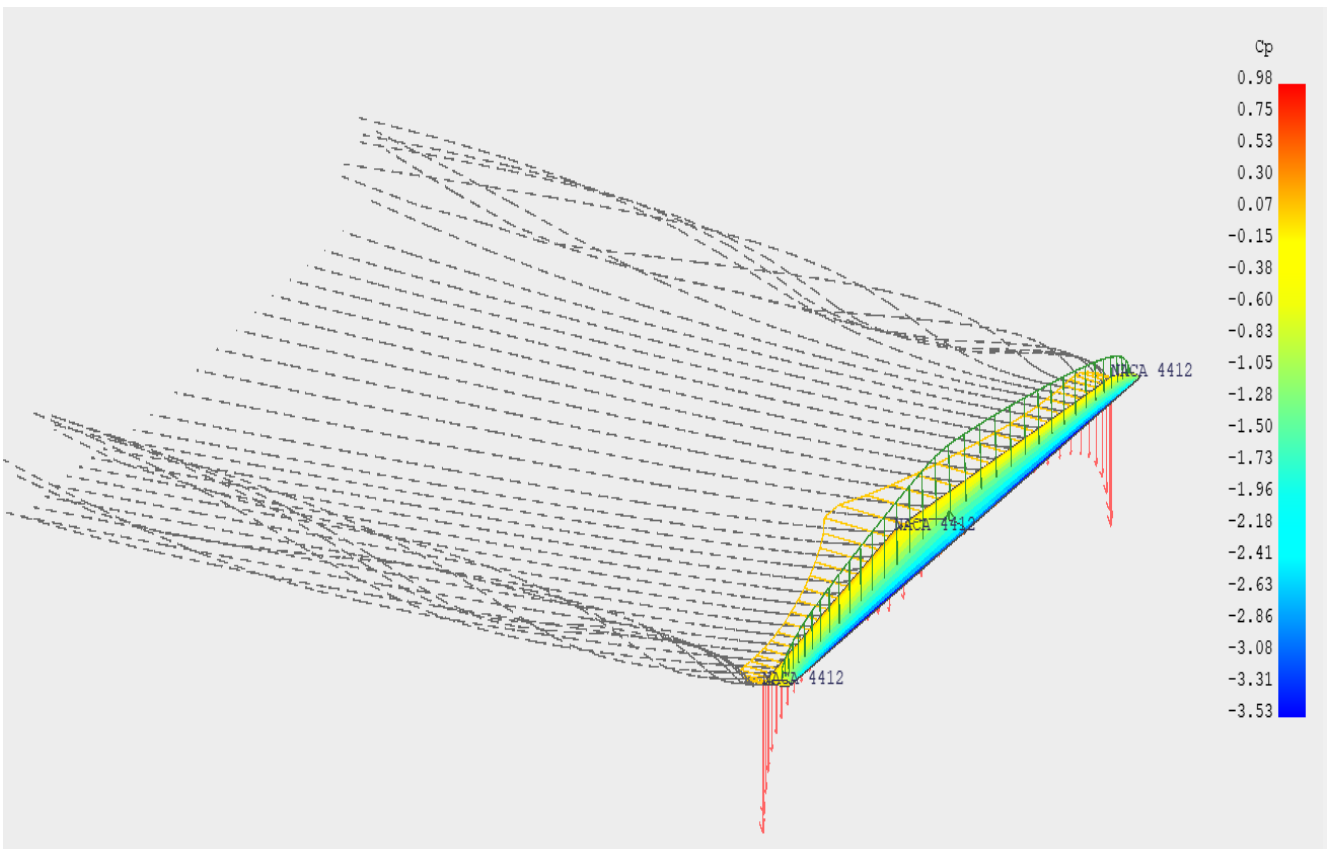


**Figure 8.10a:** Combined Isometric View of Lift, Drag, Downwash, Streamline At  $10^0$  AOA

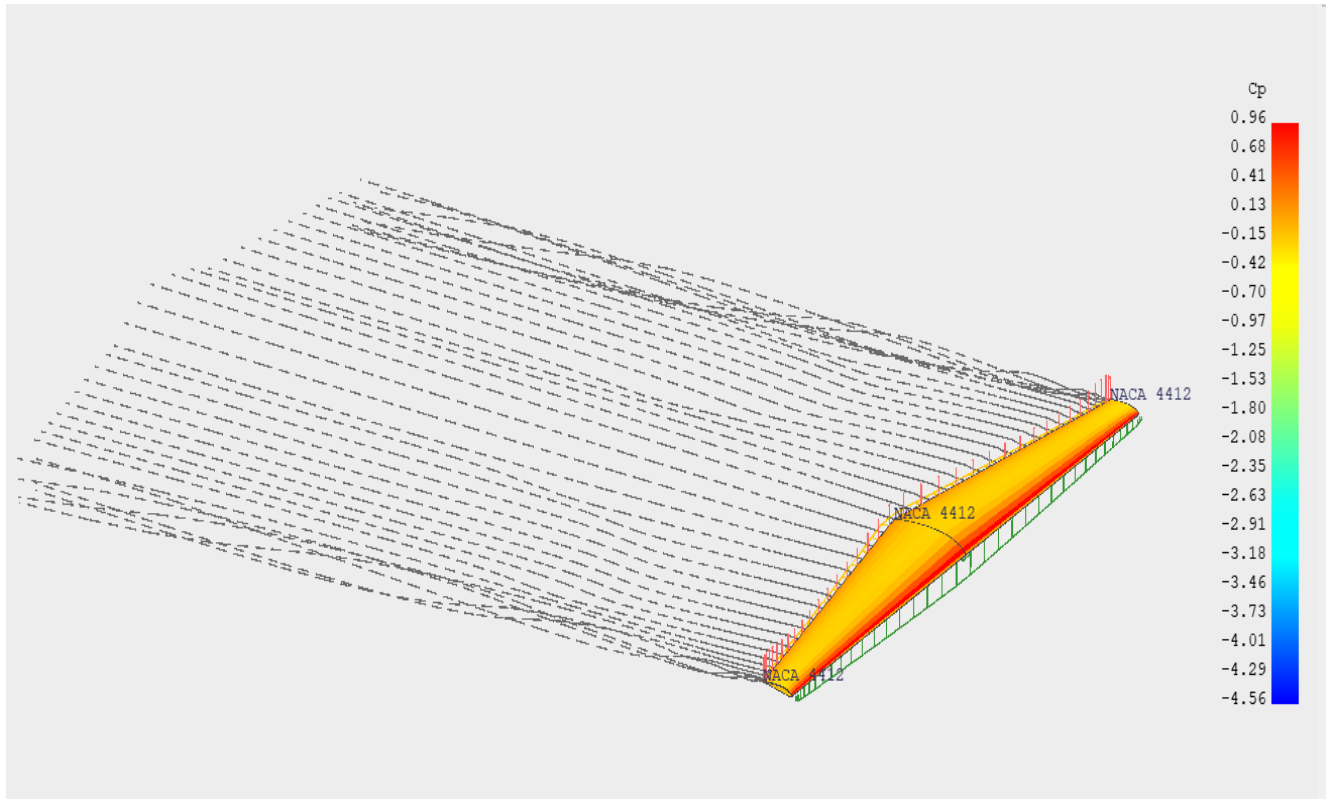


**Figure 8.10 b:** Combine Isometric View of Lift, Drag, Downwash, Streamline At  $-9^{\circ}$  AOA

The simulation was done in XFLR5, where lift and line theory were followed. From the simulation, the following data (see Table 8.4) were generated, which are shown in the figure.

**Table 8.4:** Extracted Values from Simulation

| Angle of Attack, ( $\alpha$ ) | Lift coefficient, ( $C_L$ ) | Induced Drag Coefficient, ( $C_{D_i}$ ) | Pitching Moment ( $C_M$ ) | Total Drag coefficient, ( $C_D$ ) | Center of Pressure ( $X_{CP}$ ) |
|-------------------------------|-----------------------------|-----------------------------------------|---------------------------|-----------------------------------|---------------------------------|
| -4                            | -0.000523                   | 0.000003                                | -0.078154                 | 0.000003                          | -16.1952                        |
| -2                            | 0.156347                    | 0.000775                                | -0.117344                 | 0.000775                          | 0.0802                          |
| -1                            | 0.234713                    | 0.001736                                | -0.136964                 | 0.001736                          | 0.0621                          |
| 1                             | 0.391085                    | 0.004801                                | -0.176131                 | 0.004801                          | 0.0475                          |
| 2                             | 0.469005                    | 0.006898                                | -0.195631                 | 0.006898                          | 0.0439                          |
| 4                             | 0.624093                    | 0.012197                                | -0.234345                 | 0.012197                          | 0.0393                          |
| 5                             | 0.701177                    | 0.015385                                | -0.253513                 | 0.015385                          | 0.0377                          |
| 6                             | 0.777896                    | 0.018922                                | -0.272522                 | 0.018922                          | 0.0364                          |
| 8                             | 0.930079                    | 0.027003                                | -0.309975                 | 0.027003                          | 0.0345                          |
| 10                            | 1.080315                    | 0.036351                                | -0.346522                 | 0.036351                          | 0.0329                          |

|    |          |          |           |          |        |
|----|----------|----------|-----------|----------|--------|
| 11 | 1.154605 | 0.041469 | -0.364399 | 0.041469 | 0.0323 |
| 12 | 1.228291 | 0.046863 | -0.381984 | 0.046863 | 0.0317 |

### 8.5.5 Propeller Thrust Force

#### 8.5.5.a Boundary Conditions for CFD Analysis

**Table 8.5: Parameter Setting for the CFD Analysis**

| Parameters                   | Values                  |
|------------------------------|-------------------------|
| Inlet Velocity               | 10 m/s                  |
| Rotational Speed             | 6000 rpm                |
| Rho ( $\rho$ )               | 1.225 kg/m <sup>3</sup> |
| Angle of attack ( $\alpha$ ) | 5°                      |
| Nu ( $v$ )                   | 1.89×10 <sup>-5</sup>   |

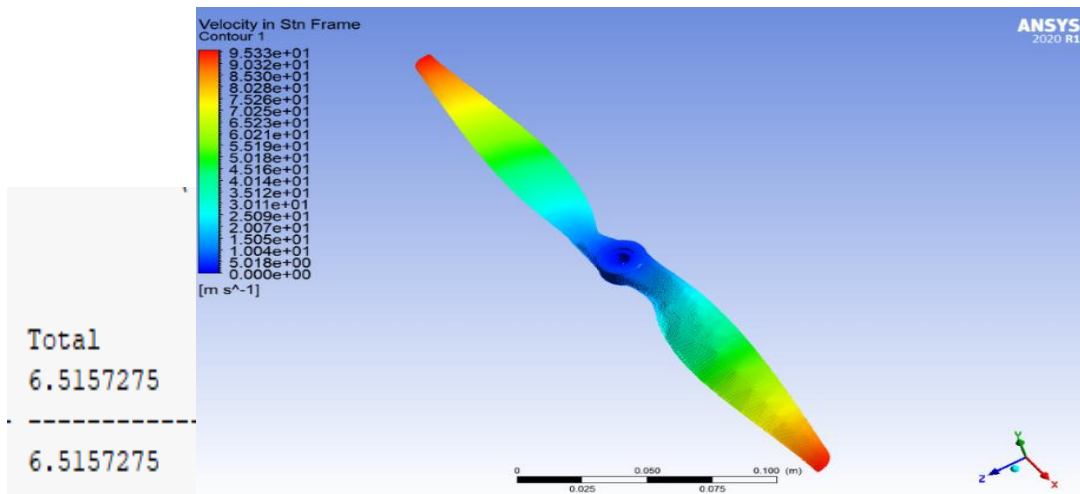


**Figure 8.11a:** Propeller Velocity Contour with Thrust Force

From Table 8.2, the numerical value of lift for 10m/s was found to be 12.54 N & after CFD at Ansys, the lift/thrust force generated from a propeller was found to be 6.51 N. So, the numerically calculated value & simulated values are almost the same.

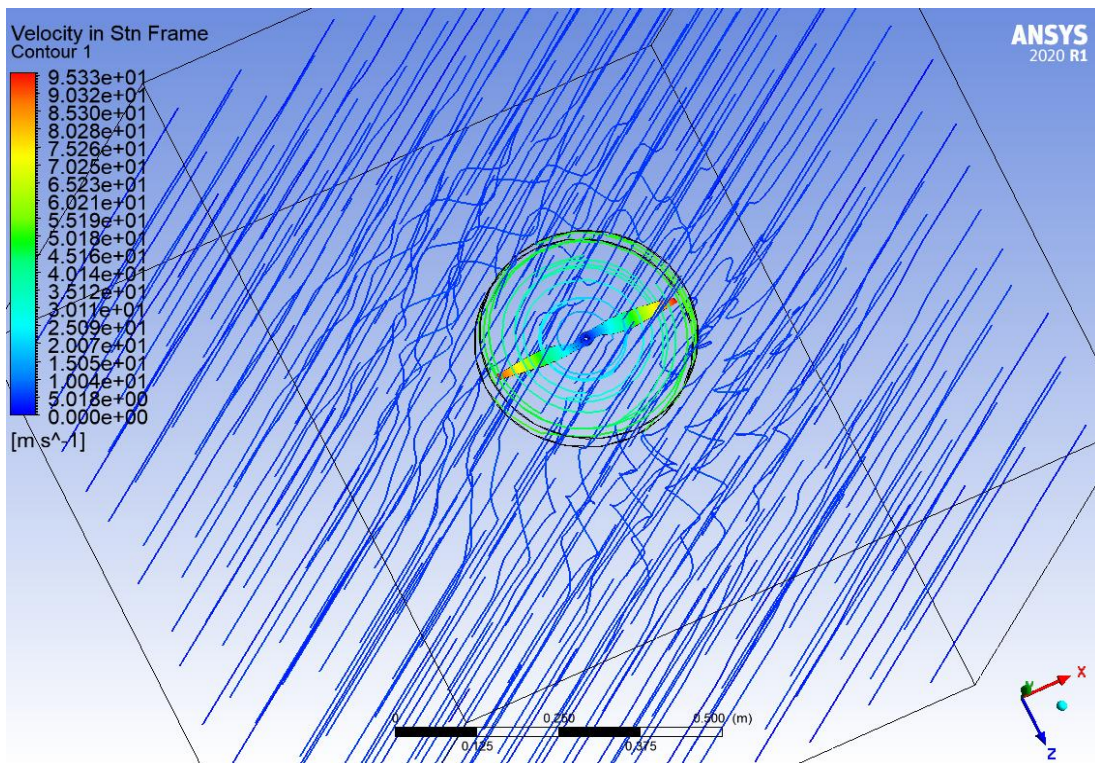


**Figure 8.11b:** Propeller Velocity Streamline

## 8.6 Optimization

### 8.6.1 Redesign of Wing

From *Table 8.2*, the numerical value of lift for 10m/s at 10° angle of attack was found to be 8.31 N & Drag 0.28 N after simulation. Now, developing a new wing design for optimization by taking the chord root & chord tip same (0.2m). A new wing design had been developed from which the value of lift and drag had been calculated using ANSYS Workbench [48]. The simulated value of the redesigned wing is given in Fig. 8.12. The meshing technique for CFD analysis is completed by establishing a mesh size of 150 mm. To ensure the precision of the simulation outcomes, additional mesh refinements were implemented, comprising a body sizing of 42 mm, face size of 10 mm, and an inflation with 12 layers with a maximum thickness of 16 mm. The SST k-omega turbulence model was utilized in this study. The simulation was conducted using a pressure-velocity coupled scheme with a second-order solution approach at an inlet velocity of 10 m/s and an angle of attack of 10°. ANSYS calculated a lift of 13.3595 N and a drag of 1.1303 N.

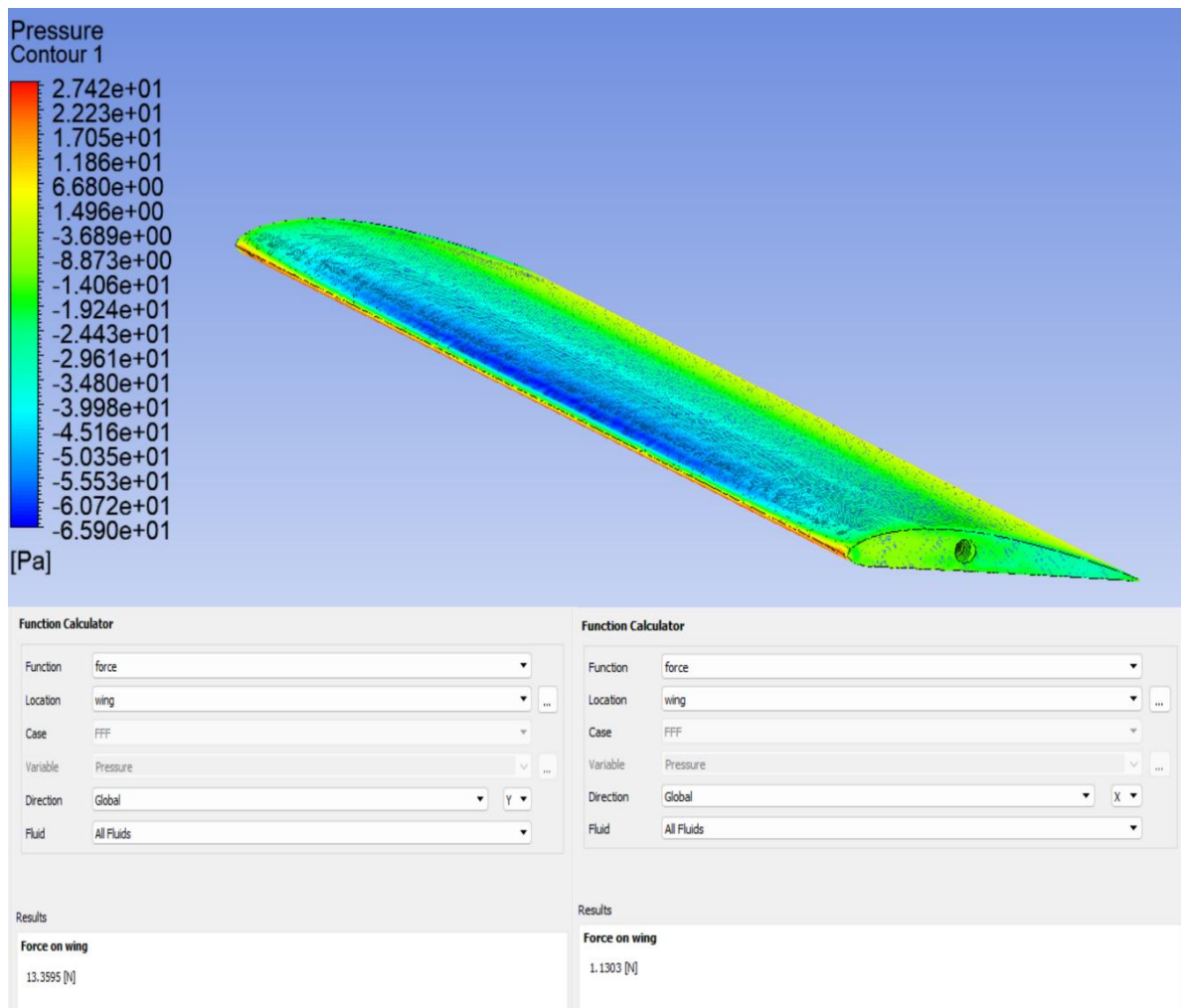


**Figure 8.12: Optimized Wing Lift & Drag**

### 8.6.2 Verification of the Optimized Wing

The simulation for verification was done in XFLR5. For a  $10^\circ$  angle of attack at 10m/s velocity. This wing had been developed for improved optimization and to redesign the model. These simulation results were compared with the ANSYS Workbench (Fig. 8.12, Fig. 8.13), where lift values were estimated at 13.359N. By using different application tools (XFLR5) with the same boundary conditions, by taking the chord tip, and chord root as a constant (0.2m) throughout the wing lift found 15.61N, which is higher than the previous wing (Fig.10). The ultimate reasons are for this deviation of lift occurs due to ANSYS using a 3D CFD approach with detailed meshing, by capturing complex aerodynamic effects, while XFLR5 is based on simpler panel methods, which approximate flow and may underpredict lift, especially in 3D cases. So, the optimized design of the wing is justified.

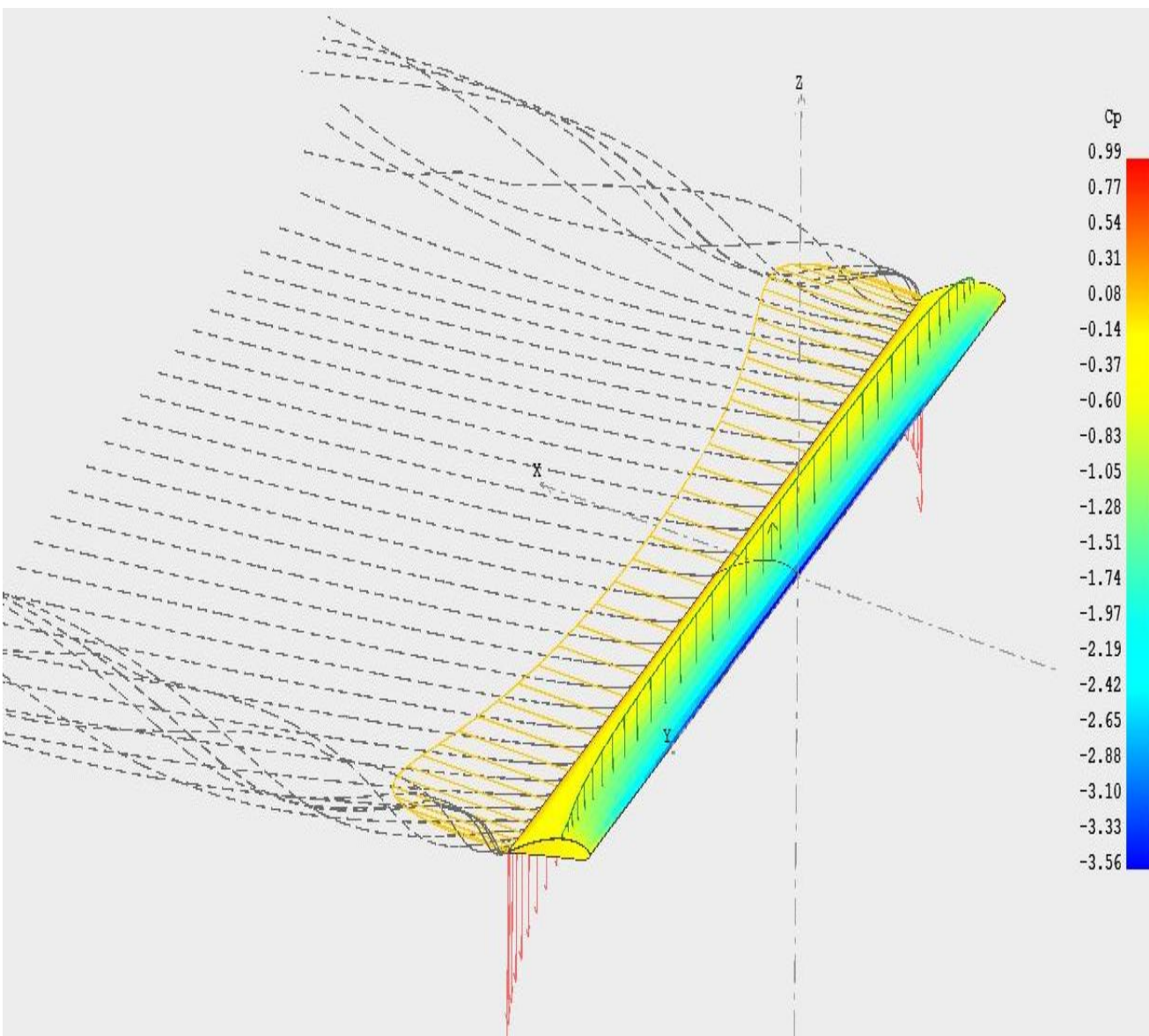


**Figure 8.13:** Combined Isometric View of Optimized Wing Lift, Drag, Downwash, Streamline At  $10^0$  AOA

# Chapter 9

# CONCLUSIONS

---

## 9.1 Conclusion

In the present world, fixed-wing unmanned aerial vehicles are becoming substantially more adaptable. These types of unmanned aerial vehicles (UAVs) are becoming increasingly popular in the field of research since they are relatively inexpensive, have the potential to fly for longer periods of time, and have a greater capacity for carrying cargo. The objective of this project was to design and build a low-cost unmanned aerial vehicle (UAV) with a fixed wing. This was accomplished through the utilization of parametric analysis and real-time manufacturing. Following the completion of the analytical computations, the conceptual model was constructed with the assistance of SOLIDWORKS. The NACA 4412 airfoil was shown to be superior to other wing shapes in terms of lift and drag. In addition, it is easy to print in three dimensions, which is another advantage of this particular airfoil. In order to achieve a higher level of design optimization, iterative adjustments were implemented based on simulation data received from computational fluid dynamics (CFD) software such as ANSYS and XFLR5. After simulation with a chord tip of 0.05721m & chord root of 0.1428m wing generating 9.6N lift at 10m/s with an angle of attack of 10°, which is lower than the theoretical one. So that by taking the chord tip & root as it is (0.2m), an optimized rectangular wing had been developed which produced almost 30% higher lift than the previous one. Although the CFD simulation was conducted at a velocity of 10 m/s, it provides substantial insights into airflow dynamics and lift patterns. As velocity increases under actual flying conditions, the resultant lift will increase, enabling the aircraft to ascend with the specified payload. Thus, the performance of the wing, which has a chord of 0.2m, was taken into consideration, and the fact that it is compatible with the tilt-rotor mechanism was another factor that drove its selection. For calculating the optimal parameters, which comprised the wingspan, lift, and necessary propulsion, the simulated data was utilized. Although initially selected T-Motor AS2820 880 kV capable of delivering 2 kg of thrust per unit resulted in a structurally destructive high-output thrust in 3D-printed PLA+ wing mounts. As a solution, two EMAX 980 kV outrunner motors were used later on, which deliver a thrust of 1 kg each. While it decreased peak thrust, it was sufficient for a total UAV mass of 1.5 kg and was used for lowering structural strain as well as expenses. This real-world adjustment only serves to illustrate how a compromise between

theoretical performance, material limitations, and expenses is essential in UAV design. The most significant findings have established a foundation that will lay the groundwork for the future development of unmanned aerial vehicles (UAVs). The research is being conducted with the primary purpose of achieving a reduction in weight across the board while optimizing the control system for low-noise, efficient UAVs. Continuous research into novel composite materials and construction methods will contribute to the advancement of unmanned aerial vehicle technology. This will be accomplished by advancing the development of technology.

## 9.2 Future Recommendations

Due to certain manufacturing difficulties encountered during the early stages of development, the vertical takeoff and landing (VTOL) unmanned aerial vehicle (UAV) couldn't undergo full-scale flight testing to assess its structural performance and aerodynamic efficiency. That was done to determine whether or not the UAV was of sufficient quality. Consequently, future endeavors will focus on improving the design through the utilization of advanced Computational Fluid Dynamics (CFD) simulations. This will be done to improve the design. The utilization of sophisticated high-resolution CFD investigations that apply advanced turbulence models and transient simulations will be utilized to acquire a comprehensive understanding of the dynamics of airflow over the NACA 4412 airfoil. This comprehension will be acquired through the course of several different tilt degrees and phases of transitional flying. As a result, the identification of aerodynamic parameters that are of critical significance, such as flow separation and lift-to-drag performance during vertical and horizontal transitions, will be simplified. The design of vertical takeoff and landing using tilt-rotor technology involves a lot of complicated mechanics and controls. This statement includes the synchronization of motor tilt angles, torque equilibrium, structural stress during transition phases, and real-time flight stability. This statement will also have more information in it. Future projects will address these challenges by employing dynamic system modeling and hardware-in-the-loop (HIL) testing to ensure dependable performance and seamless transitions between vertical takeoff and forward flight. This technology will be utilized to ensure that these concerns are resolved. Enhanced manufacturing techniques, in conjunction with the investigation of innovative composite materials, will be applied to lessen the weight of the structure while simultaneously increasing its capacity for structural strength and reliability. These goals will be accomplished by reducing the weight of the structure. Ultimately, this unmanned aerial vehicle (UAV) platform could develop into a fully functional, economically viable vertical

takeoff and landing (VTOL) system that is optimized for payload efficiency and endurance. Improving the modeling process, developing more sophisticated mechanical designs, and manufacturing with more precision using composite materials are all ways to achieve this goal.

## REFERENCES

---

- [1] W. Na, "A Case Analysis on Amazon Delivery Drones Taking over Traditional Delivery Method," *International Journal of Economic Behavior and Organization*, Jan. 2023, doi: 10.11648/j.ijebo.20231101.11.
- [2] "US20170240276A1 - Unmanned glider system for payload dispersion - Google Patents." Accessed: Dec. 11, 2024. [Online]. Available: <https://patents.google.com/patent/US20170240276A1/en>
- [3] C. Delarosa, L. Richards, T. Hilton, C. ; Richards, and H. Ty, "Multipurpose Glider-Quadcopter UAS Recommended Citation Multipurpose Glider-Quadcopter UAS Team Name: Down 2 Fly," 2018. [Online]. Available: [https://digitalcommons.kennesaw.edu/egr\\_srdsn/2](https://digitalcommons.kennesaw.edu/egr_srdsn/2)
- [4] Y. Wang, "The design, prototyping, modeling and flight tests of a vertical take-off and landing (VTOL) unmanned aerial vehicle (UAV)," 2017, doi: 10.14711/THESIS-991012535962203412.
- [5] R. Czyba and G. Szafranski, "Control structure impact on the flying performance of the multi-rotor VTOL platform - Design, analysis and experimental validation," *Int J Adv Robot Syst*, vol. 10, Jan. 2013, doi: 10.5772/53747.
- [6] G. J. J. Ducard and M. Allenspach, "Review of designs and flight control techniques of hybrid and convertible VTOL UAVs," Nov. 01, 2021, *Elsevier Masson s.r.l.* doi: 10.1016/j.ast.2021.107035.
- [7] S. Y. Choi and D. Cha, "Unmanned aerial vehicles using machine learning for autonomous flight; state-of-the-art," *Advanced Robotics*, vol. 33, no. 6, pp. 265–277, Mar. 2019, doi: 10.1080/01691864.2019.1586760.
- [8] J. Roghair, A. Niaraki, K. Ko, and A. Jannesari, "A Vision Based Deep Reinforcement Learning Algorithm for UAV Obstacle Avoidance," *Lecture Notes in Networks and Systems*, vol. 294, pp. 115–128, Mar. 2021, doi: 10.1007/978-3-030-82193-7\_8.
- [9] B. T. M. Leong, S. M. Low, and M. P. L. Ooi, "Low-Cost Microcontroller-based Hover Control Design of a Quadcopter," *Procedia Eng*, vol. 41, pp. 458–464, Jan. 2012, doi: 10.1016/J.PROENG.2012.07.198.
- [10] Z. Sun, L. Zhong, X. Cheng, and J. Guo, "Control Strategy Analysis of Brushless DC Motor," 2023 IEEE 3rd International Conference on Power, Electronics and Computer Applications, ICPECA 2023, pp. 386–389, 2023, doi: 10.1109/ICPECA56706.2023.10076158.
- [11] C. Millán-Arias, R. Contreras, F. Cruz, and B. Fernandes, "Reinforcement Learning for UAV control with Policy and Reward Shaping," *Proceedings - International Conference of the Chilean Computer Science Society, SCCC*, vol. 2022-November, Dec. 2022, doi: 10.1109/SCCC57464.2022.10000286.
- [12] H. K. Khalil, "Nonlinear Systems Third Edition."
- [13] M. Xie *et al.*, "An adaptive recursive sliding mode attitude control for tiltrotor UAV in flight mode transition based on super-twisting extended state observer," Nov. 2021, Accessed: Dec. 11, 2024. [Online]. Available: <https://arxiv.org/abs/2111.02046v1>
- [14] E. D'Amato, G. Di Francesco, I. Notaro, G. Tartaglione, and M. Mattei, "Nonlinear Dynamic Inversion and Neural Networks for a Tilt Tri-Rotor UAV," *IFAC-PapersOnLine*, vol. 48, no. 9, pp. 162–167, Jan. 2015, doi: 10.1016/J.IFACOL.2015.08.077.
- [15] H. Zhao, B. Wang, Y. Shen, Y. Zhang, N. Li, and Z. Gao, "Development of Multimode Flight Transition Strategy for Tilt-Rotor VTOL UAVs," *Drones 2023, Vol. 7, Page 580*, vol. 7, no. 9, p. 580, Sep. 2023, doi: 10.3390/DRONES7090580.
- [16] J. Betancourt, P. Castillo, and R. Lozano, "Stabilization and Tracking Control Algorithms for VTOL Aircraft: Theoretical and Practical Overview," *Journal of Intelligent and Robotic Systems: Theory and Applications*, vol. 100, no. 3–4, pp. 1249–1263, Dec. 2020, doi: 10.1007/S10846-020-01252-7/METRICS.
- [17] G. Nugroho, G. Zuliardiansyah, and A. A. Rasyiddin, "Performance Analysis of Empennage Configurations on a Surveillance and Monitoring Mission of a VTOL-Plane UAV Using a Computational

Fluid Dynamics Simulation," *Aerospace* 2022, Vol. 9, Page 208, vol. 9, no. 4, p. 208, Apr. 2022, doi: 10.3390/AEROSPACE9040208.

- [18] H. Wang, W. Sun, C. Zhao, S. Zhang, and J. Han, "Dynamic Modeling and Control for Tilt-Rotor UAV Based on 3D Flow Field Transient CFD," *Drones* 2022, Vol. 6, Page 338, vol. 6, no. 11, p. 338, Nov. 2022, doi: 10.3390/DRONES6110338.
- [19] G. Nugroho, Y. D. Hutagaol, and G. Zuliardiansyah, "Aerodynamic Performance Analysis of VTOL Arm Configurations of a VTOL Plane UAV Using a Computational Fluid Dynamics Simulation," *Drones* 2022, Vol. 6, Page 392, vol. 6, no. 12, p. 392, Dec. 2022, doi: 10.3390/DRONES6120392.
- [20] K. Min, F. Chia, and B. Kim, "DESIGN AND CFD ANALYSIS OF A LOW-ALTITUDE VTOL UAV," 2019. [Online]. Available: [www.tjprc.org](http://www.tjprc.org)
- [21] C. Bliamis, I. Zacharakis, P. Kaparos, and K. Yakinthos, "Aerodynamic and stability analysis of a VTOL flying wing UAV," *IOP Conf Ser Mater Sci Eng*, vol. 1024, no. 1, p. 012039, Jan. 2021, doi: 10.1088/1757-899X/1024/1/012039.
- [22] "NACA 4412 (naca4412-il)." Accessed: Dec. 19, 2024. [Online]. Available: <http://airfoiltools.com/airfoil/details?airfoil=naca4412-il>
- [23] "TD-8120MG Digital Servo."

## APPENDIX

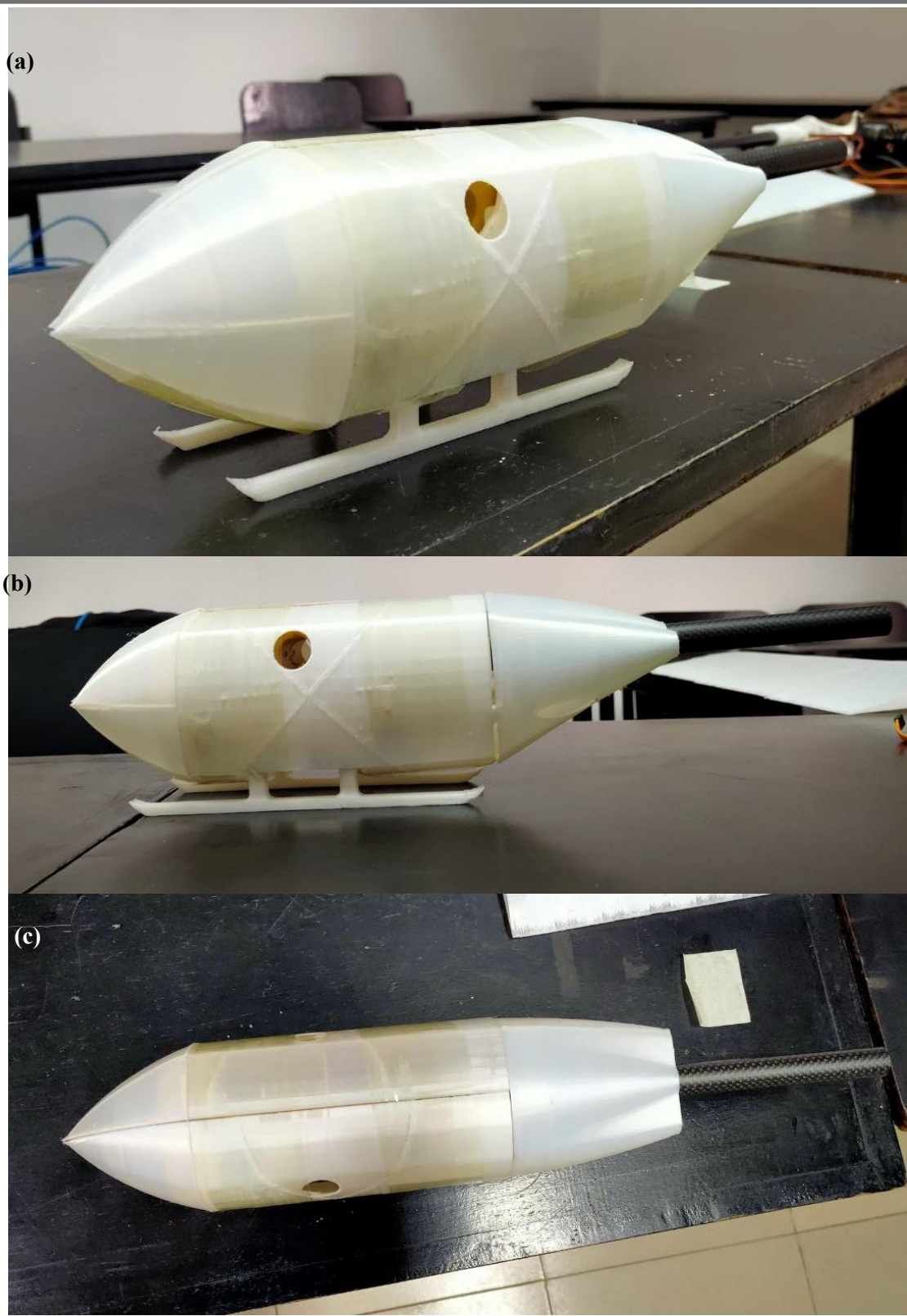


*Figure A1(a-c): Outer body.*

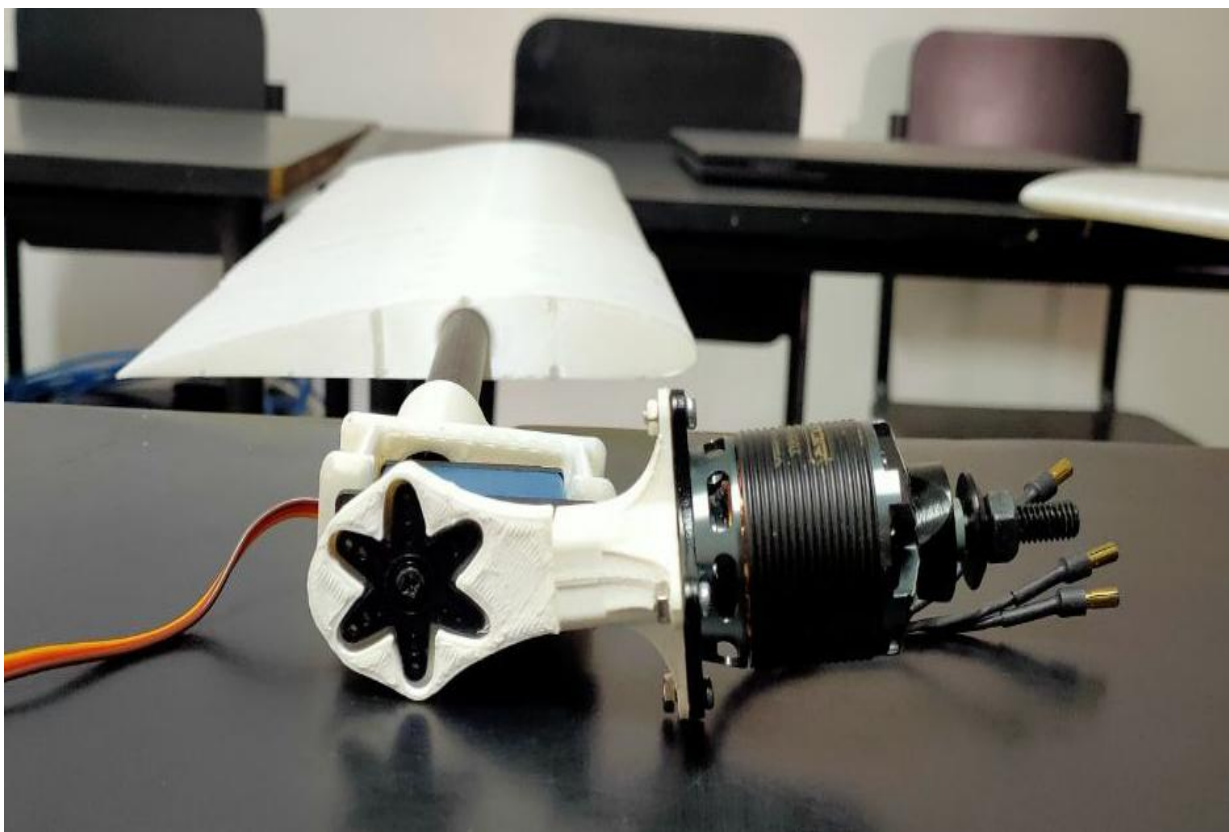


*Figure A2: Wing design with mechanism for forward flight.*

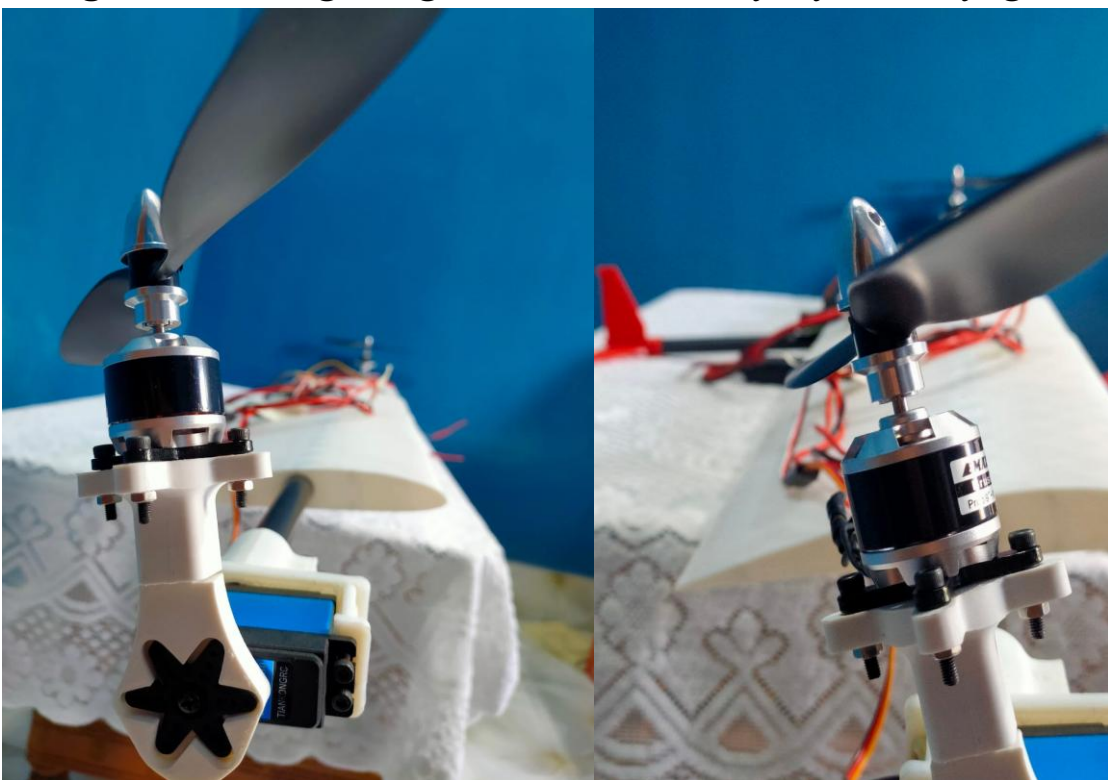


*Figure A3: Full assembled mechanism for hover flight.*

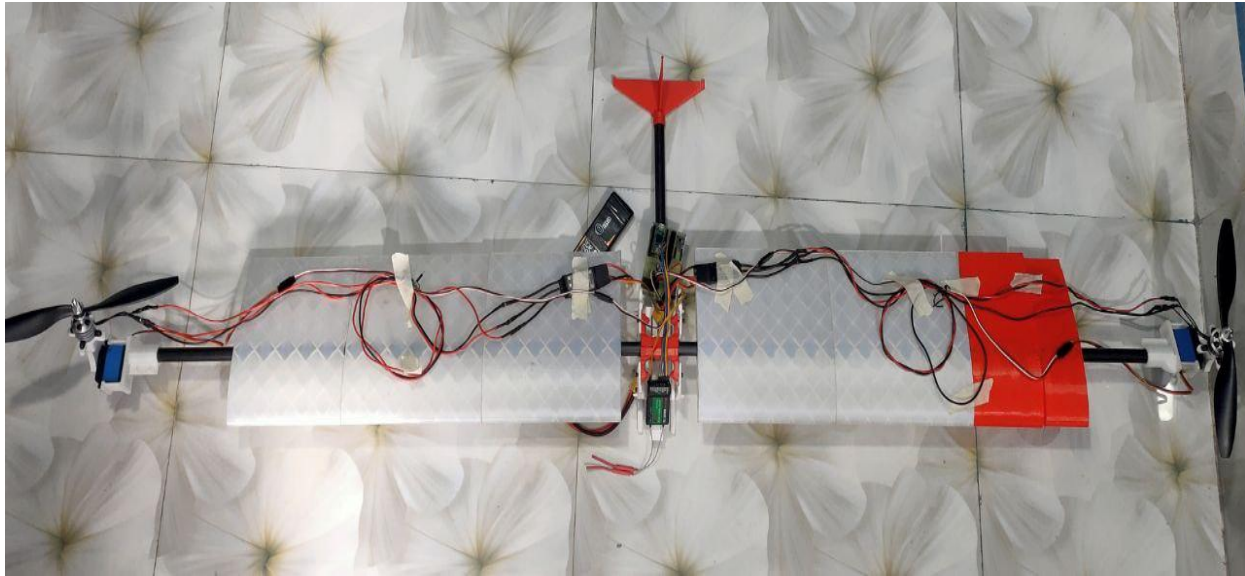


**Figure A4:** Fully assembled body with mechanism.

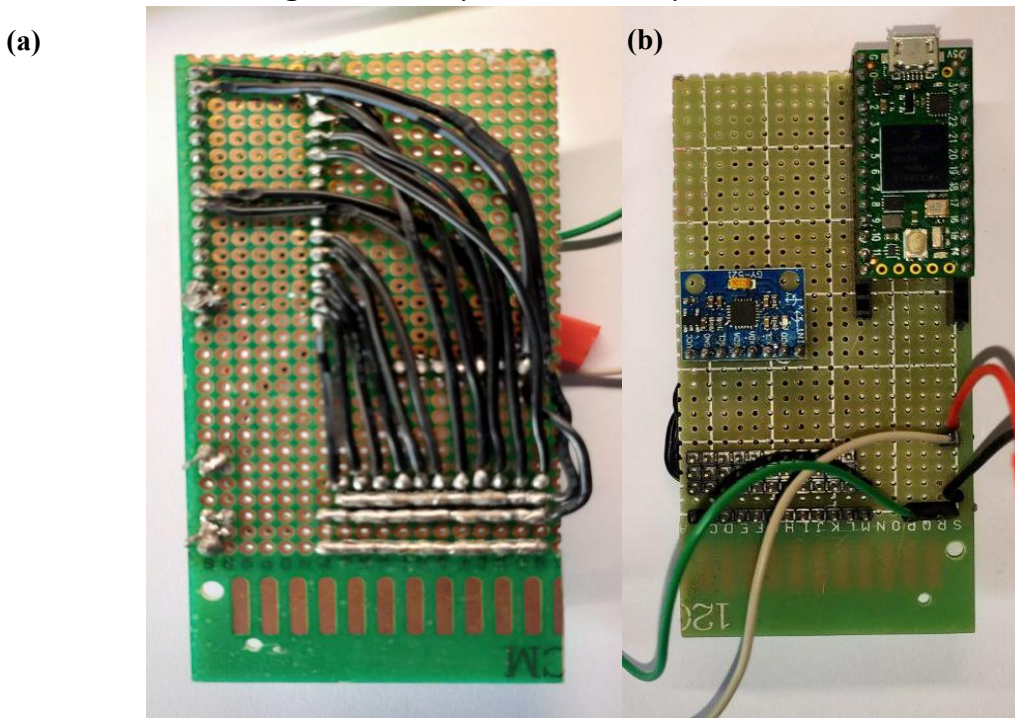


**Figure A5:** Flight controller v1 a) back, b) front.

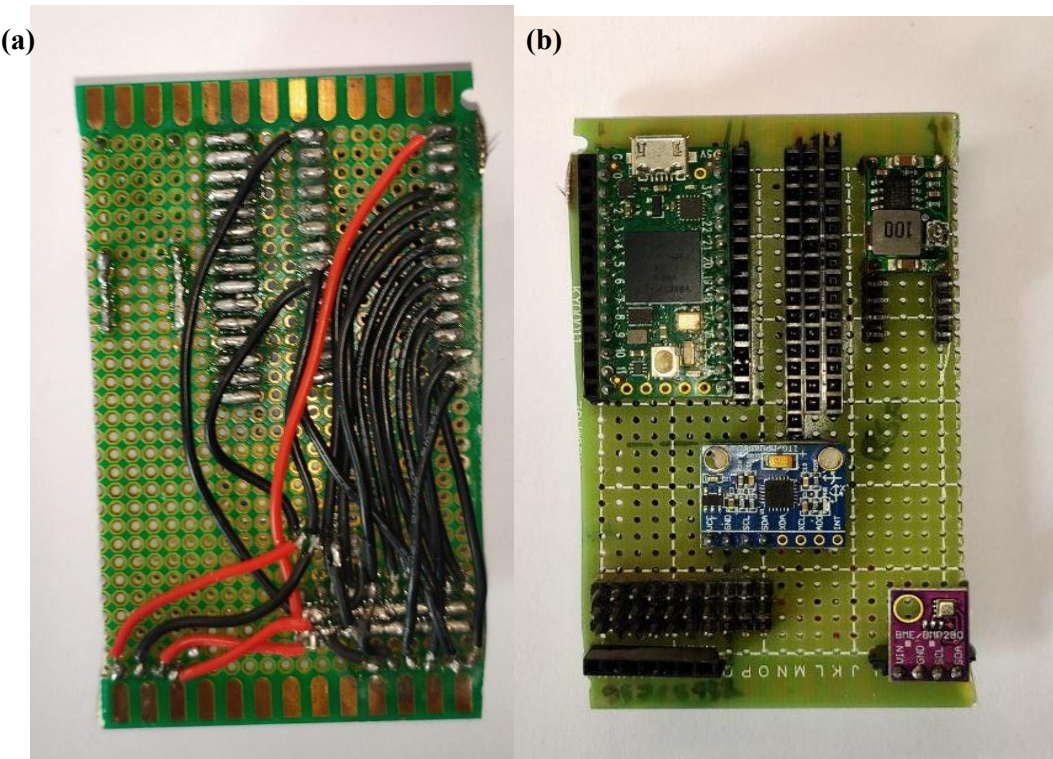


*Figure A6: Flight controller v2 a) back, b) front.*